Synthesis of N-doped broken hollow carbon spheres and inorganic-organic hybrid perovskite materials for application in photovoltaic devices

By

Hajeccarim Baloyi

Student Number: 1067074

A dissertation submitted to the Faculty of Science, University of the Witwatersrand, Johannesburg, in fulfilment of the requirements for degree of

Master of Science in Chemistry

Supervisor:

Professor Neil J. Coville

Co-Supervisors:

Associate Professor Daniel Wamwangi and Dr Manoko Maubane

Declaration

I declare that this thesis is my own, unaided work and it was done under the supervision of Professor N.J. Coville and co-supervised by Dr D. Wamwangi and Dr M. Maubane. It is being submitted for the degree of Masters in Chemistry at the University of the Witwatersrand, Johannesburg. The work has not been submitted before for any degree or examination in any other university.

_____

(*Signature*) Hajeccarim Baloyi

On this ..29.. day of….May…2018

Abstract

The mandate for renewable energy sources to replace the current reliance on fossil fuels as a primary energy source has recently attracted a lot of research interest. The research has also focussed on bringing the technologies that take into consideration the goal of reducing environmental pollution. Consequently, approaches using photovoltaic (PV) technologies have been a promising arena to tackle the problem facing energy sources. Recently, more focus has been placed on improving the power conversion efficiency (PCE) of PV devices, such as organic and/or organic-inorganic hybrid perovskite solar cells. Therefore, in this work two different materials were applied in two independent PV devices, namely organic and/or organic-inorganic hybrid perovskite solar cells.

One study employed nitrogen doped broken hollow carbon spheres (N-bHCSs), with an aim of enhancing the electronic properties of the P3HT:PCBM active layer of an organic photovoltaic (OPV) solar cell. N-bHCSs were successfully synthesized using a horizontal chemical vapour deposition method (H-CVD) employing a template-based method and the carbon was doped using *in-situ* and *ex-situ* doping techniques. Pyridine, acetonitrile and toluene were used as both carbon and nitrogen precursors. The dispersity of the SiO_2 spheres (i.e. templates) was found to play a role on the breakage of the N-bHCSs. Incorporation of the N-bHCSs into the P3HT:PCBM active layer was found to enhance the charge transfer and this led to less recombination of photogenerated charges in the interface between the donor and acceptor. The current-voltage (I-V) characteristics of the ITO/PEPOT:PSS/P3HT:PCBM:N-bHCSs/Al solar cell devices revealed an increased charge-transport distance due to increased electron density by n-type doping from the N-bHCSs.

The second study employed the organic-inorganic hybrid perovskite ($CH_3NH_3PbI_3$) material as a light harvesting layer in an ITO/PEDOT:PSS/$CH_3NH_3PbI_3$/PC_6BM/Al solar cell device. Initially, the device parameters were optimised to obtain the best performing device. These include parameters such as the degradation of the hybrid film as a function of time and air exposure. A rapid degradation was seen on the device after 24 h of air exposure which was accompanied by the decrease in the PV performance of the device. The degradation was visually seen by the formation of crystal grains (i.e. “islands”) on the perovskite film.

Dedication

I would like to dedicate this thesis to the following:

My family: Sylvia Baloyi, Morris Baloyi, Eugene Baloyi and Maisie Baloyi for their support, motivation and inspiration.

My late best friend: Rajesh Molose for his motivation, inspiration and encouragement. May his beautiful soul R.I.P!

My late girlfriend: Sanelisiwe Mbanga for her motivation and encouragement to move forward despite the obstacles and mostly for her love and caring. May her beautiful soul R.I.P!

Psalm 46:1-3

"God is our refuge and strength, an ever-present help in trouble.

Therefore, we will not fear, though the earth gives way and the mountains fall into the heart of the sea, though its waters roar and foam and the mountains quake with their surging".

Acknowledgements

First and foremost, I would like to thank my supervisor Professor Neil J. Coville for his outstanding support and guidance from the beginning to the end of this research.

I would also like to give a special gratitude to my co-supervisors, Associate Professor Daniel Wamwangi and Dr Manoko Maubane for their guidance, timeously feedback on the project and also for their mentorship throughout this research.

I would like to sincerely thank my mentors, Dr Bridget K. Mutuma, Dr Boitumelo Matsoso and Dr Kamalakannan Ranganathan for their great support in accomplishing this work.

Finally, I would like thank DST-NRF Centre of Excellence in Strong Materials; this research would not be possible without their financial assistance.

Publications and presentations

Publications related to this work

1. **Baloyi, H,** B. Matsoso, B. Mutuma, M. Maubane, D. Wamwangi, N. J. Coville. "Study of N-doped broken-shell carbon materials for their use in photovoltaic solar cell devices", *to be submitted.*

Publications from collaborations

1. Ncube, P., Bingwa, N., **Baloyi, H.** and Meijboom, R., "Catalytic activity of palladium and gold dendrimer-encapsulated nanoparticles for methylene blue reduction: A kinetic analysis", *Applied Catalysis A*, **2015,** *495*, 63-71.

Presentations

1. Study of N-doped broken-shell carbon materials for their use in photovoltaic solar cell devices; **Poster presentation**. Catalysis Society of South Africa (CATSA) Annual conference. Johannesburg, South Africa. November 2016.

2. Study of N-doped Broken Hollow Carbon Spheres, Inorganic-Organic Hybrid Perovskite Materials and their Application in Photovoltaic Devices; **Poster presentation and flash presentation**. Catalysis Society of South Africa (CATSA) Annual conference. Johannesburg, South Africa. November 2017.

List of figures

Chapter 2

Chapter 3

Chapter 4

List of tables

Chapter 3

Chapter 4

Abbreviations

AFM Atomic force microscopy

BET Brunner-Emmet-Teller

BHJ Bulk heterojunction

bHCSs broken Hollow Carbon Spheres

CNTs Carbon nanotubes

CVD Chemical vapor deposition

dH_2O Deionised water

DSSCs Dye-sensitized solar cells

EtOH Ethanol

Eq. Equation

Fig. Figure

FTIR Fourier Transform Infrared spectroscopy

HCSs Hollow carbon spheres

HF Hydroflouric acid

HOMO Highest occupied molecular orbital

LUMO Lowest unoccupied molecular orbital

ITO Indium tin oxide

J_{max} Current density at maximum power

J_{SC} Current density

LUMO Lowest unoccupied molecular orbital

N-bHCSs N-doped broken Hollow Carbon Spheres

OPV Organic photovoltaic device

PCE Power conversion efficiency

PCBM Phenyl-C61-butyric acid methyl ester

PEDOT:PSS Poly(3,4-ethylenedioxylenethiophene):poly(styrenesulfonic acid)

P3HT Poly(3-hexyl-thiophene-2,5-diyl)

PL Photoluminescence spectroscopy

P_{max} Maximum power

RH Relative humidity

R_s Series resistance

R_{sh} Shunt resistance

sccm Standard cubic centimetres per minute

SEM Scanning electron microscopy

TEM Transmission electron microscopy

TEOS Tetraethylorthosilicate

$\mathbf{V_{max}}$ Voltage at maximum power

$\mathbf{V_{oc}}$ Open circuit voltage

Table of contents

Chapter 1

Research questions and hypothesis

1.1 Motivation of the study

The perpetual increasing world energy demand for electricity and power consumption has recently led to the depletion of fossil fuels and their reserves. This had led to a high demand to find the substitute materials to compensate the energy consumption[1]. The discovery of shaped carbon nanomaterials (SCNMs) had led to an intensive research effort, exploring their properties and bringing forth their applications in various fields such as catalysis, materials sciences etc.[2-5]. This study was motivated by the recent discovery of broken hollow carbon spheres (bHCSs),[6] which raised thoughts around using these materials in the photovoltaic (PV) arena to explore their physicochemical, optical and PV properties in depth[7]. The study also explores the use of inorganic-organic hybrid perovskite materials in PV devices and monitors their decomposition behaviour as a function of time and moisture exposure.

This study on N-bHCSs has a foundation already laid by Bridget Mutuma and colleagues on their study done using similar bHCSs but without N-doping6. Herein, we extend their study, by employing both ex-situ and in-situ N-doping techniques in an attempt to enhance their electronic and photovoltaic properties. In the second part of the dissertation, a pristine inorganic-organic hybrid perovskite material (i.e. $CH_3NH_3PbI_3$) was employed as a light harvesting material and the effect of moisture on the overall morphology and performance of the $CH_3NH_3PbI_3$ crystals in a solar cell device was explored. The two parts of the project are connected in that the objective in making the N-bHCSs was to assist in providing a 'shell' structure for eliminating or reducing the moisture effects that plague the use of perovskite solar cell devices. The actual use of the shell structure was not achieved in this study but will be investigated in later studies by others to complete the study.

The main objective of the second part of study was then to monitor the degradation rate of the $CH_3NH_3PbI_3$ crystals in the PV device and explore their morphology and overall impact on the performance of the device. We have also taken into consideration of the fact that N-bHCSs does

not absorb light can be a challenge when applying the encapsulated perovskite materials in solar cell devices as light harvesting materials, but first step will be to achieve this encapsulation for long time storage of $CH_3NH_3PbI_3$ crystals.

The study holds a value in exploring alternative sources of electricity, which in this case it's photovoltaics, taking into account factors such as cost-effectiveness, environmental friendliness and also accessibility.

1.2 Questions to be addressed

1.2.1 Carbon nanomaterials

i. Does the doping technique (*in-situ* and *ex-situ*) have an effect on the overall morphology of the N-bHCSs?

ii. How does the dispersity of the SiO_2 spheres and horizontal chemical vapour deposition (H-CVD) control the morphology of the synthesized N-bHCSs?

iii. How do N-bHCSs influence the electronic, optical and photovoltaic properties of the P3HT: PCBM active layer?

1.2.2 Inorganic-organic perovskite photovoltaic devices

i. How does air exposure influence the morphology of the $CH_3NH_3PbI_3$ crystal?

ii. How does the change in $CH_3NH_3PbI_3$ morphology affect the photovoltaic device performance?

1.3 Aims and objective

1.3.1 Synthesis and characterization of pristine HCSs and N-bHCSs using H-CVD methods using both *in-situ* and *ex-situ* approaches and the investigation of the effects of the SiO_2 spheres dispersity and nitrogen doping and on the morphology of the N-bHCSs.

1.3.2 Investigation of the effect of doping of a P3HT: PCBM active layer with N-bHCSs on photovoltaic device performance.

1.4 Hypothesis

1.4.1 We hypothesized the doping P3HT:PCBM blends with N-bHCSs will enhance the electronic properties and photovoltaic properties of these materials.

1.4.2 We hypothesize that N-doping of bHCSs will increase the electronic and physical properties of these materials as compared to the pristine bHCSs reported in literature[6].

1.4.3 We hypothesis that the degradation of $CH_3NH_3PbI_3$ crystals will be a fast process and after completion of the decomposition process, the solar cell devices fabricated using these materials will drastically decrease.

1.4.4 We hypothesize that while the degradation of $CH_3NH_3PbI_3$ crystals will be a fast process and after completion of the decomposition process, the solar cell devices fabricated using these materials will drastically decrease, that encapsulation in bNHCSs will reduce this behaviour

1.5 References

2. Deng, Y., Xie, Y., Zou, K. & Ji, X. Review on recent advances in nitrogen-doped carbons: preparations and applications in supercapacitors. *J. Mater. Chem. A.* **4,** 1144–1173 (2015).
3. Masalov, V. M., Sukhinina, N. S., Kudrenko, E. A. & Emelchenko, G. A. Mechanism of formation and nanostructure of Stöber silica particles. *Nanotechnology*. **22,** 275718 (2011).
4. Servaites, J. D., Ratner, M. A. & Marks, T. J. Organic solar cells: A new look at traditional models. *Energy Environ. Sci.* **4,** 4410–4422 (2011).
5. Guldi, D. M., Rahman, G. M. A., Zerbetto, F. & Prato, M. Carbon Nanotubes in Electron Donor−Acceptor Nanocomposites. *Acc. Chem. Res.* **38,** 871–878 (2005).
6. Choy, D.M. Chemical vapour deposition of coatings. *Prog. Mater. Sci.* **48,** 57–170 (2003).
7. Mutuma, B. Generation of open ended , worm like and graphene like structures from layered spherical carbon materials. RSC Adv. **6**, 20399–20408 (2016).
8. Carlsson, J.-O. & Jansson, U. Progress in chemical vapor deposition. *Prog. Solid State Chem.* **22,** 237–292 (1993).

Chapter 2

Literature Review

2.1 Introduction

2.1.1 Carbon nanomaterials

The discovery of new polyhedral (mostly sp^2 bonded) carbon clusters with nanoscale dimensions such as fullerene in 1985, single walled nanotubes in 1991 and graphene in 2004 drove an increased interest in the structures of shaped carbon nanomaterials (SCNMs) especially the carbon nanomaterials (CNMs) constrained at the nanoscale[1–3]. The advantages of CNMs on the mentioned applications, is mainly their controllable sizes, environmental friendliness and they are seen as cost-effective as compared to other known technologies[2]. All these materials exhibit physicochemical properties, which gives them advantages[3]. CNMs can take a spherical shape which has been exploited recently for many uses including their application in lithium ion batteries, energy storage, paintings, drug delivery systems, catalyst supports, tyres, high strength composites, lubricants, for the dispersion of silver nanoparticles and so forth[4–6]. Some other shapes adopted by carbon include onions and these materials differ in terms of the number of carbon layers and their size ($d_{spheres} > d_{onions}$). All these carbon shapes adopt basic low dimensional forms and combining them into more complex 3D architectures is still a challenge[7]. A most imperative feature adopted by many SCNMs is that they contain a hollow centre surrounded by carbon layers which determine their shell thickness[8]. These materials are called hollow carbon spheres (HCSs). Alternatively, the hollow could be partially filled with a small particle (or particles) to give a rattle type structure. Carbon spheres (CSs) also possess electron accepting properties and hence they have been used recently in organic solar cells as electron accepting materials[9]. CSs can be synthesized by methods such as pyrolysis, chemical vapour deposition (CVD) and so forth and depending on the type of method employed, different micro-structures can be obtained and the type of the microstructure obtained can vary with other types in terms on their electrochemical properties[6,10,11].

2.1.2 Photovoltaics

Due to increasing demand for alternative energy sources, that are renewable in order to replace the current energy sources such as fossil fuels, a lot of research been initiated to address this issue[4,12]. One of the important technologies is photovoltaic (PV) devices. Various materials have been employed recently to improve the conversion factor of solar energy into electrical energy, also known as the power conversion efficiency (PCE) in PV arena. Attempts has been done recently to improve the PCE and these include the use of an extremely thin absorber (ETA) cell which is based on Sb_2S^3 sensitized mesoscopic TiO_2 films which gave a PCE of 6.3%[13, 18]. A coupling between the N719 dye with a p-type semiconductor ($CsSnI_3$) with a PCE to 8.5%[3] and a submicron thick film of mesoporous anatase enhanced the PCE to 9.7%[15]. The increase in PCE over the years is shown in Fig. 2.1[8].

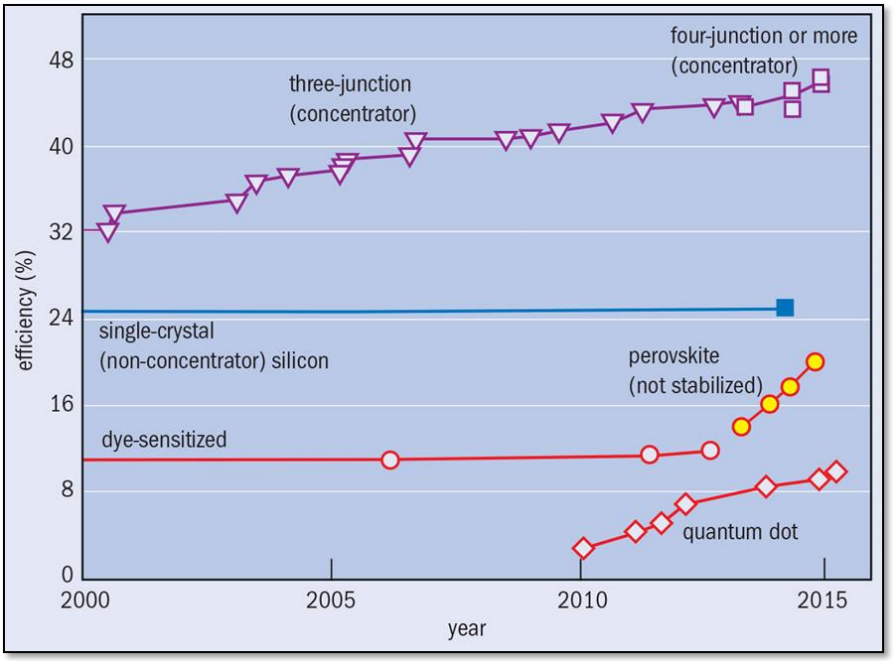

Fig. 2.1: Best reported PCEs reported from 2000 to 2015[18].

Recently, intrinsically core-shell plasmonic dielectric nanostructures have also shown unique optical properties (i.e. a high refractive index extending up to 5.5 in the near-infrared frequency range) that flags an innovative way for designing low-loss and high-performance visible to infrared optical devices[14]. Si-based solar cells of numerous generations such as the single-crystalline, multi-crystalline, microcrystalline and amorphous-Si[8] have been also been studied to enhance their PCE without a cost trade-offs. Silicon based solar cells continue to dominate the PV technology, however their degradation under IR illumination (hot spots) have motivated the search for high

efficient and low cost PV alternatives[15]. The drive for new materials to substitute silicon has led to intensive research on carbon as a highly attractive substitute for Si due to its iso-valency with Si[16]. Graphene has been recently explored in many research field it lacks a bandgap due to the delocalization of the pi electrons in carbon atoms, a half-filled band with a linear dispersion that lies near the Brillouin zone corners, the so-called Dirac cone is formed. This makes graphene in its pristine form unsuitable as an active layer for PV applications[17], However its excellent electrical and optical properties could see it function as a transparent electrode. Several strategies have been explored for converting graphene from its pristine form to a more active form. The incorporation of heteroatoms such as nitrogen into a graphene matrix has recently provided a breakthrough into opening a bandgap in graphene. The role of incorporating heteroatoms in graphitic carbon nanomaterials is to either increase the electrons or holes in the carbon material, which is why the choice can be made on whether the doping should be p-type for holes or n-type for electrons[13].

2.2 Different carbon polymorphs

2.2.1 Graphene

Graphene is a flat single-layered structure made of hexagons with carbon atoms packed into a two-dimensional (2D) honeycomb framework, (Fig. 2.2). All graphitic materials of various dimensions can be derived from manipulating graphene sheets the so called "mother of all graphitic forms"[19]. For example, 3D graphite can be formed by stacking multiple graphene sheets. Rolling up the graphene sheet yields 1D nanotubes and wrapping up a graphene sheet yields 0D fullerenes[20].A distinguishing characteristic of graphene is its uncommon conical band structure that leads to a zero-energy band gap[21].

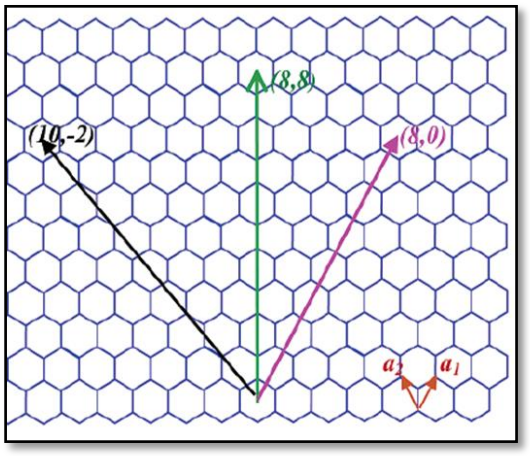

Fig. 2.2: Representative honeycomb structure of graphene sheet with the lattice vectors of folding[22] and a SEM image of graphene matrix[23].

The choice of production method is very important because various methods determine the quality, type of defects and substrate used for graphene[24]. Some of the methods, with their production quality and price are indicated in Fig. 2.3. From this figure we can notice variation methods such as CVD, mechanical exfoliation etc. lead to changes in quality of resulting materials and also the cost for mass production. Many studies, including our study, prefers the use of CVD to make carbonaceous materials because the method provides good yields of high quality materials cheaply[24-25].

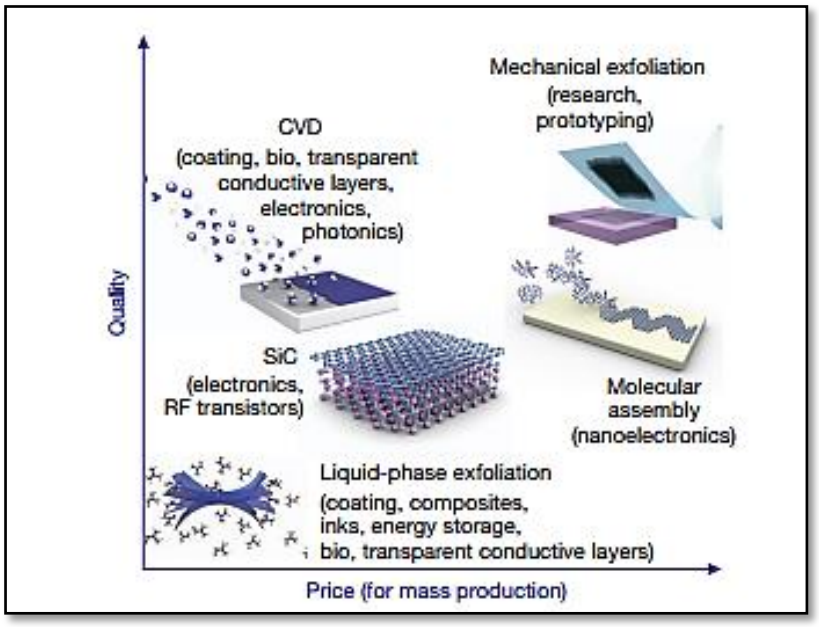

Fig. 2.3: Production methods of graphene in terms of quality and price[25].

Graphene has been applied in many fields such as in catalysis as a catalyst support materials because of extremely high surface area and adsorption capacity[26], and in photovoltaic devices to replace silicon-based electronic devices[27,28] etc. Graphene possesses some important features such as high carrier mobility[29], 2.3% constant absorption of visible light[30] and high mechanical strength[16] which makes it a good candidate for electronic applications. In the case of solar cell devices, a power conversion efficiency (PCE) of 10.4% and 15.5% for a graphene/GaAs-based solar cell device with and without an anti-reflective layer respectively has been reported, (Fig. 2.4)[31]. Fig. 2.4 presents a graphene-based device that uses Au and Ag as contact layers and also SiN_x as the dielectric insulating layer[31].

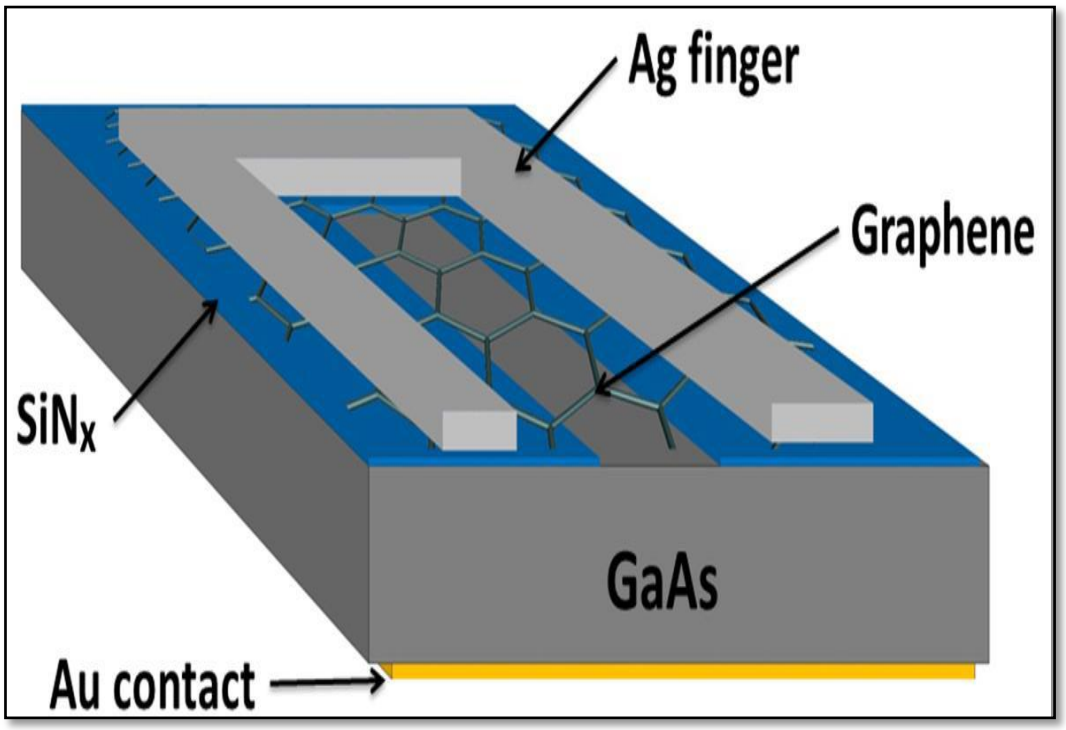

Fig. 2.4: Basic graphene/GaAs solar device with SiN_x as the dielectric insulating layer[31].

2.2.2 Carbon nanotubes

Carbon nanotubes (CNTs) are one of the carbon polymorphs that have recently attracted a lot of interest in the research field. They are made by various synthetic methods. They are "formally" made by wrapping graphene sheets into a tube. Depending on the manner in which the edges are oriented together lead to different types of CNTs. Synthetic methods can give single-walled nanotubes (SWCNTs) as shown in Fig. 2.5 (a) or multi-walled carbon nanotubes

(MWCNTs) as shown in Fig. 2.5 (b-d) which are made from several graphene sheets that are stacked together[19,22]. They are one-dimensional (1D) structures[32]. SWCNTs can either exhibit metallic or semiconducting properties whereas MWCNTs usually display metallic properties[19]. CNTs have been applied in many fields including the photovoltaic arena as a hole extraction layer due to their high work function[33].

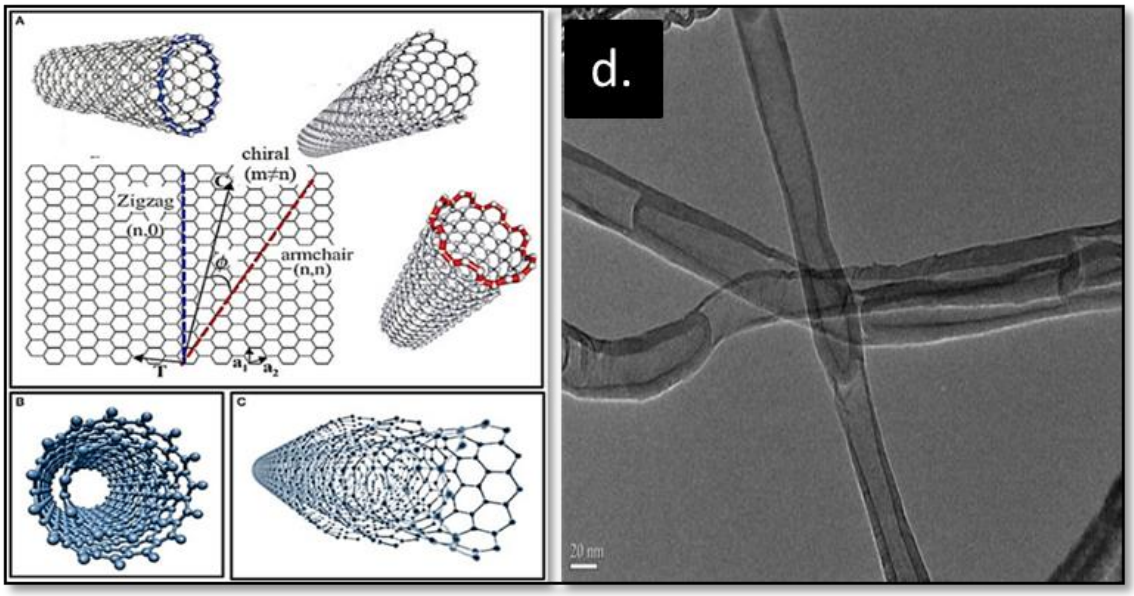

Fig. 2.5: Structural representation of carbon nanotubes with different sizes (a) SWCNTs and graphene lattice vectors of folding (b) Double-walled carbon nanotubes (DWCNTs) (c) MWCNTs and (d) TEM image of DWCNTs[34].

2.2.3 Carbon spheres

Carbon spheres (CSs) are spherically shaped carbon nanomaterials (SSCNs) which have recently received a great deal of attention because of their unique physical and chemical properties such as controllable sizes, morphology, good adsorption performance and minimal surface energies[35]. CSs have been employed in many applications, including catalyst support, in drug delivery, potential supercapacitor applications, and also in their use as lithium batteries[35–37]. CSs can either be semi-crystalline or crystalline and can have solid, core or hollow shell morphology, (Fig. 2.6). SSCNs encompass carbon microbeads, carbon onions, carbon black etc. CSs can be synthesized by various methods including laser ablation, chemical vapor deposition, autoclave processes and shock compression techniques amongst other methods[38]. These methods can either give a low yield of CSs or involve toxic complicated processes and attributes serve as the metrics for selecting the optimal method for a desired study. Ensuring the monodispersed CSs sizes is a key issue in their synthesis[38].

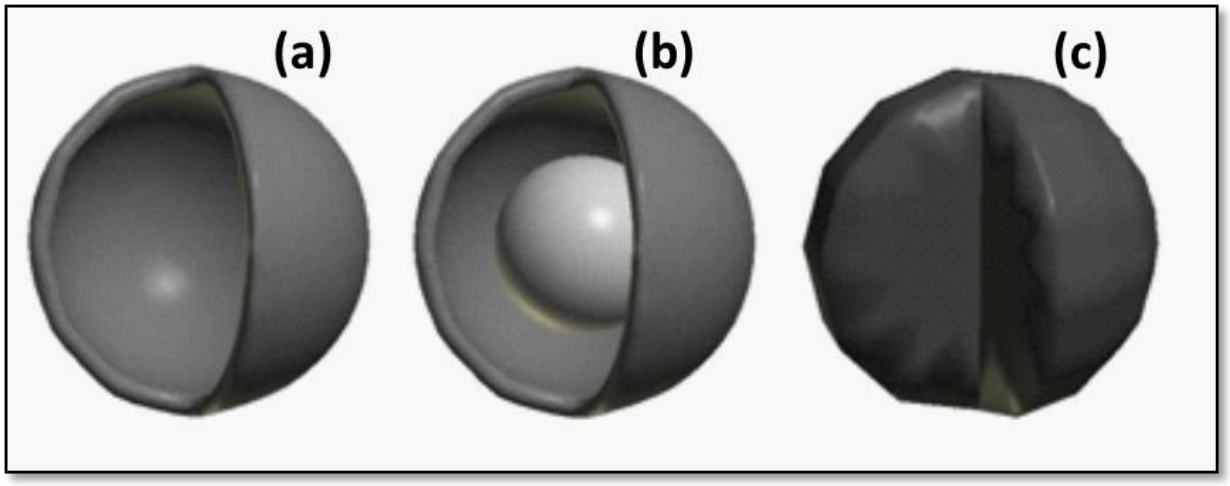

Fig. 2.6: (a) Hollow carbon sphere (b) Core shell carbon sphere and (c) Solid carbon sphere[1].

The growth mechanisms of CSs are influenced by the synthesis method used to make them, which can either involve a non-template or a template approach. Various parameters such as the carbon source, template, temperature etc. also play a role in the growth mechanism of CSs. Various studies have attempted the use of CSs in solar cell devices as electron transport layer, but the materials still suffer the problem concerning shorting and high recombination rates[32-33]. Some studies managed to resolve these issues to some extent by reducing the sizes of the CSs[36].

2.2.4 Hollow carbon spheres

Hollow carbon spheres (HCSs) are amongst the carbon shaped materials that are widely studied for their fascinating properties such as their special shape, low density, "tuneable" void volume, excellent flow performance, and large surface area[39]. HCSs can be synthesized by two main approaches: a template based and template free method. The internal volume of HCSs provides a space for storage or can be used as an artificial reaction "pot" in which to 'make' molecules, as was demonstrated from studies using mesoporous nanostructures[39].

i. Template based strategy

In the template-based approach, a rigid particle is prepared and employed as a "hard" core template, followed by coating the core template by a carbon-containing precursor with self-assembly on the template. Removal of the template after the formation of a carbon shell creates a hollow structure, (Fig. 2.7)[40]. The self-assembly process is facilitated by the formation of C-C bonds on the surface of the template which yields the core-shell structure[1,38,41]. The techniques that are often employed in a template-based approach include; CVD, hydrothermal carbonisation (HTC) and pyrolysis.

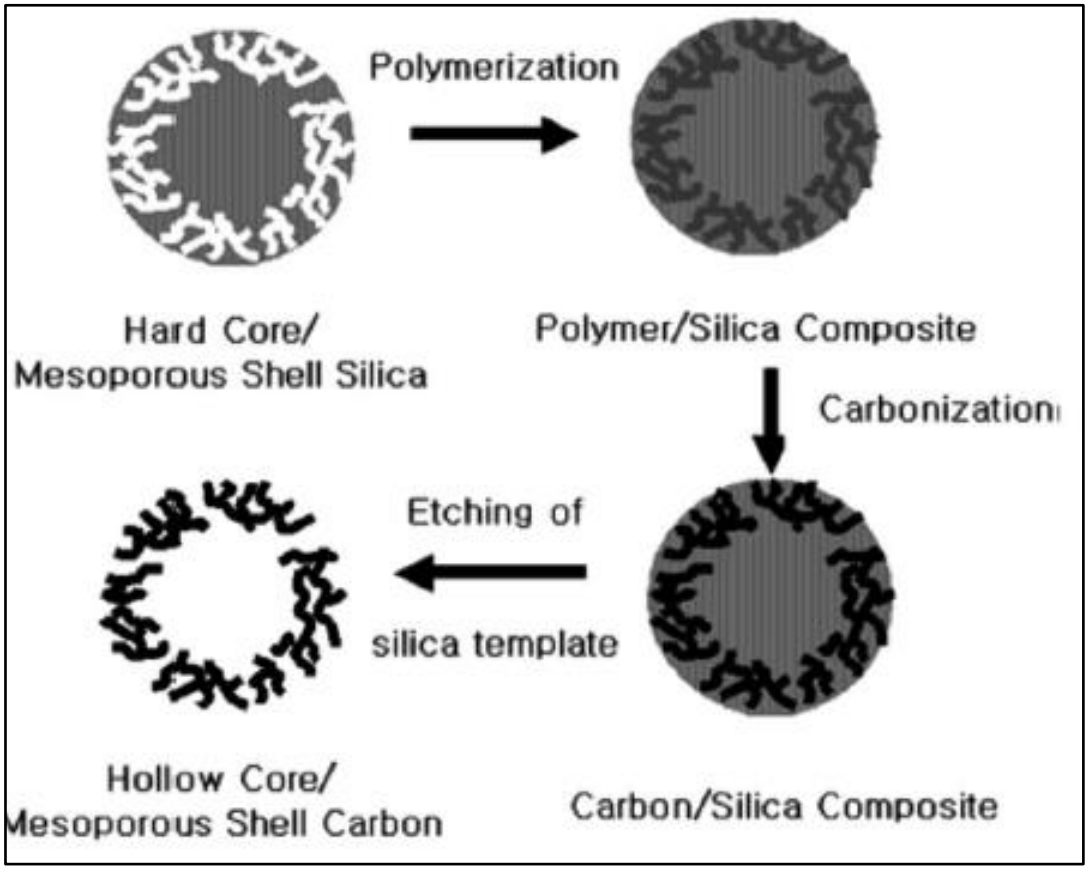

Fig. 2.7: Synthesis of mesoporous hollow carbon spheres by template based method of solid core/ mesoporous shell silica templates[40].

ii. Template free strategy

A template free method involves making the carbon nanostructures without introducing the template in the system. Li and co-workers[42] reported a hydrothermal processing approach as an example of a template free model of achieving carbon hollow spheres, (Fig. 2.8).

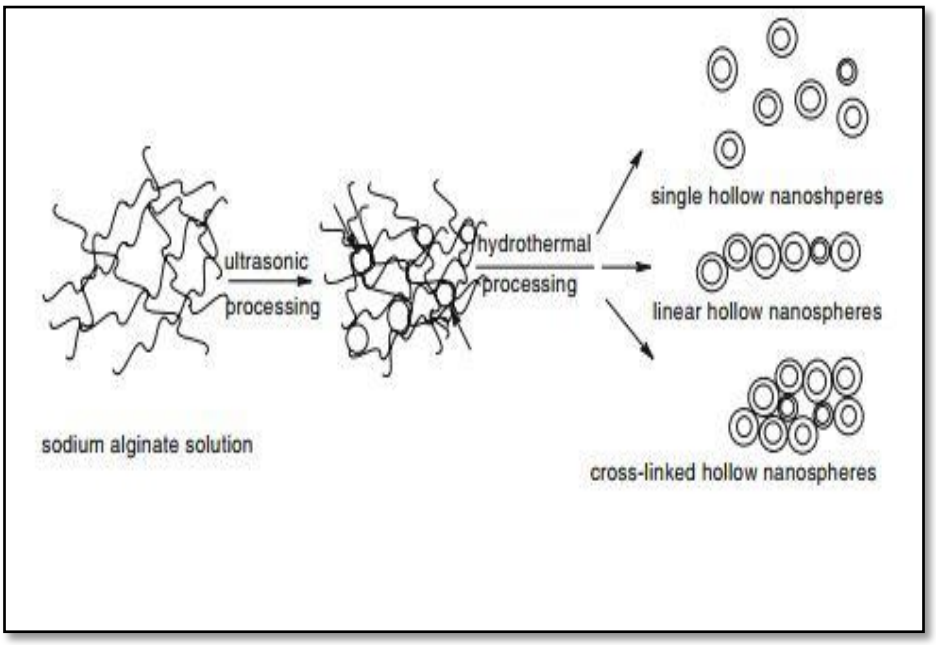

Fig. 2.8: Formation mechanism of hollow carbon nano spheres using a template free hydrothermal model[42].

2.3 Nitrogen doped carbon nanostructures

Modification of the (hydrophobic) pore structure of the carbon sphere can be done by using heteroatoms (doping with boron, nitrogen and so forth) into the CNMs to give nitrogen doped carbon nanomaterials, N-CNMs[43,44]. The practice of doping CNMs with surface heteroatoms could cause electron modulation to provide appropriate electronic structures for many applications[45]. N-CNMs have been employed in many applications, including the enhancement of capacitance[43], for use in making anode materials in Li-ion batteries by improving the electrochemical performance of carbon materials (e.g. by nitrogen doping)[6], as a support for platinum-based electro-catalysts[46] and in many other applications, N-CNMs can improve conductivity, enhance the interface with molecules, and modify the oxidation stability and activity of materials supported on carbon[47–50]. N-doping also results in redistribution of the spin and charge density states in CNMs[51–56]. However N-doping also introduces defects in the carbon framework and these defects constitute scattering centres that can consequently affect electron/hole mobility of graphene[57]. Many studies have employed two approaches to dope CNMs, *in-situ* and *ex-situ* doping approaches. The *in-situ* doping approach involves the incorporation of nitrogen atoms during the CNMs growth while the *ex-situ* techniques involves post-treatment of pre-prepared CNMs with a nitrogen-containing precursor such as NH_3. Both doping approaches have their own advantages; *in-situ* doping incorporates

nitrogen atoms into the entire carbon nanomaterials homogeneously whereas *ex-situ* doping leads to only surface functionalization of CNMs without modifying their bulk properties[45]. The study done by Bridget Mutuma and colleagues, had employed pristine bHCSs as doping agents for P3HT:PCBM based solar cells to enhance the opto-electronic properties of the these hybrid materials, however very low PCEs were obtained[33-36].

2.3.1 Effects of N-doping on the physicochemical properties of carbon materials

The properties of various carbon materials depend not only on the carbon porosity but also on the presence of heteroatoms (such as nitrogen, boron and oxygen) decoration their surface to extend their application realms[58]. The introduction of nitrogen into a CNM framework affects the bulk properties of the material, with effects contingent on the amount of nitrogen and the type of bonding configuration of the N[59]. Oxygen doping often contributes carbon surface acidic character, whereas nitrogen doping is often used to promote basic properties in order to enhance carbon interaction with acid molecules[60,61]. Many studies has recently put focus on N-doped carbon materials because of their outstanding electro-catalytic performance, low cost, good stability, high conductivity and environmental friendliness[62]. The presence of nitrogen in the graphitic plane of carbon increases the number of π-electrons and the difference in electronegativity of N and C leads to the changes in the carbon materials properties. Some properties enhanced by increased electron density include reduction of work-function, enhancement of field emission characteristics, increased n-type carrier concentration and high surface energy[19,21,30,63–65]. It has been observed in many studies that N-doping of various graphitic carbon materials also enhances the structural transformation of carbon[63]. Some studies also show that an increased nitrogen content, increases the basicity and the catalytic activity of carbon materials[66]. Studies done by Zhang and colleagues also showed that a nitrogen content on carbon materials can be varied by use of different temperature e.g. 21.66 % at 900°C[59] and 14.32 % at 1000°C[48].

2.3.2 Stability of N-doped carbon nanostructures

Studies on carbon nanotubes (CNTs), for example, has shown that N-doping increases the diameter, generates defects and decreases the crystallinity of CNTs[63]. It has also been found that nitrogen doping could inhibit the formation of micro-pores in mesoporous carbon materials[58]. It has been shown that the atomic quantity of nitrogen on CNMs can be controlled by varying the growth temperature of the CVD reaction[45]. Studies carried out by Tao and co-workers has demonstrated

that the oxidation temperature of pristine or non-doped carbon occurs at between 600-700℃ as compared to the alternate study where the N-CNMs had oxidative temperature around 550-680℃ revealing a reduced stability due to the disorder induced by incorporation nitrogen into the carbon framework[67].

2.3.3 Microstructure or electronic structure and elemental composition of N-doped carbon

X-ray photoelectron spectroscopy (XPS) is a tool that is often employed to describe the electronic state of N-doped CNMs. The microstructure of N-doped graphitic carbon materials possesses three common bonding configurations of N atoms; pyridinic, pyrrolic and graphitic/quaternary N, (Fig. 2.9)[41,68]. Bonding configurations affect the physical and chemical properties of N-CNMs, such as electron and hole transport performances[69]. These bonding configurations are also chemically active and improve the surface reactivity of carbon materials because of the existence of electron donors[70]. Pyridinic N is bonded with two C atoms at defect sites or edges of graphene sheets, contributing one p electron to the π electron system. Pyrrolic N contributes two p-electrons to the π system and graphitic N substitutes one C atom and bonds to three other adjacent C atoms in an hexagonal ring system of graphene[71,72]. Graphitic N shows an n-type doping effect, whereas pyridinic or pyrrolic N atoms show a p-type doping effect [25,73,74]. The atomic content of nitrogen on CNMs has also shown an important effect in terms of controlling n-type or p-type environment of graphene sheets, which is a very important property to be considered when deciding which semiconductor is to be incorporated in a PV device[45].

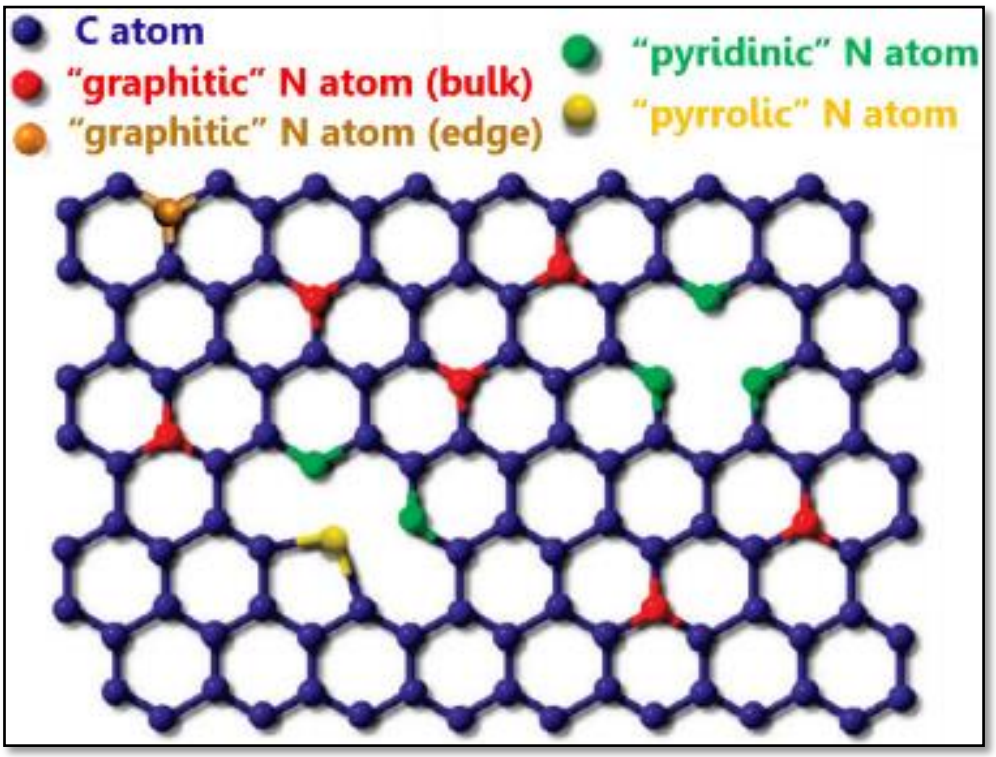

Fig. 2.9: Structural representation of nitrogen bonding configurations incorporated into graphitic carbon and their respective XPS binding energies[68].

XPS binding energies of these nitrogen configurations are estimated to be: pyridinic N 1*s* at 397.6 eV, pyrrolic N 1*s* at 399.6 eV and substitutional N 1*s* at 401.2 eV[75]. It is also worth noting that a choice of doping approach (i.e. *in-situ* and *ex-situ* doping) is also critical in yielding specific bonding configurations, It has been demonstrated that *in-situ* doping often yields pyrrolic and/or pyridinic-N whereas post-doping often yield graphitic/quartenary-N[62].

2.4 Photovoltaic devices

2.4.1 Semiconductors

Semiconductors are single elements of a compound class of materials with conductivity between that of an insulator and most metals[4]. Their electronic properties are temperature dependent due to the thermal excitation of the charge carriers, thus the conductivity of these materials increase with increasing temperature. Semiconductors can be classified as either n-type of p-type depending on the majority carriers (majority carriers for n-type are electrons and for p-type are holes).

2.4.2 General working principles of photovoltaic devices and overall architectural design

There are four essential steps involved in a typical operating PV device, (Fig. 2.10)[12], namely:

i. Absorption of light by the active layer to create free charge carriers or bound excitons. Generally, the excellent candidates for PV applications should have a high absorption coefficient which matches the solar emission spectrum.

ii. Generation of electron (e^-)/ hole (h^+) (photo-generated charges). These charge pairs can be bound to form a quasi-particle (exciton) which requires energy or an electric field to separate them.

iii. Separation of photo-generated charges (e^- goes to the negative terminal and h^+ goes to the positive terminal). The separation of charge carriers in inorganic solar cells is driven by the differences in the chemical potential of the n and p type semiconductors. However, for organic semiconductors, the closeness of electron donor and acceptor interfaces is essential for charge separation after diffusion of the exciton to the interface. The diffusion of the exciton is limited; thus, a short exciton diffusion length is essential for the efficient performance of an organic photovoltaic (OPV) device. This is the basis of the bulk heterojunction concept.

iv. Charge collection into the electrodes (e^- into the cathode and h^+ into the anode) to generate electrical power.

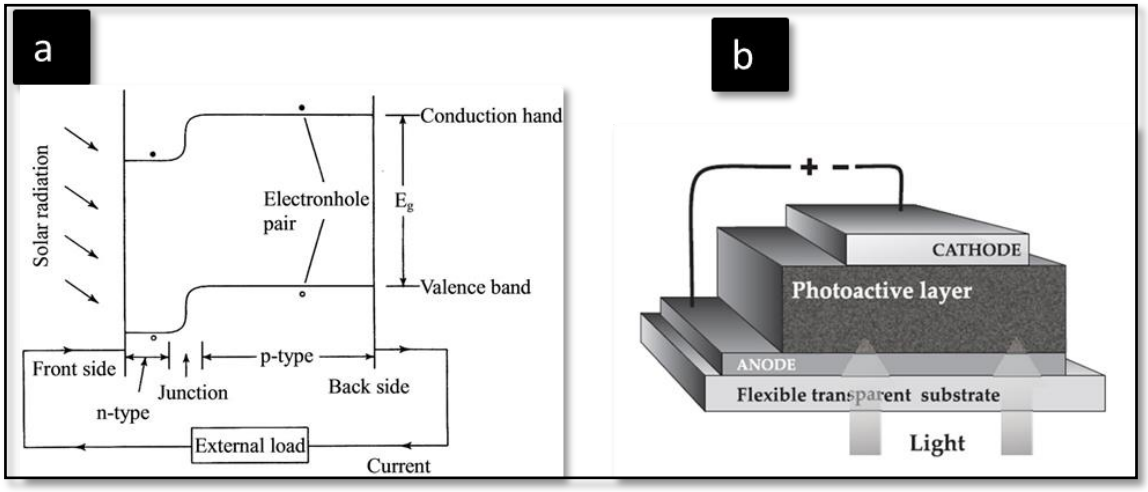

Fig. 2.10: (a) Working principle of a PV device[76], (b) Basic architectural design of PV device[77].

2.4.3 Typical PV device structure

2.4.3.1 p-n Junction of PV device

The p-n junction has been referred to as a "fundamental building block of the electronic age" due to its frequent advent in most of PV devices formed when an n-type and p-type semiconductor materials are fused together at the junction or when a semiconductor is doped by either an n-dopant (e.g. phosphorus) or p-dopant (e.g. boron)[78]. When semiconductors are fused together the e^- jumps from an n-type to p-type semiconductor and h^+ diffuse from a p-type to n-type semiconductor and eventually creates a space charge region (SCR) or a depletion layer, (Fig. 2.11 (a))[79]. The p-n junction will then induce a strong electric field pointing from the positively charged ions to the negatively charged ions creating a fixed space charge that enhance the separation of minority carriers[80].

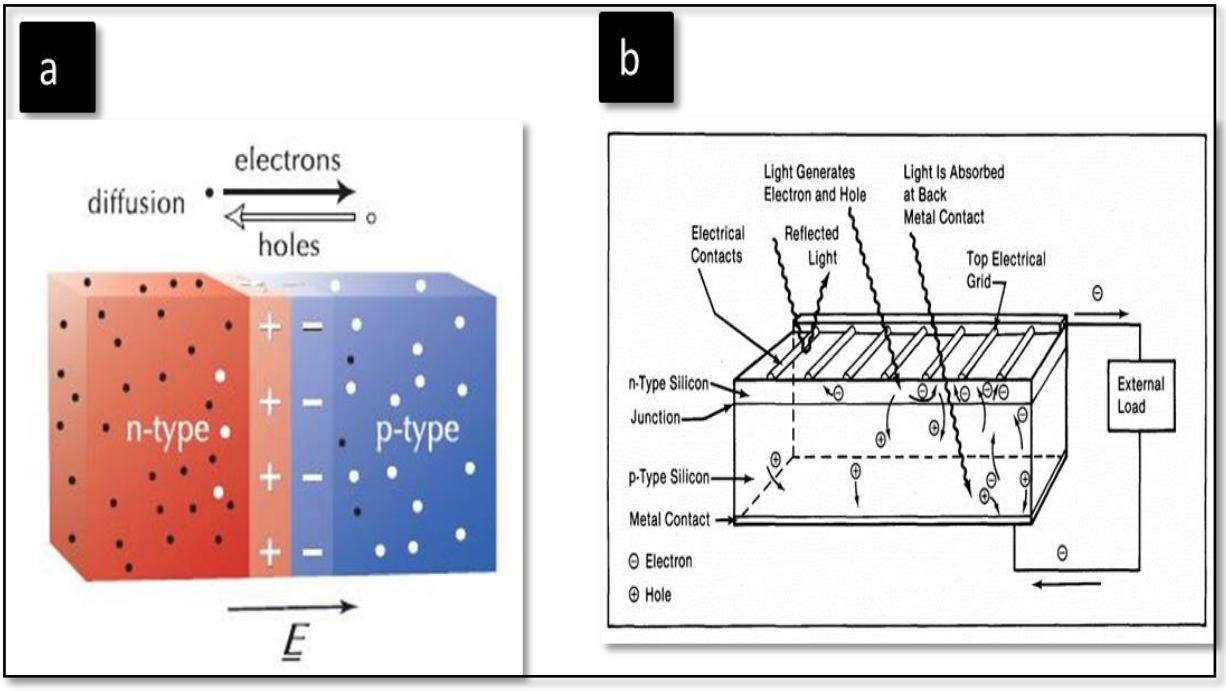

Fig. 2.11: (a) Basic p-n Junction showing e- moving from n-type to p-type and h^+ from p-type to n-type and (b) Comprehensive process of e^-/ h^+ pair generation after light absorption by the PV device[79].

The electric field created eventually generates an opposing force that moves some of the e^- and h^+ in the opposite direction to the flow caused by diffusion until an equilibrium state is reached. At equilibrium the number of e^- and h^+ due to diffusion balances those due to the electric field, and hence the net flow of both species becomes zero[81,82].

Although there is no longer a net current flow across the junction, an electric field is created at the junction, and the depletion region becomes very resistive and this forms the basis of the operation of diodes, transistors and solar cells[78]. When an external electric field (E_{ex}) is applied to the internal electric field (E_{in}), the resistivity is modified. The two electric fields can either be in the same direction or oppose each other and that determines whether the resistance will increase or decrease and this is hence called voltage-controlled resistor[30,83,84].

2.4.3.2 Forward and reverse bias

This is a configuration induced when a positive voltage is applied to the p-type side and the negative voltage is applied to the n-type side and this results in a low resistance and hence current flow (i.e. E_{ex} and E_{in} are in opposite directions). Reverse bias occurs when negative voltage is applied to the p-type side and the positive voltage is applied to the n-type side to give a very high resistance and hence no current flow (i.e. E_{ex} and E_{in} are on the same directions). Forward and reverse bias can be presented in an I-V curve, (Fig. 2.12)[78].

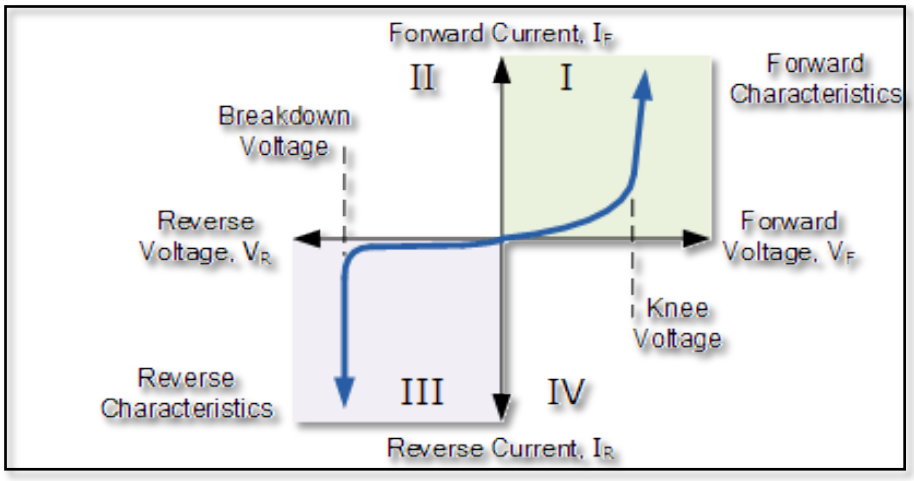

Fig. 2.12: I-V curve of the silicon p-n junction diode under forward and reverse bias conditions[78].

The effect of bias voltage can also be illustrated by energy band diagrams, (Fig. 2.13). When a negative voltage is applied, the potential across the semiconductor and the depletion layer width increases. When a positive voltage is applied, the potential across the semiconductor and the depletion layer width decreases[85]. The total potential across (ϕ) the semiconductor equals the built-in potential (ϕ_i) minus the applied voltage (V_a), (Fig. 2.13)[78].

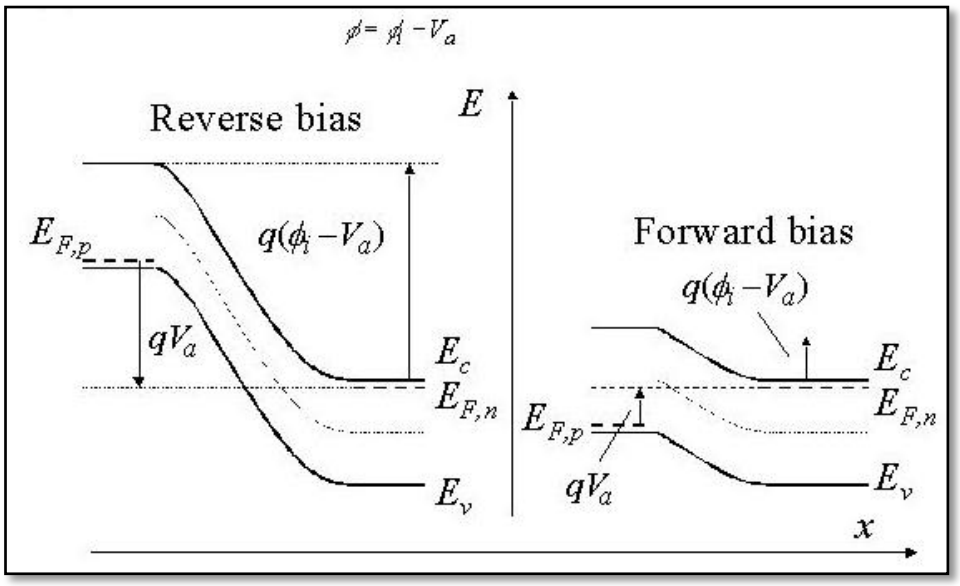

Fig. 2.13: Energy band diagram of a p-n junction under reverse and forward bias; V_a: applied bias voltage, ϕ_i: built in potential/ E_{in}, $E_{f,p}$ and $E_{f,n}$: fermi energies, E_c: conduction band energy and E_v: valence band energy[86].

2.4.4 Photovoltaic characterization

The photovoltaic properties of a solar cell are described with four major parameters from dark and illuminated current-voltage curves, (Fig. 2.14). The parameters include open circuit voltage (V_{oc}), short circuit current density (J_{sc}), fill factor (*FF*) and power conversion efficiency (PCE).

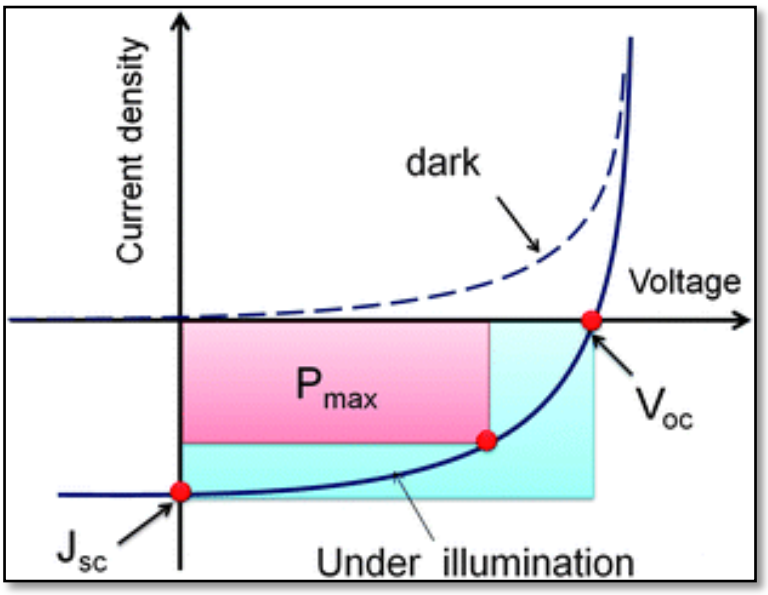

Fig. 2.14: Dark and illuminated current-voltage curve[4].

2.4.4.1 Open circuit voltage (V_{oc})

This is the potential difference between two terminals of a solar cell under illumination when there is no current flow through the terminals and it represents the maximum voltage a solar cell can provide to an external circuit[87]. At this point, the current will be at its minimum (zero) and the voltage across the cell is at its maximum[88,89]. V_{oc} is mainly dependent on the dark current and the generated short circuit current is shown by Eq. 1.

$$V_{oc} = \frac{kT}{q} \times \ln\left(\frac{Jsc}{Jo} + 1\right)$$

Eq. 1

The inorganic semiconductors, and the acceptor polymer play an important role in affecting the overall V_{oc} because of the energy level difference between its highest occupied molecular orbital (HOMO) and lowest un-occupied molecular orbital (LUMO)[30,90,91]. In contrast, inorganic semiconductors has the valence band (VB) and conduction band (CB) are analogous to the HOMO and LUMO respectively, hence the V_{oc} in this case depends on the difference between the VB and CB[2,78,92,93]. The lowering of the V_{oc} may be caused by manufacturing defects, resulting in a bad isolation of the electrodes and these defects eventually cause current leakage[87].

2.4.4.2 Short circuit current density (J_{sc})

This is the current density generated by the solar cell under illumination in the absence of a load potential. J_{sc} mainly dependent on the following factors:

i. **The area of the solar cell**
ii. **The number of photons** (i.e., the power of the incident light source)
iii. **The spectrum of the incident light,** for most solar cell measurement, the spectrum is standardised to the AM1.5 spectrum.
iv. **The optical properties**
v. **The collection probability of the solar cell**, which depends chiefly on the surface passivation and the minority carrier lifetime in the base.

When comparing solar cells of the same material type, the most critical parameter is the diffusion length and surface passivation[15,80,94]. In a cell with perfectly passivated surface and uniform generation, the equation for the short-circuit current can be estimated by Eq. 2

$$J_{sc} = qG\,(L_n + L_p) \qquad \textbf{Eq. 2}$$

Where q is the electron charge, G is the generation rate, and L_n and L_p are the e^- and h^+ diffusion lengths respectively. It is clear from Eq. 2 that J_{sc} depends strongly on the generation rate and diffusion length[95].

2.4.4.3 Fill factor (FF)

Fill Factor (*FF*) is essentially a measure of quality of the solar cell[88]. It is determined by comparing the maximum power (P_{max}) to the theoretical power (PT) that would be output at both the open circuit voltage and short circuit current together and it can also be interpreted from the IV as the ratio of the rectangular areas as depicted in Fig. 12[96–98]. The maximum power density is obtained between V_{oc} (V = 0) and V_{oc} at maximum voltage V_{max} and corresponding maximum current density J_{max} and hence the equation for *FF* can be deduced as indicated by Eq. 3.

$$FF = \frac{Pmax}{PT} = \frac{Jmax \times Vmax}{Jsc \times Voc}$$ **Eq. 3**

A larger fill factor is desirable and corresponds to an IV sweep that is more square-like.

2.4.4.4 Power conversion efficiency (PCE)

This is the ability of a photovoltaic device to convert sunlight into usable energy[89]. PCE is often denoted by η symbol and it is calculated as the ratio between the generated P_{max} and the incident power, P_{in}. P_{in} is equal to the irradiance of AM1.5 spectrum, normalized to 1000 W/m^2. PCE is determined from the IV measurement using Eq. 4. The maximum power output can be limited through optical losses and interfacial contact related losses[99]. The power losses can be enhanced by resistance (i.e. series and shunt, Fig. 2.15 (b)) induced by the current or leakage currents around the sides of the device and the effect can also be presented graphically (i.e. curve) and compared with the ideal I-V curve, (Fig. 2.16).

$$\eta = \frac{P_m}{P_{in}} = \frac{J_{mp} V_{mp}}{P_{in}} = \frac{J_{sc} V_{oc} FF}{P_{in}}$$ **Eq. 4**

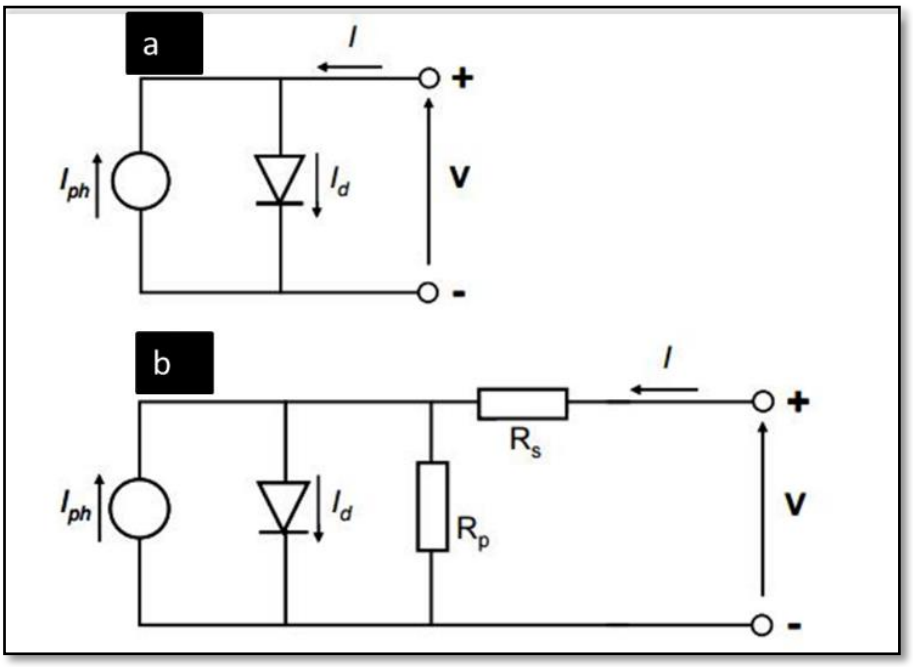

Fig. 2.15: (a) Equivalent circuit of an ideal solar cell (b) Equivalent circuit of a solar cell with series and shunt resistance. R_s is the series resistance, R_p is the shunt resistance[100].

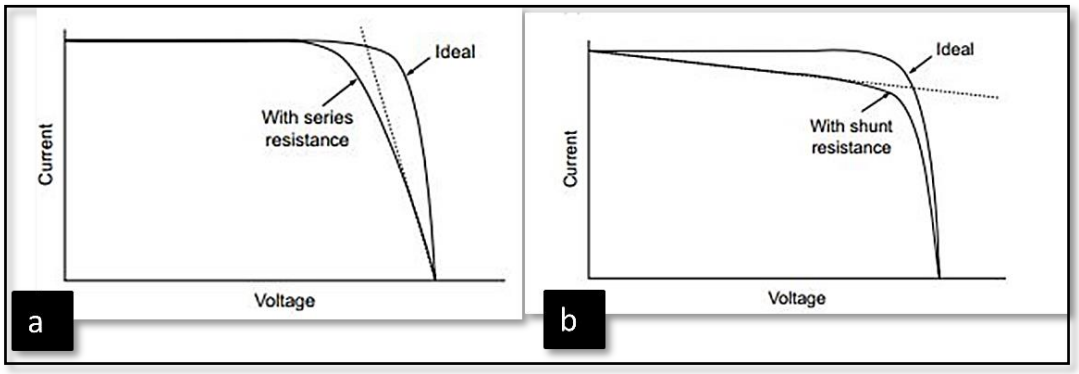

Fig. 2.16: I-V curves as a result of (a) Series resistance and (b) Shunt resistance[16].

It is also worth noting that if the reverse voltage becomes too large, the junction will breakdown and induce the current flow[78].

2.5 Progress in the study of carbon nanomaterials, perovskites and photovoltaics in general

Some research attempts had already been done using carbon nanomaterials in photovoltaics[4], lithium ion batteries8 etc. but there had always been a challenge on stability, high recombination rates and also low PCEs[4-8]. Hybrid perovskites on the other hand had climbed to a PCE of about 21 % within a short space of time[100], which drawn a big interest in the research field, however the technology is at the moment facing a boundary to be scaled up to large scale production[76-80]. This is mainly due to the fact that the inorganic-organic hybrid perovskite materials still suffer severe degradation after moisture exposure, and hence they have a very short life-span.

2.6 References

1. Deshmukh, A. A., Mhlanga, S. D. & Coville, N. J. Carbon spheres. *Mater. Sci. Eng. R Reports* **70,** 1–28 (2010).

2. Chung, I., Lee, B., He, J., Chang, R. P. H. & Kanatzidis, M. G. All-solid-state dye-sensitized solar cells with high efficiency. *Nature* **485,** 486–489 (2012).

3. Gao, M.-Y. Fullerene-like Polyoxotitanium Cage with High Solution Stability. *J. Am. Chem. Soc.* **138,** 2556–2559 (2016).

4. Mohammad Bagher, A. Comparison of Organic Solar Cells and Inorganic Solar Cells. *Int. J. Renew. Sustain. Energy* **3,** 53 (2014).

5. Tang, S., Tang, Y., Vongehr, S., Zhao, X. & Meng, X. Nanoporous carbon spheres and their application in dispersing silver nanoparticles. *Appl. Surf. Sci.* **255,** 6011–6016 (2009).

6. Cao, B. Preparation of Nitrogen-Doped Carbon Spheres by Injecting Pyrolysis of Pyridine. *ACS Sustain. Chem. Eng.* **3,** 1786–1793 (2015).

7. Zhang, J. Carbon science in 2016: Status, challenges and perspectives. *Carbon N. Y.* **98,** 708–732 (2016).

8. Chen, J. Recent Progress in Advanced Materials for Lithium Ion Batteries. *Materials (Basel).* **6,** 156–183 (2013).

9. Guldi, D. M., Rahman, G. M. A., Zerbetto, F. & Prato, M. Carbon Nanotubes in Electron Donor−Acceptor Nanocomposites. *Acc. Chem. Res.* **38,** 871–878 (2005).

10. K. L. Choy. Chemical vapour deposition of coatings. *Prog. Mater. Sci.* **48,** 57–170 (2003).

11. Carlsson, J.-O. & Jansson, U. Progress in chemical vapor deposition. *Prog. Solid State Chem.* **22,** 237–292 (1993).

12. Tyagi, V. V., Kaushik, S. C. & Tyagi, S. K. Advancement in solar photovoltaic/thermal (PV/T) hybrid collector technology. *Renew. Sustain. Energy Rev.* **16,** 1383–1398 (2012).

13. Kuang, C. Highly Efficient Electron Transport Obtained by Doping PCBM with Graphdiyne in Planar-Heterojunction Perovskite Solar Cells. *Nano Lett.* **15,** 2756–2762 (2015).

14. Yue, Z., Cai, B., Wang, L., Wang, X. & Gu, M. Intrinsically core-shell plasmonic dielectric nanostructures with ultrahigh refractive index. (2016).

15. Glunz, S. W., Preu, R. & Biro, D. *Crystalline silicon solar cells. State-of-the-art and future developments*. *Comprehensive Renewable Energy* **1,** (2012).

16. Balandin, A. A. Superior Thermal Conductivity of Single-Layer Graphene. *Nano Lett.* **8,** 902–907 (2008).

17. Jeon, C. Opening and reversible control of a wide energy gap in uniform monolayer graphene. *Sci. Rep.* **3,** 2725 (2013).

18. Nie, W. High-efficiency solution-processed perovskite solar cells with millimeter-scale grains. *Science (80-.).* **347,** 522 LP-525 (2015).

19. Lee, W. J. Nitrogen-doped carbon nanotubes and graphene composite structures for energy and catalytic applications. *Chem. Commun.* **50,** 6818–30 (2014).

20. Geim, A. K. & Novoselov, K. S. The rise of graphene. *Nat. Mater.* **6,** 183–191 (2007).

21. Bostwick, A. Observation of Plasmarons in Quasi-Freestanding Doped Graphene. *Science (80-.).* **328,** 999–1002 (2010).

22. Dai, H. Carbon nanotubes: Synthesis, integration, and properties. *Acc. Chem. Res.* **35,** 1035–1044 (2002).

23. Barreiro, A. Understanding the catalyst-free transformation of amorphous carbon into graphene by current-induced annealing. *Sci. Rep.* **3,** 1115 (2013).

24. Novoselov, K. S. A roadmap for graphene. *Nature* **490,** 192–200 (2012).

25. Schiros, T. Connecting Dopant Bond Type with Electronic Structure in N-Doped Graphene.

Nano Lett. **12,** 4025–4031 (2012).

26. Lonkar, S. P. & Abdala, A. A. Thermodynamics & Catalysis Applications of Graphene in Catalysis Graphene Oxide (GO) Reduced Graphene Oxide. *Nature*. **5,** (2014).

27. Schiros, T. Study of the electronic properties of Li-intercalated nitrogen doped graphite. *ACS Nano* **4,** 4025–4031 (2010).

28. Choi, W. & Lee, J. Graphene: Synthesis and Applications Nanomaterials and their Applications. *Science*, **3**, 394 (2011).

29. Geim, A. K. Graphene: Status and Prospects. *Science.* **324,** 1530-1534 (2009).

30. Hwang, J. O. Workfunction-tunable, N-doped reduced graphene transparent electrodes for high-performance polymer light-emitting diodes. *ACS Nano.* **6,** 159–167 (2012).

31. Li, X., Zhang, S., Wang, P. & Zhong, H. High performance solar cells based on graphene / GaAs heterostructures. *Science*. **3**, 1–23 (2014).

32. Neto, A. C., Guinea, F. & Peres, N. M. Drawing conclusions from graphene. *Phys. World*. **19,** 33–37 (2006).

33. Paulo, S., Palomares, E. & Martinez-ferrero, E. Graphene and Carbon Quantum Dot-Based Materials in Photovoltaic Devices : From Synthesis to Applications. Science. **56**, 1–20 (2016).

34. Tîlmaciu, C.-M. & Morris, M. C. Carbon nanotube biosensors. *Front. Chem.* **3,** 1–21 (2015).

35. Mwenya, T., Fan, H., Dai, H. & Li, M. The Detailed Evolution of Carbon Spheres by Hydrothermal Method. *Science*. **6,** 4-7 (2000).

36. Trogadas, P., Fuller, T. F. & Strasser, P. Carbon as Catalyst and Support for Electrochemical Energy. *Carbon N. Y.* (2014).

37. Chen, J. Mesoporous carbon spheres: Synthesis, characterization and supercapacitance. *Int. J. Electrochem. Sci.* **4,** 1063–1073 (2009).

38. Article, R. A review of shaped carbon nanomaterials. **107,** 1–15 (2011).

39. Chen, X. Synthesis , Growth Mechanism , and Electrochemical Properties of Hollow Mesoporous Carbon Spheres with ... Synthesis , Growth Mechanism , and Electrochemical

Properties of Hollow Mesoporous Carbon Spheres with Controlled Diameter. *Nature*, **33**, 194-198 (2014).

40. Li, S., Pasc, A., Fierro, V. & Celzard, A. Hollow Carbon Spheres , Synthesis and Applications - A Review. *J. Mater. Chem. A Mater. energy Sustain.* **0,** 1–28 (2016).

41. Nxumalo, E. N. & Coville, N. J. Nitrogen Doped Carbon Nanotubes from Organometallic Compounds: A Review. *Materials (Basel).* **3,** 2141–2171 (2010).

42. Li, M., Wu, Q., Wen, M. & Shi, J. A novel route for preparation of hollow carbon nanospheres without introducing template. *Nanoscale Res. Lett.* **4,** 1365–1370 (2009).

43. Liao, Y., Gao, L., Zhang, X. & Chen, J. Nitrogen-doped hollow carbon spheres with enhanced electrochemical capacitive properties. *Mater. Res. Bull.* **47,** 1625–1629 (2012).

44. Hulicova-Jurcakova, D. Highly Stable Performance of Supercapacitors from Phosphorus-Enriched Carbons. *J. Am. Chem. Soc.* **131,** 5026–5027 (2009).

45. Lu, Y.-F. Nitrogen-Doped Graphene Sheets Grown by Chemical Vapor Deposition: Synthesis and Influence of Nitrogen Impurities on Carrier Transport. *ACS Catal*. **8**, 4409 (2013).

46. Galeano, C. Nitrogen-Doped Hollow Carbon Spheres as a Support for Platinum-Based Electrocatalysts. *ACS Catal.* **4,** 3856–3868 (2014).

47. Zheng, Y., Jiao, Y., Jaroniec, M., Jin, Y. & Qiao, S. Z. Nanostructured Metal-Free Electrochemical Catalysts for Highly Efficient Oxygen Reduction. *Small* **8,** 3550–3566 (2012).

48. Liang, J., Jiao, Y., Jaroniec, M. & Qiao, S. Z. Sulfur and Nitrogen Dual-Doped Mesoporous Graphene Electrocatalyst for Oxygen Reduction with Synergistically Enhanced Performance. *Angew. Chemie Int. Ed.* **51,** 11496–11500 (2012).

49. Xu, B., Hou, S., Cao, G., Wu, F. & Yang, Y. Sustainable nitrogen-doped porous carbon with high surface areas prepared from gelatin for supercapacitors. *J. Mater. Chem.* **22,** 19088 (2012).

50. Jiao, Y., Zheng, Y., Jaroniec, M. & Qiao, S. Z. Origin of the Electrocatalytic Oxygen Reduction Activity of Graphene-Based Catalysts: A Roadmap to Achieve the Best

Performance. *J. Am. Chem. Soc.* **136,** 4394–4403 (2014).

51. Ling, X. Can Graphene be used as a Substrate for Raman Enhancement? *Nano Lett.* **10,** 553–561 (2010).

52. Wei, D. Synthesis of N-Doped Graphene by Chemical Vapor Deposition and Its Electrical Properties. *Science*. **200,** 333-339 (2009).

53. Jin, Z., Yao, J., Kittrell, C. & Tour, J. M. Large-Scale Growth and Characterizations of Nitrogen-Doped Monolayer Graphene Sheets. *ACS Nan.o* **5,** 4112–4117 (2011).

54. Dai, J., Yuan, J. & Giannozzi, P. Gas adsorption on graphene doped with B, N, Al, and S: A theoretical study. *Appl. Phys. Lett.* **95,** 232105 (2009).

55. Jeong, H. M. Nitrogen-Doped Graphene for High-Performance Ultracapacitors and the Importance of Nitrogen-Doped Sites at Basal Planes. *Nano Lett.* **11,** 2472–2477 (2011).

56. Reddy, A. L. M. Synthesis Of Nitrogen-Doped Graphene Films For Lithium Battery Application. *ACS Nano.* **4,** 6337–6342 (2010).

57. Chaban, V. V & Prezhdo, O. V. Nitrogen-Nitrogen Bonds Violate Stability of N-Doped Graphene. *Appl. Phys. Lett*. **78**, 203211 (2006)

58. Chen, H. Nitrogen Doping Effects on the Physical and Chemical Properties of Mesoporous Carbons. *J. Phys. Chem. C*. **117,** 8318–8328 (2013).

59. Zhang, S., Tsuzuki, S., Ueno, K., Dokko, K. & Watanabe, M. Upper limit of nitrogen content in carbon materials. *Angew. Chem. Int. Ed. Engl.* **54,** 1302–6 (2015).

60. Xia, Y. & Mokaya, R. Synthesis of Ordered Mesoporous Carbon and Nitrogen-Doped Carbon Materials with Graphitic Pore Walls via a Simple Chemical Vapor Deposition Method. *Adv. Mater.* **16,** 1553–1558 (2004).

61. Seredych, M., Hulicova-Jurcakova, D., Lu, G. Q. & Bandosz, T. J. Surface functional groups of carbons and the effects of their chemical character, density and accessibility to ions on electrochemical performance. *Carbon N. Y.* **46,** 1475–1488 (2008).

62. Wei, Q. Nitrogen-Doped Carbon Nanotube and Graphene Materials for Oxygen Reduction Reactions. *Catalysts* **5,** 1574–1602 (2015).

63. Chun, K.-Y., Lee, H. S. & Lee, C. J. Nitrogen doping effects on the structure behavior and the field emission performance of double-walled carbon nanotubes. *Carbon N. Y.* **47,** 169–177 (2009).

64. Czerw, R., Terrones, M. J., Charlier, J.C., Blase, X., B. F., Kamalakaran, B.F.R., Grobert, N., Terrones, H., Tekleab, D., Ajayan, P.M. W. B. & Ruhle, M. Identification of Electron Donor States in N- Doped Carbon Nanotubes. *Nano Lett.* **1,** 457–460 (2001).

65. Boncel, S., Pattinson, S. W., Geiser, V., Shaffer, M. S. P. & Koziol, K. K. K. En route to controlled catalytic CVD synthesis of densely packed and vertically aligned nitrogen-doped carbon nanotube arrays. *Beilstein J. Nanotechnol.* **5,** 219–233 (2014).

66. Chen, H. Nitrogen Doping Effects on the Physical and Chemical Properties of Mesoporous Carbons. *J. Phys. Chem. C*. **117,** 8318–8328 (2013).

67. Tao, X. Y. Large-scale CVD synthesis of nitrogen-doped multi-walled carbon nanotubes with controllable nitrogen content on a CoxMg1-xMoO4 catalyst. *Diam. Relat. Mater.* **16,** 425–430 (2007).

68. Biddinger, E. J., von Deak, D. & Ozkan, U. S. Nitrogen-Containing Carbon Nanostructures as Oxygen-Reduction Catalysts. *Top. Catal.* **52,** 1566–1574 (2009).

69. Zhang, J. Tunable electronic properties of graphene through controlling bonding configurations of doped nitrogen atoms. *Sci. Rep.* **6,** 28330 (2016).

70. Liu, H., Zhang, Y., Li, R., Sun, X. & Abou-Rachid, H. Thermal and chemical durability of nitrogen-doped carbon nanotubes. *J. Nanoparticle Res.* **14,** 1016 (2012).

71. Wang, H., Maiyalagan, T. & Wang, X. Review on Recent Progress in Nitrogen-Doped Graphene: Synthesis, Characterization, and Its Potential Applications. *ACS Catal.* **2,** 781–794 (2012).

72. Zhang, J. Tunable electronic properties of graphene through controlling bonding configurations of doped nitrogen atoms. *Sci. Rep.* **6,** 28330 (2016).

73. Zheng, B., Hermet, P. & Henrard, L. Scanning Tunneling Microscopy Simulations of Nitrogen- and Boron-Doped Graphene and Single-Walled Carbon Nanotubes. *ACS Nano* **4,** 4165–4173 (2010).

74. Jalili, S. & Vaziri, R. Study of the electronic properties of Li-intercalated nitrogen doped graphite. *Mol. Phys.* **109,** 687–694 (2011).

75. Pappas, G. Heteroatom Doped-Carbon Nanospheres as Anodes in Lithium Ion Batteries. *Materials (Basel).* **9,** 35 (2016).

76. Elgani, R. A., Hilo, M. H. M., Allah, M. D. A., Hassan, a Al & Elhai, R. A. Impact of the light intensity variation on the performance of solar cell constructed from (Muscovite / TiO 2 / Dye / Al). *Nature*. **5,** 1069–1077 (2013).

77. Bagher, A. M. Introduction to Organic Solar Cells. *Sustain. Energy* **2,** 85–90 (2014).

78. Kasap, S. pn Junction Devices and Light Emitting Diodes. *Junction Devices* **7,** 34 (2001).

79. Hersch, P. & Zweibel, K. Basic photovoltaic principles and methods. *Antimicrob. Agents Chemother.* **58,** 7250–7 (1982).

80. Markvart, T. & Castañer, L. *Principles of Solar Cell Operation*. *Practical Handbook of Photovoltaics* (Elsevier Ltd, 2012). doi:10.1016/B978-0-12-385934-1.00001-5

81. dos Santos, A. M., Beliaev, D., Scolfaro, L. M. R. & Leite, J. R. Quasi-Fermi levels, chemical and electric potential profiles of a semiconductor under illumination. *Brazilian J. Phys.* **29,** 775–778 (1999).

82. Zhao, Y. & Zhu, K. Charge Transport and Recombination in Perovskite (CH3NH3)PbI3 Sensitized TiO2 Solar Cells. *J. Phys. Chem. Lett.* **4,** 2880–2884 (2013).

83. Servaites, J. D., Ratner, M. A. & Marks, T. J. Organic solar cells: A new look at traditional models. *Energy Environ. Sci.* **4,** 4410–4422 (2011).

84. Wang, J. Promising photovoltaic application of multi-walled carbon nanotubes in perovskites solar cells for retarding recombination. *RSC Adv.* **6,** 42413–42420 (2016).

85. Liu, J. Two-Dimensional CH3NH3PbI3 Perovskite: Synthesis and Optoelectronic Application. *ACS Nano.* **10,** 3536–3542 (2016).

86. Pierret, R. F. Advanced Semiconductor Fundamentals. *Book.* **121,** 221 (1987).

87. Krebs, F. C. Indium Tin Oxide-Free Polymer Solar Cells : Toward Commercial Reality Indium Tin Oxide-Free Polymer Solar Cells : Toward Commercial Reality. *Nature*. **8**, 333

(2014).

88. Gupta, D., Mukhopadhyay, S. & Narayan, K. S. Fill factor in organic solar cells. *Sol. Energy Mater. Sol. Cells* **94,** 1309–1313 (2010).

89. Lin, Q., Armin, A., Burn, P. L. & Meredith, P. Organohalide Perovskites for Solar Energy Conversion. *Acc. Chem. Res.* **49,** 545–553 (2016).

90. Facchetti, A. Polymer donor – polymer acceptor (all-polymer) solar cells. *Mater. Today* **16,** 123–132 (2013).

91. Spanggaard, H. & Krebs, F. C. A brief history of the development of organic and polymeric photovoltaics. *Sol. Energy Mater. Sol. Cells* **83,** 125–146 (2004).

92. Im, J.-H., Chung, J., Kim, S.-J. & Park, N.-G. Synthesis, structure, and photovoltaic property of a nanocrystalline 2H perovskite-type novel sensitizer (CH3CH2NH3)PbI3. *Nanoscale Res. Lett.* **7,** 353 (2012).

93. Kalb, W. L. & Batlogg, B. Calculating the trap density of states in organic field-effect transistors from experiment: A comparison of different methods. *Phys. Rev. B - Condens. Matter Mater. Phys.* **81,** (2010).

94. Gonzalez-Pedro, V. General working principles of CH3NH3PbX3 perovskite solar cells. *Nano Lett.* **14,** 888–893 (2014).

95. Jung, H. S. & Park, N. G. Perovskite solar cells: From materials to devices. *Small* **11,** 10–25 (2015).

96. Gupta, D. Fill factor in organic solar cells , *Science*. **55,** 2–7 (2010).

97. Wang, Q. Large fill-factor bilayer iodine perovskite solar cells fabricated by a low-temperature solution-process. *Energy Environ. Sci.* **7,** 2359 (2014).

98. Mei, A. A hole-conductor–free, fully printable mesoscopic perovskite solar cell with high stability. *Science (80-.).* **345,** 295–298 (2014).

99. Chu, P. K. & Li, L. Characterization of amorphous and nanocrystalline carbon films. *Mater. Chem. Phys.* **96,** 253–277 (2006).

100. Im, J.-H., Chung, J., Kim, S.-J. & Park, N.-G. Synthesis, structure, and photovoltaic property

of a nanocrystalline 2H perovskite-type novel sensitizer (CH3CH2NH3)PbI3. *Nanoscale Research Letters* **7,** 353 (2012).

Chapter 3

Investigation of N-bHCSs effect on the electronic, optical and photovoltaic properties of a P3HT:PCBM active layer

3.1 Introduction

3.1.1 Carbon nanomaterials

The discovery of the new polyhedral carbon clusters, mostly sp^2 bonded with nano-scale dimensions such as fullerene, in 1985, single walled nanotubes in 1991, and graphene in 2004 has driven an increased interest in the study of shaped carbon nano-materials (SCNMs) especially the carbon nanomaterials (CNMs) constrained at the nanoscale[1–3]. All these materials exhibit physicochemical properties, which gives them advantages in current carbon research fields[3]. CNMs can take a spherical shape as seen in fullerenes, and they had been exploited recently for many uses including their application in lithium ion batteries, energy storage, paintings, drug delivery systems, catalyst supports, tires, high strength composites, lubricants and also, for the dispersion of silver nanoparticles and so forth[4–6].

Carbon spheres (CSs) possess electron accepting properties, hence they have been used recently in organic solar cells as electron accepting materials[7]. CSs can be synthesized by methods such as pyrolysis, chemical vapor deposition (CVD) and so forth and depending on the type of method employed, different micro structures are obtained, which in turn influences their electrochemical properties[6,8,9]. Some other shapes adopted by carbon include onions and these materials differ in terms of the number of carbon layers and their size (spheres>onions), and these materials have a hollow centre[10].

All these carbon shapes adopt basic low dimensional forms but combining them into more complex 3D architectures is still a challenge[11]. A most imperative feature adopted by a hollow SCNM is their hollow centre which offers an advantage of modifying the shell thickness of the carbon sphere[12]. These materials are called hollow carbon spheres (HCSs). Alternatively, the hollow could be partially filled with a small particle (or particles) to give a rattle core-shell or yolk-shell type structure.

Modification of the (hydrophobic) pore structure of the carbon allotropes is also critical and this can be done by using heteroatoms (doping with boron, nitrogen and other heteroatoms) into the lattice of CNMs (i.e. N-CNMs)[13,14]. Some examples of the N-doped CNMs includes carbon nanotubes (CNTs), CSs covered in this study and many more for various application related to enhancement of the electronic properties of pristine CNMs[14;18].

The practice of doping CNMs with surface heteroatoms could cause electron modulation in order to provide appropriate electronic structures for many impending applications[15]. N-CNMs have been employed in many applications, including the enhancement of specific capacitance[13], for use in making anode materials in Li-ion batteries by improving the electrochemical performance of carbon materials[6], as a support for platinum-based electro-catalysts[16] and in many other uses of practical significance, the nitrogen in N-CNMs can improve conductivity, enhance the interface with molecules, and change the oxidation stability and catalytic activity of metals attached to the N-CNMs[17–20].

N-doping also results in redistribution of the spin and charge density states in CNMs[21–26]. Many studies have employed two approaches to dope CNMs; *in-situ* and *ex-situ* (post-doping) doping approaches[27]. *In-situ* doping approach involves the incorporation of nitrogen atoms during the CNMs growth and the *ex-situ* techniques involves post-treatment of pre-prepared CNMs with a nitrogen-containing precursor such as NH_3. Both doping approaches have their own benefits. *In-situ* doping can incorporate nitrogen atoms into the entire carbon nanomaterials homogeneously whereas *ex-situ* doping often leads to surface functionalization only of CNMs without modification of their bulk properties[15].

Silica spheres have been widely studied ever since their first emergence, propelled by Stober[12]. Synthetic SiO_2 can either exist in crystalline or amorphous forms[28]. Silica is used as a template for the synthesis of carbon nanomaterials taking advantage of their manupulative sizes[29,30]. Although the practice of using silica as a template is cheape, it still requires the use of a strong base or hydrofluoric acid for etching to produce HCSs[29]. Fig. 3.1, shows an example of a template-assisted (i.e. silica) synthesis of multi-shelled carbon hollow spheres with an ultralarge pore volume[31].

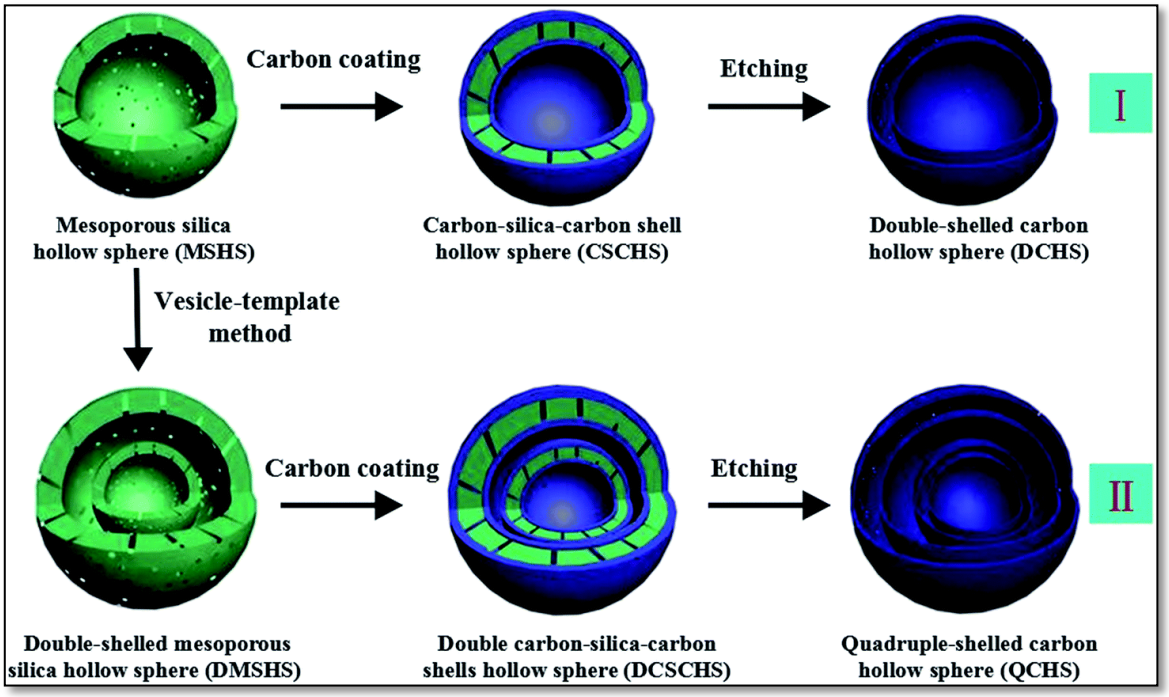

Fig. 3.1: Schematic illustration for producing double/quadruple-shelled carbon hollow spheres. Step I and II show the porous template assisted synthesis of double-shelled carbon hollow spheres and double-shelled silica hollow sphere as template, respectively[32].

It has recently been found that the dispersity of silica spheres can also be controlled by either adding tetra ethyl orthosilicate (TEOS) slowly or fast giving polydispersed or monodispersed silica spheres, respectively[33]. As compared to many traditional synthetic methods, the template method is an effective method that can be employed to synthesize CNMs, with control of morphology, particle size and structure during their preparation[32,34,35]. SiO_2 spheres are an example of a widely used template[36,37] and is an example of a hard template amongst others such as polymer microspheres, carbon fiber and porous anodic aluminium oxide[38]. Synthetic SiO_2 spheres with core shell structure have also been widely used in many recent studies, using sodium silicate as SiO_2 precursor, cetyltrimethyl ammonium bromide (CTAB) as surfactant, and methanol as co-surfactant[39].

3.1.2 Applications of carbon nanomaterials in photovoltaic devices

Polymer bulk heterojunction (BHJ) solar cells have recently received a lot of attention in research fields due to their promising power conversion efficiencies (PCEs) which had reached PCEs of up to 10 %. A polymer BHJ utilizes two polymer (donor/acceptor) materials (e.g. poly(3-hexyl-thiophene) (P3HT) and phenyl-C61-butyric acid methyl ester (PCBM)) which are closely mixed together to form continuous donor and acceptor networks[40]. The adavantages of polymer BHJ

technology includes the fact that they are solution processible, which makes their production very inexpensive and they also have a good charge carrier collection[41]. Although this technology is promising for use in solar cells (eg. Silicon based solar cells), its commercial vailability is still an issue because of some drawbacks. Some of these drawbacks include fast degredation rates and low efficiencies[29,42,43]. Many attempts have been made to incorporate various materials into a solar cell device to enhance charge transfer between donor and acceptor materials, and thus increase the PCEs[40]. Some of the research approaches include incorporation of additives such as diodooctane[44], addition of carbon nanomatrials such as carbon nanotubes[45], introduction of buffer layers[40] etc.

In this work we have studied the effect of incorporating nitrogen doped broken hollow carbon spheres (N-BHCSs) into the electronic and photovoltaic properties of polymer composite based on a C60 bucky ball derivarive which acts as an acceptor, PCBM and a semicrystalline regioregular P3HT as a donor. Fig. 3.2, (a and b) shows the chemical structures of P3HT and PCBM, respectively. P3HT was selected in this work because of its absorption edge around 650 nm, its high hole mobility of about 0.1 cm^2/Vs and P3HT based solar cells with PCE over 3 % have been reported[38,46,47]. PCBM was selected also because of it's absorption edge which matches that of P3HT at around 600 nm[46] making the most optimal polymer blend for the aim of this study.

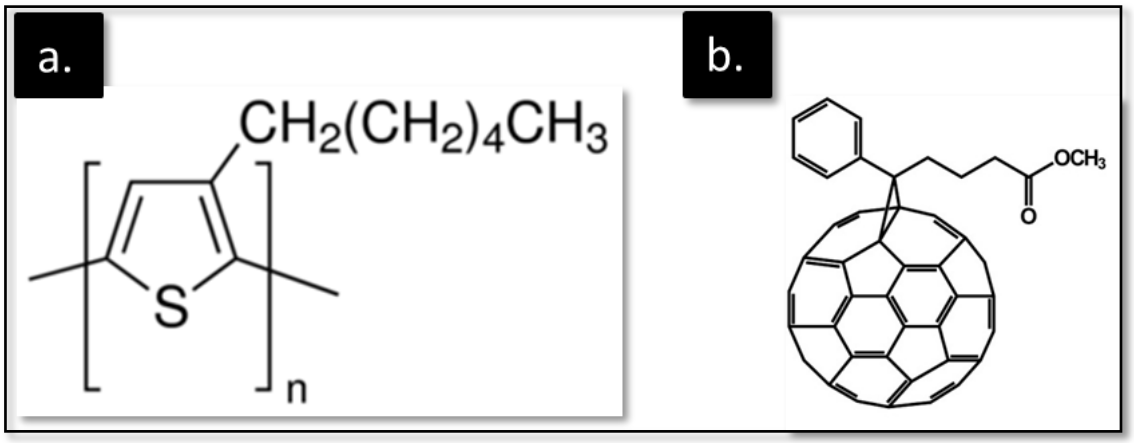

Fig. 3.2: Chemical structure of (a) P3HT; (b) PCBM[5] .

3.2 Experimental

3.2.1 Synthesis of monodispersed and polydispersed SiO_2 spheres

A large quantity of SiO_2 spheres was synthesized using a well-known Stober method[37] modified by Mutuma and co-workers[48]. The process involved mixing ethanol (90 mL), distilled water (dH_2O, 63 mL) and NH_4OH (5 mL) together. The solution was stirred for 25 min at room temperature. TEOS (16 mL) was *slowly* added to the mixture to achieve polydispersity of SiO_2 spheres and *fast* addition to achieve monodisperse SiO_2 spheres and the reaction stirred for a further 1 h. The solutions were then centrifuged at 15000 rpm for 10 min, washed with dH_2O (5 mL) followed by few a drop of ethanol and dried overnight at 80℃.

3.2.2 Synthesis of N-BHCSs: horizontal chemical vapor deposition

A succinct description of chemical vapor deposition (CVD) refers to an atomistic deposition method that involves the formation of a thin solid film on a heated substrate surface[8,49]. The horizontal CVD (H-CVD) method has been widely employed to synthesize various N-doped carbon materials. In this technique, a substrate material such as silica is placed in a quartz tube which is placed into a furnace at a temperature of 600 to 1100 ℃, (Fig. 3.3). The carbon or nitrogen-containing precursor is passed over the substrate with the assistance of a carrier gas such as H_2, Ar etc. which then carbonizes and coats the substrate[50].

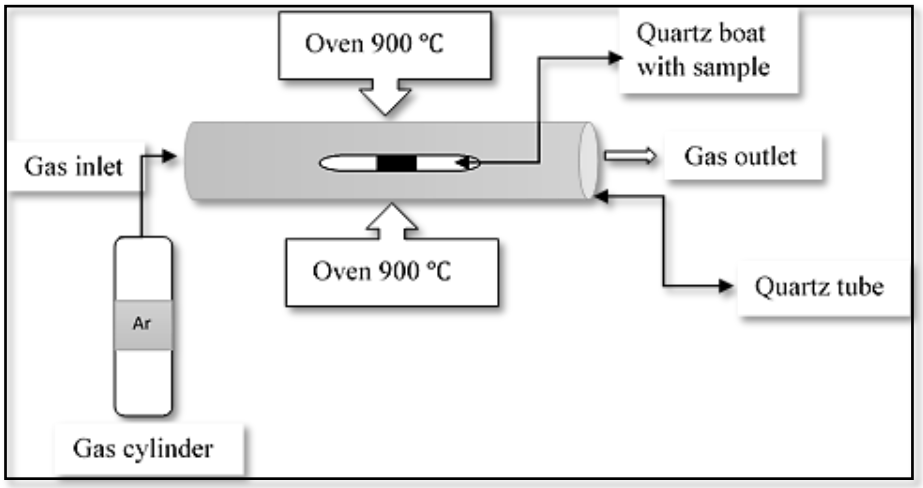

Fig. 3.3: Representative scheme of an H-CVD setup.

The synthesis of nitrogen doped broken hollow carbon spheres (N-bHCSs) was done using the H-CVD method. The chemical, physical and optical properties of materials synthesized using both in-situ and ex-situ N-doping techniques were compared before and the best candidates were selected

for further studies on electronic properties on XPS and FTIR and also application in photovoltaic devices as doping agents for P3HT: PCBM blends. Polydispersed and monodispersed SiO_2 were pre-weighed (1.5 g) in a quartz boat. Toluene was used as a carbon source to make pristine broken hollow carbon spheres (bHCSs) and as a first layer on ex-situ N-doping.

The synthesis of pristine bHCSs involved polydispersed SiO_2 that were first put in a furnace, ramping for 1 h to get to 900 ℃ under Ar gas and finally carbonization by passing through toluene at a constant temperature. Ex-situ N-doping was done by first covering polydispersed silica spheres with carbon using toluene as a carbon precursor, followed by C/N using pyridine to give P@T, N-bHCSs (P = pyridine, T = toluene) and alternatively acetonitrile to yield A@T, N-bHCSs (A = acetonitrile). In-situ N-doping was done using acetonitrile to yield A@N-bHCSs and pyridine to yield P@N-bHCSs. All the experiments were done under argon (Ar) gas passed at a (flow rate of 100 sccm) at a temperature of 900 ℃, (Table 1).

After carbonization of all material, silica was etched out using 10 % hydrofluoric acid (HF) to achieve N-bHCSs and pristine bHCSs. All performed experiments are listed in Table 1 and the produced materials with the notations are listed in Table 2.

Table 1: Synthesis of N-bHCSs and pristine bHCSs.

Experiments	**Temperature (℃)**	**CVD Time (h)**	**Flow rate (sccm)**
Pristine, *In-situ* and *ex-situ*	900	1.5	100)

Table 2: N-BHCSs materials synthesized.

Experiments	**C/N source**	**N-bHCSs**	**Notation used**
in-situ N-doping	Acetonitrile Pyridine	Acetonitrile based Pyridine based	A@N-bHCSs P@N-bHCSs
ex-situ N-doping	Acetonitrile Pyridine Toluene	Acetonitrile/Toluene based Pyridine/Toluene based	A@T,N-bHCSs P@T,N-bHCSs

3.2.3 Preparation of the ITO/PEPOT:PSS/P3HT:PCBM:N-bHCSs/Al thin films

3.2.3.1 Cleaning of ITO-glass substrate

The ITO-glass substrate was first etched with ZnO slurry and 10M HCl applied on the ITO-coated side. The conductivity of the ITO was first checked using the multimeter. The substrate was then washed with soap water while rubbing the surfaces to remove any adhering materials and then rinsed with dH_2O. The substrate was then a sonicated in dH_2O for 15 min, rinsed with dH_2O, sonicated in acetone for 15 min to remove any small particles on the surface, rinse with dH_2O, sonicated in EtOH for 15 min to activate the surface, add small portion of dH_2O and sonicated for further 5 min then take out the substrate. It was then dried under stream of N_2 air. The procedures for substrate cleaning are illustrated in the flow diagram below.

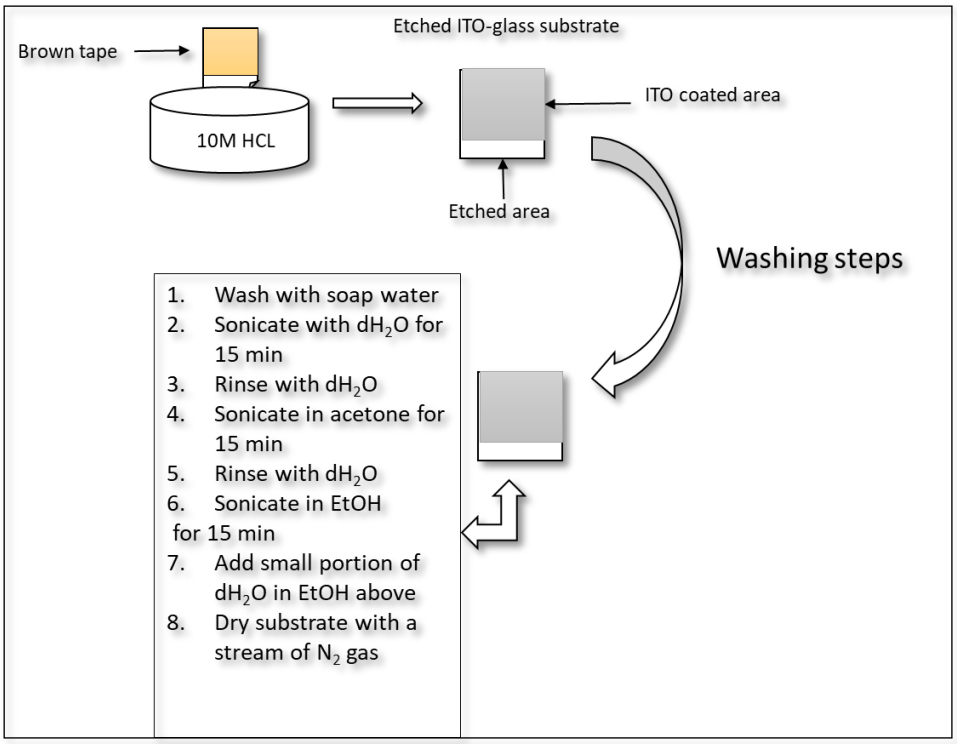

Fig. 3.4: Schematic illustration of the ITO-glass substrate etching and cleaning process.

3.2.3.2 preparation of the P3HT:PCBM:N-bHCSs blends

Fig. 3.5 shows a schematic illustration of the preparation of N-bHCSs:P3HT:PCBM blends. P3HT and PCBM (20 mg of each) were dissolved in trichlorobenzene (1 ml) separately and stirred for 1 h at room temperature. All N-bHCSs (1 mg of each) were dispersed in trichlorobenzene (1 mL) and stirred for 1 h at room temperature. The P3HT and PCBM solutions were then filtered using a 0.22

μm microfilter. A blend of P3HT: PCBM was then prepared in 1:1 ratio and mixed thoroughly. N-bHCSs:P3HT:PCBM were then prepared at a ratio of 0.1: 0.1: 0.1 ratio to achieved the blends listed in Table 3. The ratios were chosen in such a way that N-bHCSs loading was lower than that of P3HT: PCBM blend (1:1) and the reason behind this was to minimize shorting on the solar cell device which can be caused by large size of the spheres [33].

.

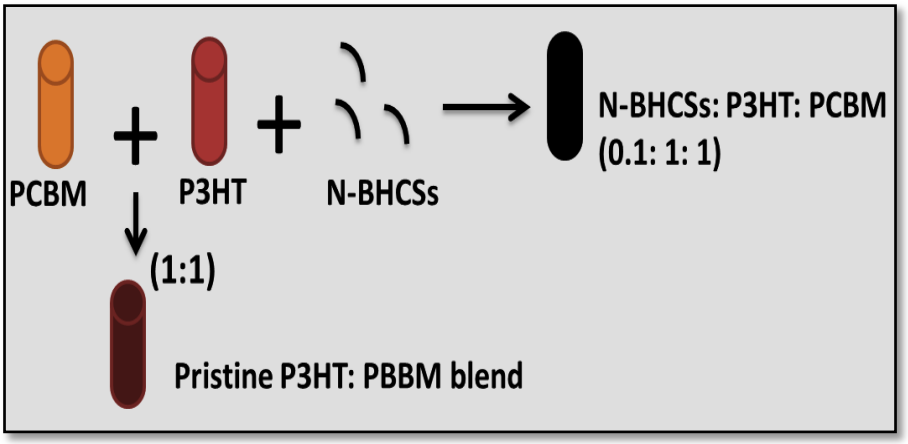

Fig. 3.5: Schematic illustration of P3HT:PCBM:N-bHCSs preparation.

Table 3: List of all prepared N-bHCSs doped P3HT: PCBM blends

Type of materials used	Blends
Pristine bHCSs	P3HT:PCBM
in-situ based N-bHCSs	P@N-bHCSs:P3HT:PCBM A@N-bHCSs:P3HT:PCBM
ex-situ based N-bHCSs	P@T, N-bHCSs:P3HT:PCBM A@T, N-bHCSs:P3HT:PCBM

3.2.4 Characterization of SiO_2, pristine HCSs, N-bHCSs and N-bHCSs:P3HT:PCBM blends

3.2.4.1 Transmission electron microscopy (TEM)

The morphological features of the synthesized SiO_2 spheres, pristine bHCSs and N-bHCSs were determined by TEM using a FEI Technai G2 spirit electron microscope operating at 120 keV. All samples were prepared by dispersing about 1 mg of the synthesized materials in 1 ml of ethanol and the mixture sonicated to form a homogeneous solution. A few drops of the homogeneous solution were placed onto a carbon coated copper grid and the grid dried in ambient air for 30 min before

inserting it in the microscope. The diameters of the carbon sphere images obtained were measured using image J 1.48v software. The diameters of 120 randomly chosen N-bHCSs and SiO_2 materials were measured per sample and the data plotted using Origin lab 8.50.

3.2.4.2 Scanning electron microscopy (SEM)

The morphology of the obtained SiO_2 spheres, pristine bHCSs and N-bHCSs were determined using a FEI Nova Nanolab 600 FIB/SEM. 1 mg of all samples was dispersed in ethanol (1 mL) and homogenized using a sonicator. One drop of the solution was placed on a carbon tape placed on a carbon stub. After drying the samples were then coated with a palladium/gold coating for 2 min to induce conductivity. The stub was then placed in a SEM and images were taken at 5 keV.

3.2.4.3 Raman spectroscopy

Raman spectroscopic analysis was done to determine the degree of graphitization and the structure of the pristine bHCSs and N-bHCSs. The measurements were carried out on the bright areas of the materials using a Jobin-Yvon T6400 micro-Raman spectrometer equipped with a laser excitation wavelength of 514.5 nm and a liquid N_2 cooled charge coupled device detector. The obtained Raman bands were deconvoluted using a Lorentzian function. The peak areas and intensities were measured using the Origin 8.50 package.

3.2.4.4 Thermal gravimetric analysis (TGA)

A TGA instrument conjugated with a weight loss derivative curve (DTG) was used to measure the thermal stability of the prepared pristine bHCSs and N-bHCSs using a Perkin Elmer Pyris 1 TGA. Each sample (10 mg) was placed in a ceramic pan and put in the instrument furnace. The sample was heated from 35^0C to 900^0C at a rate of 10^0C/min under air (10 mL/min). The weight loss plot (TGA) provided information about the stability, nature and composition of the samples. The derivative curve provided information of the weight loss and temperatures as which it took place.

3.2.4.5 Photoluminescence spectroscopy (PL

Photoluminescence (PL) measurements were carried out using a Varian PL spectrophotometer, in the wavelength range 525–800 nm, with excitation wavelength of 514.5 nm.

3.2.4.6 Atomic Force Microscopy

The surface roughness and topographic images of the pristine and N-bHCSs doped P3HT: PCBM films were studied using a Veeco Di3100 AFM in tapping mode installed with a Si_3N_4 tip.

3.2.4.7 Current-voltage characterization

Current-voltage characteristics were done using a HP4141B DC source model under 1.5 Air mass (100 mW/cm^2 illumination).

3.2.4.8 X-ray photoelectron spectroscopy (XPS)

The chemical composition of N-bHCSs, electronic states and bonding configurations of nitrogen atoms on carbon framework was determined by X-ray photoelectron spectroscopy (XPS). The ex-situ XPS study was carried out on N-bHCSs.

3.3 Results and Discussion

3.3.1 The effect of TEOS addition on SiO_2 spheres dispersity and their effect on pristine bHCSs

The effect of SiO_2 dispersity on the structure of N-bHCSs was investigated in this study. The SEM and TEM images of the SiO_2 spheres are shown in Fig. 3.6. The images reveal important synthesis information. The TEOS addition determined the size distribution and morphology of the SiO_2 spheres. Fig. 3.6 (b) shows a polydispersion of SiO_2 spheres (105 – 200 $\pm$5 nm) as a result of the *slow* addition of TEOS. Fig. 3.6 (a) on the other hand shows that the fast addition of TEOS gave a monodispersion of SiO_2 spheres (130 $\pm$ 3 nm). A similar trend was observed in a study carried out by Masalov and co-workers using the concept of "interrupted particle growth" where TEOS was added after different time intervals[51]. The study carried by Mutuma and co-workers also revealed similar trend[48]. This method implies that different/ independent nucleation sites are formed after the addition of TEOS[36].

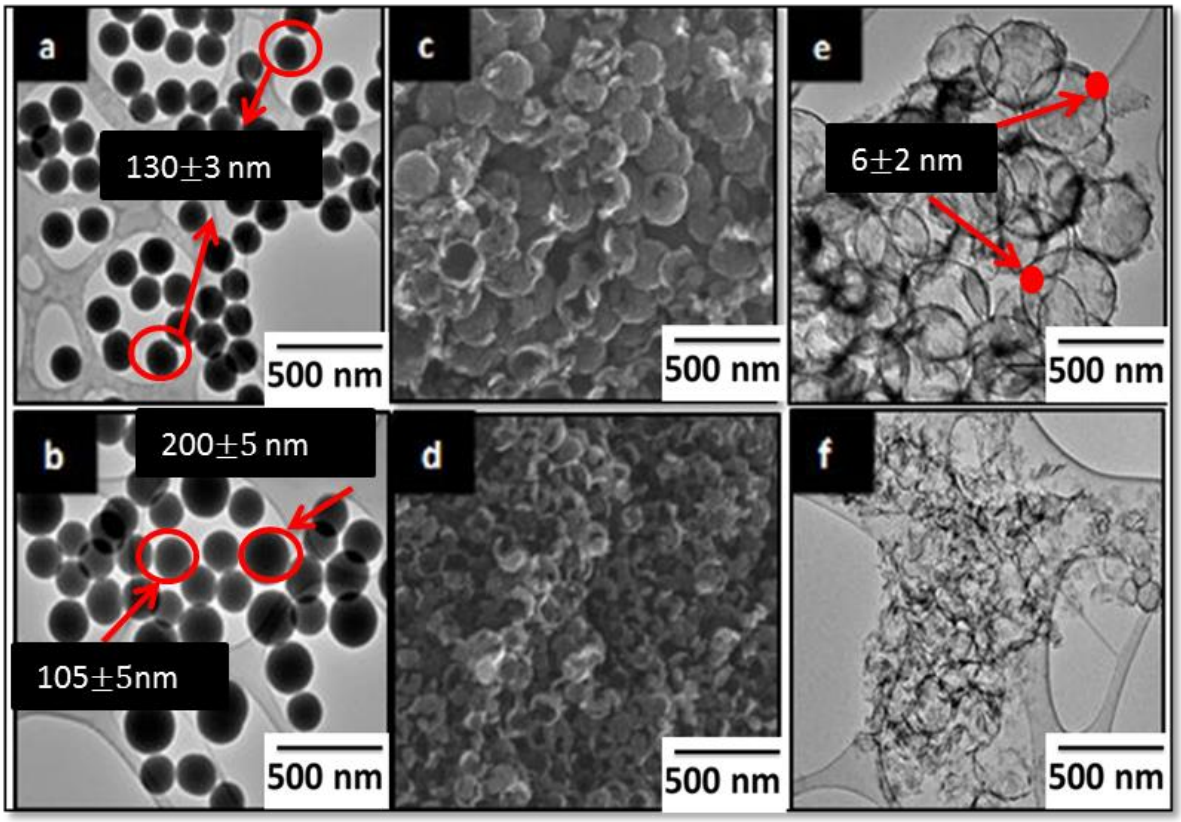

Fig. 3.6: SEM images of (a) Monodispersed SiO_2 spheres; (b) Polydispersed SiO_2 spheres; (c) Pristine bHCSs from monodisperse SiO_2 spheres; (d) Prisine bHCSs from polydisperse SiO_2 spheres; (e) and (f) corresponding TEM images of (c) and (d) respectively.

SEM images and their corresponding TEM images, Fig. 3.6 (c-e) and Fig. 3.6 (d-f), shows how the dispersity of the SiO_2 spheres influences the overall morphology of the pritine broken hollow carbon spheres (bHCSs).It was shown that monodispersed SiO_2 spheres yield partially broken pristine bHCSs, Fig. 3.6 (c-e). where as polydispersed SiO_2 spheres yields fully broken pristine bHCSs, Fig. 3.6 (d-f). The explanation of the breakages enhanced by the polydispersion of SiO_2 spheres is still not fully understood. Polydispersed SiO_2 spheres were selected as optimal materials to achieve N-bHCSs needed for this study.

3.3.2 Morphology studies on the N-bHCSs

N-bHCSs were synthesized using polydispersed SiO_2 spheres, employing *in-situ* and *ex-situ* doping techniques. Their morphology was studied using TEM and SEM. Polydispersed SiO_2 spheres showed a very smooth morphology with sizes ranging from 105- 200 nm, (Fig. 3.7(a)). A rough

morphology was revealed upon coating the SiO_2 spheres with nitrogen containing carbon sources, (Fig. 3.7 (b)). A clear breakage of carbon spheres steered by the use of polydispersed SiO_2 spheres was demonstrated in this work, this was first demonstrated by Mutuma and co-workers for materials that did not contain nitrogen[33]. Fig. 3.7 (c) reveals a partial breakage of the *ex-situ*-based N-bHCSs, with shell thickness of 6 $\pm$ 2 nm. The result of partial breakage is mainly due to the formation of dense/ multiple layers of C or C/N. Completely broken spheres were revealed in materials made by *in-situ* doping, (Fig. 3.7 (d)). Here the inner cavity was encapsulated by carbon shells with thickness of 6 $\pm$ 2 nm.

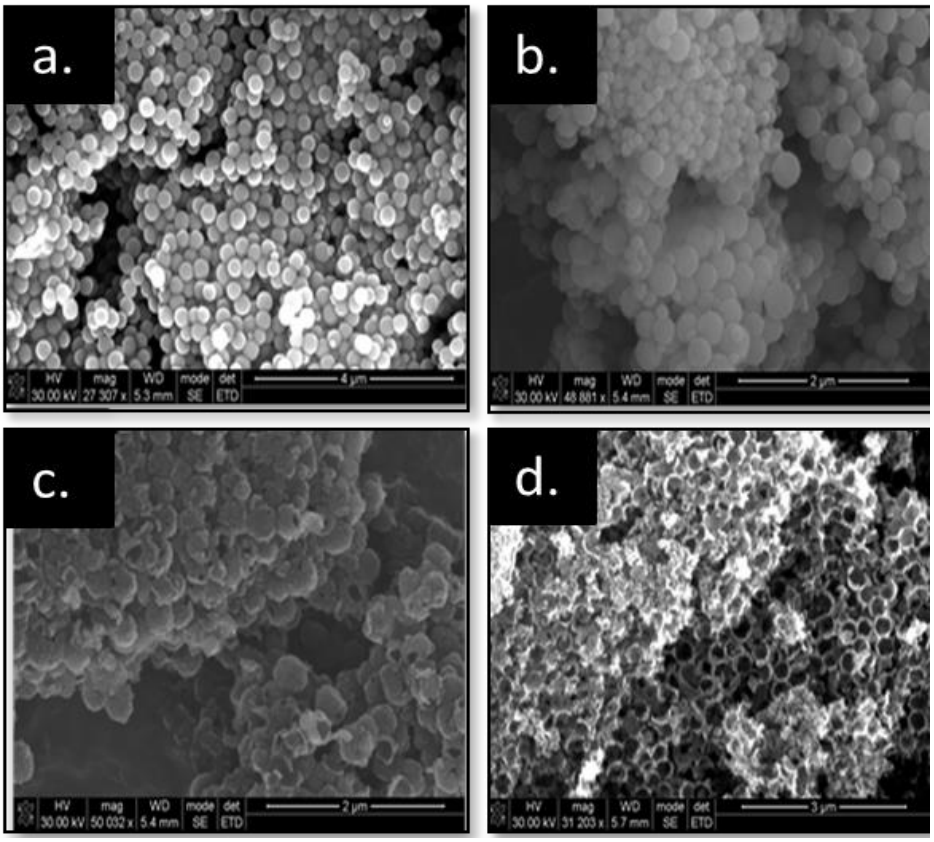

Fig. 3.7: SEM images of (a) polydispersed SiO2 spheres; (b) SiO2@C@C/N; (c) Ex-situ based N-bHCSs (i.e. A@T,N-bHCSs) ; (d) In-situ based N-bHCSs (i.e. A@N-bHCSs). Note: only acetonitrile doped materials images were selected; the pyridine based materials (i.e. P@T,N-bHCSs and P@N-bHCSs) showed similar breakage trends**.**

3.3.3 Raman spectroscopy analysis

Raman data was used to investigate the structural and surface chemistry of the bHCSs. The Raman spectra in Fig. 3.8 (a-b), reveals two characteristic peaks at 1339- 1380 nm and 1579 - 1586 nm which correspond to the D and the G bands respectively. The D band is attributed to the presence of

disordered amorphous carbon and double resonance effects in sp^2 carbon, while the G band is attributed to the E_{2G} vibration mode that is present due to the sp^2 bonded graphitic carbon[52]. The presence of the G band further endorses the presence of graphitic domains in the N-bHCSs[52]. The D band to G band intensity ratio (I_D / I_G) is used to measure the degree of defects in the N-bHCSs and is inversely proportional to the crystallite dimensions[19].

All the synthesized N-bHCSs, including pristine bHCSs had a high degree of graphitization as shown by their low I_D/I_G ratios of less than 1 as shown in Table 3. However, the degree of graphitization on N-bHCSs materials was higher than that of pristine bHCSs, this was attributed to the fact that when nitrogen is incorporated to the carbon framework, it induces more defects and this was revealed by their I_D/I_G ratios which were lower than those pristine carbon.

Other important information indicated in Fig. 3.8, is the G-band which shifted to lower values. This showed that by doping bHCS with N more defects were introduced and hence there was less sp^2 bonded graphitic carbon and more sp^3 dangling bonds[52].

The results were compared with results obtained by Dr Bridget Mutuma and colleagues on pristine bHCS[48]. The I_D/I_G ratio was also found to be much lower than that obtained in their study which is expected and also in-line with the pristine bHCSs made in this study. The trend implies that N-doping of bHCSs introduced more defects than those reported in the literature[48].

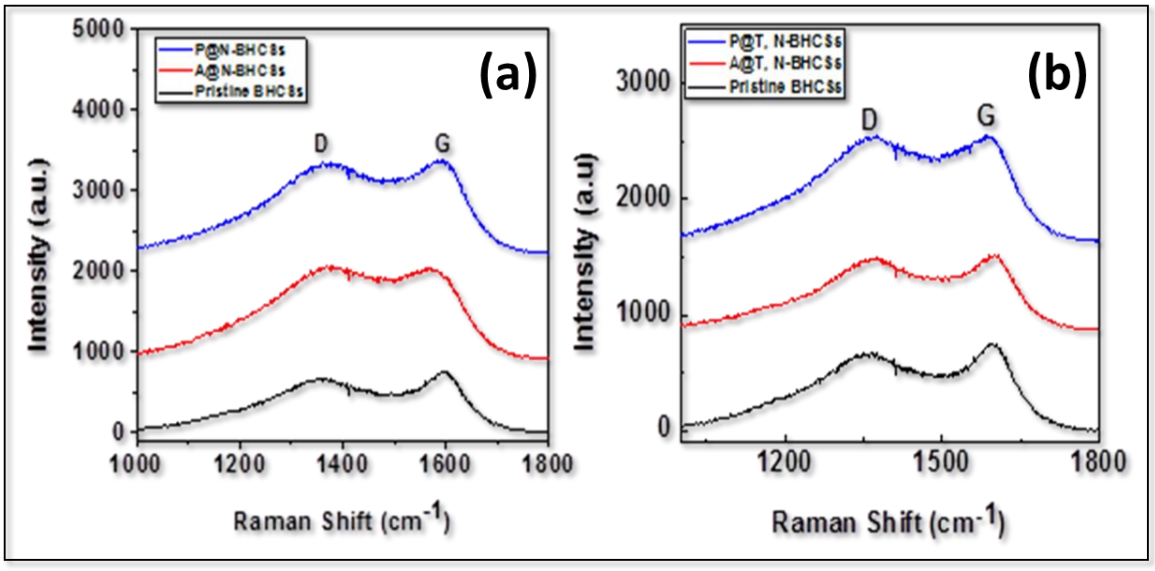

Fig. 38: Raman spectra of the synthesized bHCSs, (a) Black = pristine bHCSs; Blue = P@N-bHCSs; Red = A@N-bHCSs; (b) Black = pristine bHCSs; Blue = P@T, N-bHCSs; Red = A@T, N-bHCSs.

Table 4: The D and G band positions and I_D/I_G ratio of the *ex-situ*-based N-bHCSs, *in-situ* based N-bHCSs and pristine bHCSs

Sample	Description	I_D (cm^{-1})	I_G (cm^{-1})	I_D/I_G
Pristine bHCSs	Un-doped carbon	1354	1597	0.90
P@N-bHCSs	Pyridine based *in-situ* doped bHCSs	1354	1593	0.88
A@N-bHCSs	Acetonitrile based *in-situ* doped bHCSs	1354	1588	0.87
P@T, N-bHCSs	Pyridine based *ex-situ* doped bHCSs	1353	1594	0.88
A@T, N-bHCSs	Acetonitrile based *ex-situ* doped	1354	1590	0.89

3.3.4 TGA analysis

The thermal stability of all the synthesized carbon materials showed a consistent trend as expected. The thermal stability was determined by the TGA technique and the corresponding derivative curves, (Fig. 3.9). The thermal stability of N-bHCSs was compared to that of pristine bHCSs. It can be deduced that the thermal stability of N-bHCSs was reduced significantly, as marked lower onset decomposition temperature followed by lower temperatures at the completion of decomposition, of which ideally it revealed a fast decomposition rate of N-bHCSs, (Table 5). This observation was consistent with the Raman spectra, (Fig. 3.8). This was attributed to the disorder induced onto the carbon framework of these materials and reducing their thermal stability.

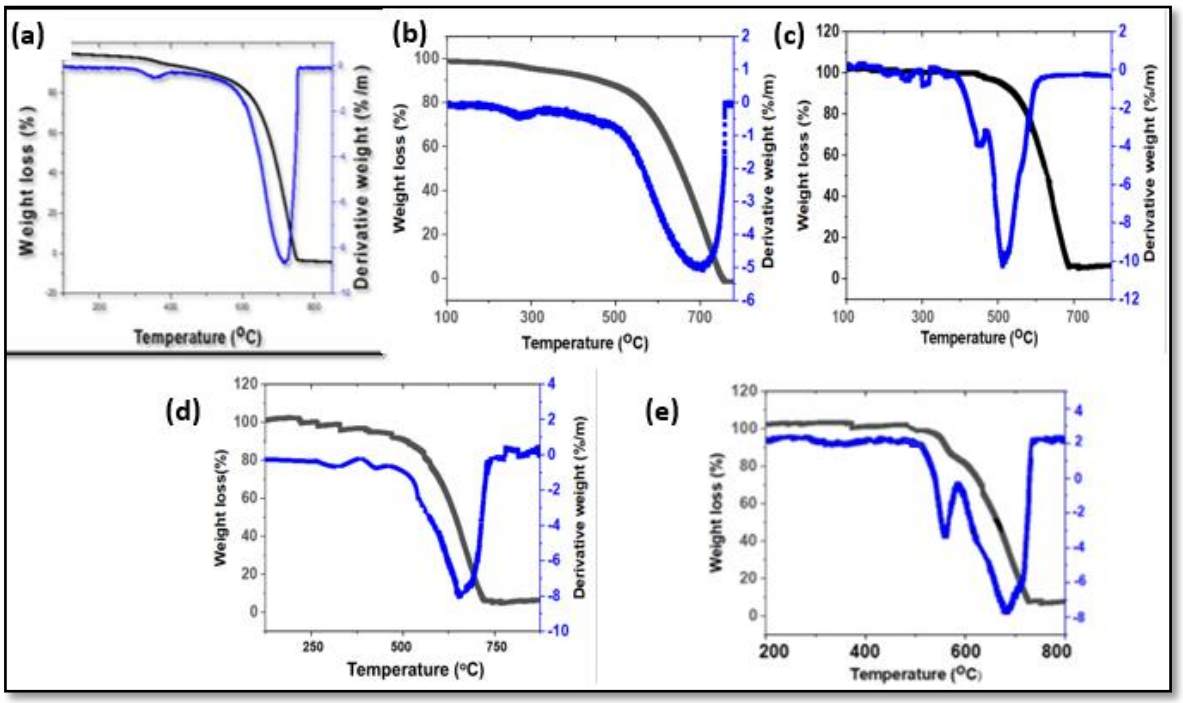

Fig. 3.9: Thermal gravimetric curves of the obtained bHCSs (a) Pristine bHCSs; (b) A@N-bHCSs; (c) A@T, N-bHCSs; (d) P@N-bHCSs and (e) P@T, N-bHCSs.

Table 5: Decomposition temperatures of *ex-situ*-based N-bHCSs, *in-situ* based N-bHCSs and pristine bHCSs

Sample	**Onset decomposition temp. (^{o}C)**	**Complete decomposition temp. (^{o}C)**
Pristine bHCSs	650	750
P@N-bHCSs	560	710
A@N-bHCSs	520	680
P@T, N-bHCSs	530	680
A@T, N-bHCSs	580	710

3.3.5 Optical and electronic properties of N-bHCSs and N-bHCSs doped P3HT: PCBM blends

3.3.5.1 XPS analysis

Fig. 3.10 shows survey XPS spectra with three dominant peaks corresponding to carbon (C1s), nitrogen (N1s) and oxygen (O1s). The presence of these peaks reveals a high purity of the N-bHCSs. The absence of N1s on pristine bHCSs spectrum also confirms the purity of these materials

and well fit for comparison with N-bHCSs. The elemental atomic percentage of each species in pristine bHCSs is also listed in Table 6, revealing C1s being the dominant as compared to O1s. It is also revealed that nitrogen atoms in N-bHCSs were lower than carbon atoms as expected. It is also revealed that the N1s contents of both P@N-bHCSs and A@N-bHCSs were similar.

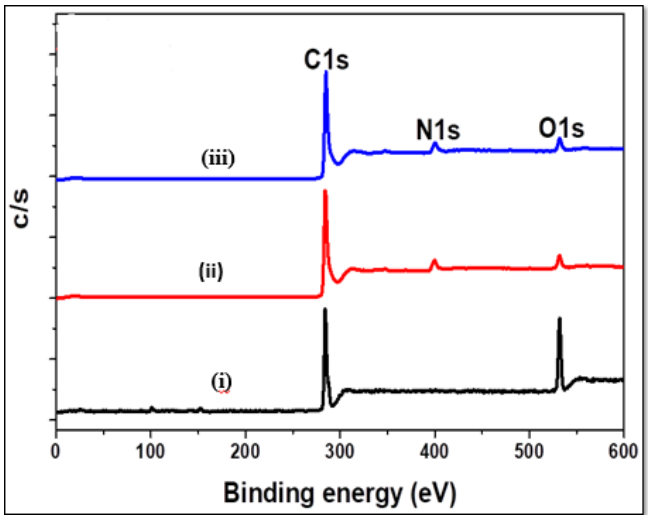

Fig. 3.10: Survey XPS spectrum (i) Pristine bHCSs; (ii) P@N-bHCSs and (iii) A@N-bHCSs.

Table 6: Elemental atomic compositions of the synthesized bHCSs materials

Sample	Elemental Atomic %		
	C1s	N1s	O1s
Pristine bHCSs	97.57	-	2.43
P@N-bHCSs	90.31	5.85	3.84
A@N-bHCSs	90.41	5.73	3.86

Fig. 3.11 shows the C1s and O1s scans on the pristine bHCSs. The peak at 283.8 eV on C1s scan corresponds to the sp^2 hybridized carbon. The other two peaks at 284.8 and 286.9 eV are ascribed to sp^3 C=C and C=O bonding configurations, respectively. The appearance of the main peak at 283.8 eV is attributed to the presence of graphitic carbon, which is in agreement with the Raman analysis, (Fig. 3.8). It was also reported that the presence of graphitic carbon, more likely means that majority carbon atoms are arranged in a conjugated honeycomb lattice[42].

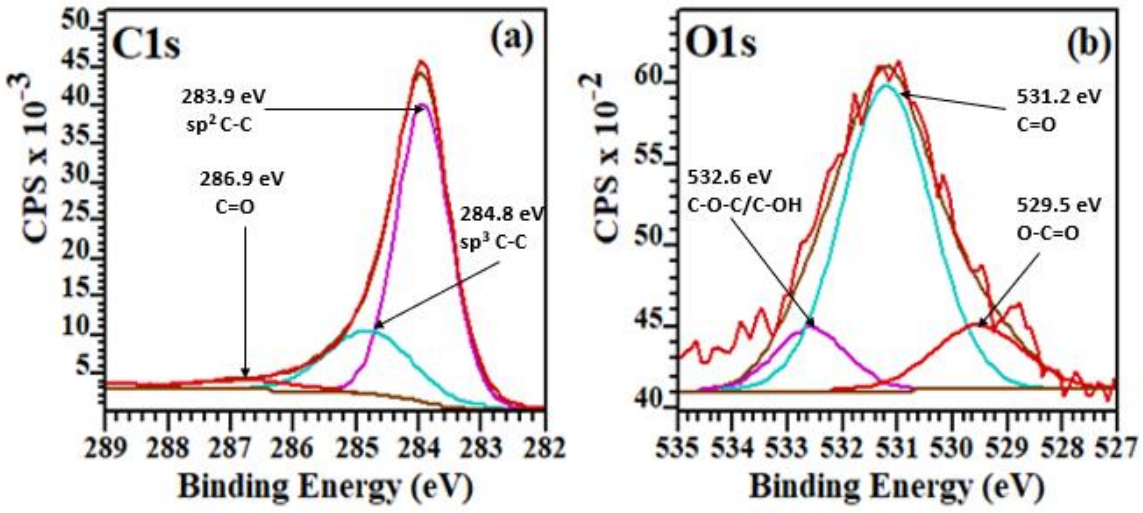

Fig. 11: XPS spectra of deconvoluted (a) C1s peaks and (b) O1s peaks of pristine N-bHCSs.

Both P@N-bHCSs and A@N-bHCSs N1s XPS spectra were deconvoluted, revealing four sub-peaks corresponding to the bonding domains and electronic states of the nitrogen in a carbon framework of the pristine bHCSs, (Fig. 3.12). P@N-bHCSs revealed four N1s peaks at 398.1, 400.6, 402.7 and 405.3 eV corresponding to pyridinic-N, graphitic-N, oxidized-N and elemental N_2, respectively. The chemical structural arrangement of these bonding configurations is illustrated in Fig. 3.13. It was also observed that there was higher concentration on pyridinic N^+-O^- on A@N-bHCSs as compared to P@N-bHCSs, 16% and 13%, respectively. This was ascribed to fewer oxygen atoms bonded to the edge defects of the P@N-bHCSs than in A@N-bHCSs. It was reported that the increased nitrogen content in carbon nanomaterials offers a benefit to the arrangement of defects and enhanced adsorption properties in hydrogen storage technologies[16]. Pyridinic-N was also reported to enhance the catalytic activities of some reactions ascribed to the lone electron pair on the nitrogen atom[12]. The presence of N atoms on graphene framework has also been known to change the local density of states around the Fermi level of the N-doped graphitic carbons, which opens up other properties that are not displayed in pristine carbon and most importantly it tailors the electronic properties which was the main focus of this study[36-37].

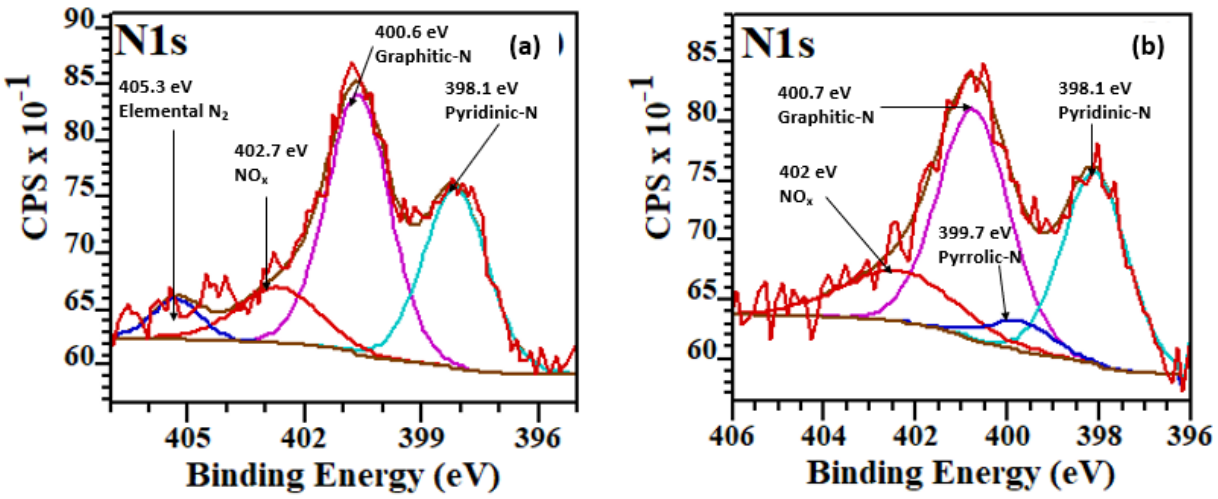

Fig. 3.12: XPS spectra of deconvoluted N1s peaks of (a) P@N-bHCSs and (b) A@N-bHCSs.

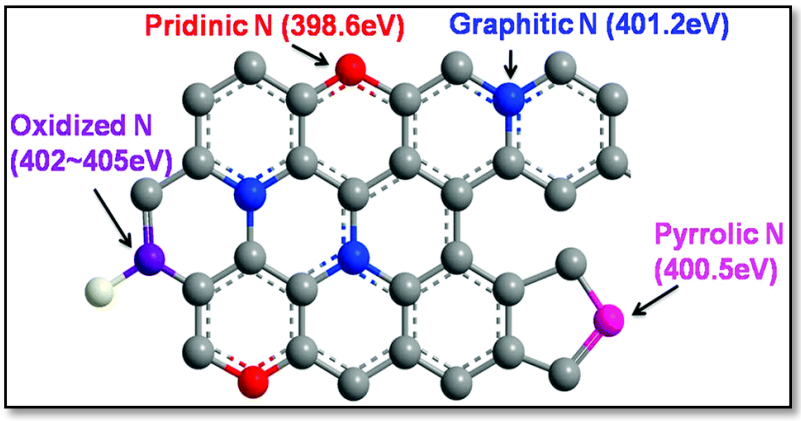

Fig. 3.13: Ball and stick illustration of N-bHCSs bonding domains based on deconvolution of N1s peaks, (Fig. 3.12)[24].

Table 7: Relative concentrations of nitrogen bonding configurations on N-bHCSs

Sample	Concentration of N (%)				
	Pyridinic-N	Pyrrolic-N	Graphitic-N	NOx	Elemental N_2
P@N-bHCSs	33.62	-	47.60	13.19	5.59
A@N-bHCSs	33.95	5.46	44.70	15.89	-

.

Fig. 3.14 shows the deconvoluted C1s and O1s XPS spectra for both P@N-bHCSs and A@N-bHCSs. A@N-bHCSs had higher percentage of sp^2 C-C bonding domains as compared to P@N-bHCSs, (Table 8). This observation was due to the presence of sp^2 bonded graphitic carbon, which explains why the materials showed to have more defects and less thermal decomposition behaviour as shown by the TGA spectrum in Fig. 3.9(c). The concentration of oxygen bonding states on A@N-bHCSs was also higher that P@N-bHCSs as shown in Table 8 and this was ascribed to more oxygen atoms bonded to the edge defects. The results in Table 8 were in an accurate agreement with the results obtained from Raman spectroscopy and TGA, implying that the thermal decomposition temperature of N-bHCSs decreases with increasing oxygen edge defects and also increasing sp^2 C-C dangling bonds.

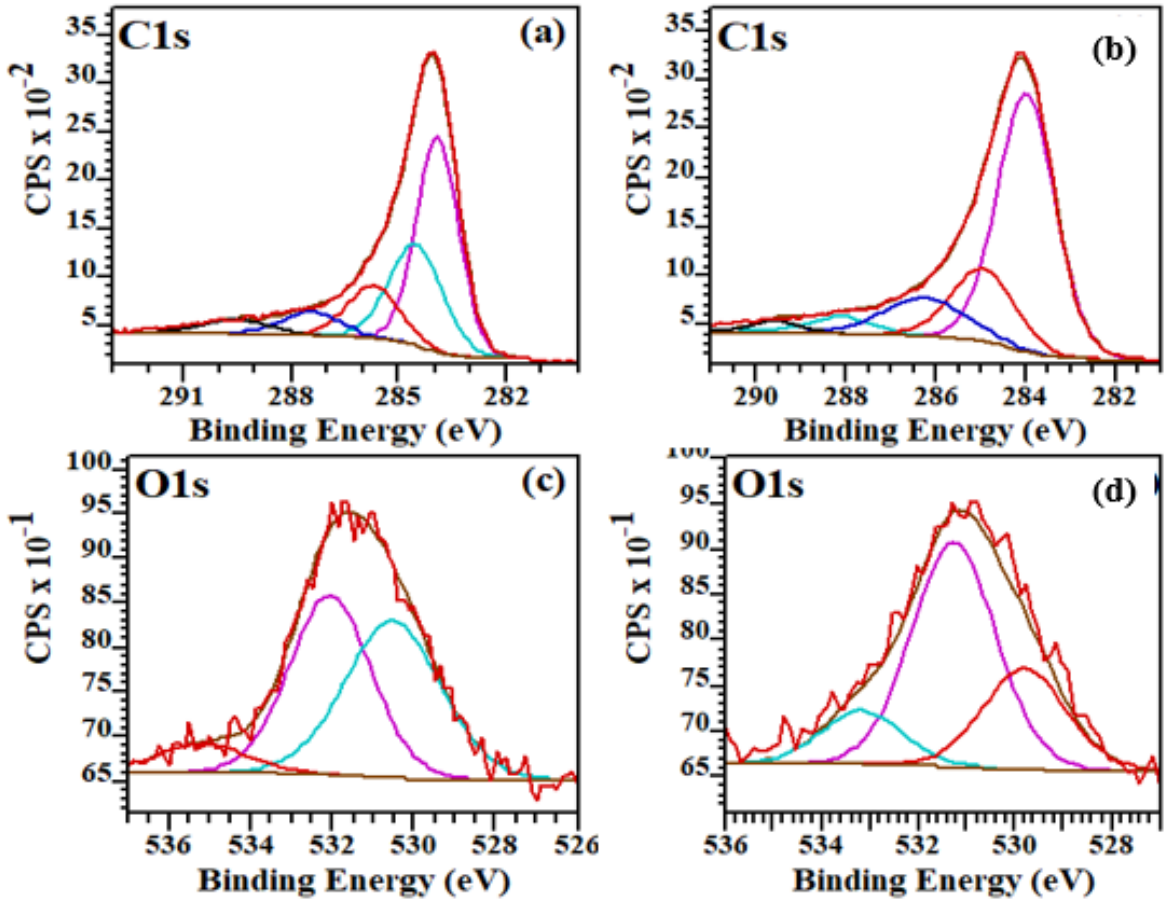

Fig. 3.14: XPS spectra of deconvoluted C1s peaks of (a) P@N-bHCSs and (b) A@N-bHCSs and O1s peaks of (c) P@N-bHCSs and (d) A@N-bHCSs.

Table 8: Relative concentrations of carbon and oxygen bonding configurations/ states on N-bHCSs

Sample	Ave. % Concentration				
	sp^2 C-C	**sp^2 C-N**	**sp^3 C-N/C-C**	**C=O**	**O-C=O**
% [carbon bonding states]					
P@N-bHCSs	46.42	27.71	14.14	7.05	4.67
A@N-bHCSs	61.19	18.92	13.12	4.41	2.36
	% [oxygen bonding states]				
	C=O	**O-C=O**	**C-O-C/C-OH**		
P@N-bHCSs	40.89	48.34	10.77		
A@N-bHCSs	59.39	26.59	14.03		

3.3.5.2 PL analysis

Fig. 3.15 (a-b) shows the PL spectra of the pristine P3HT:PCBM (1:1) blended solution and N-bHCSs doped composites at the same concentrations. The PL spectra of the blends were studied in the wavelength range 525–800 nm, with excitation wavelength of 514.5 nm. The emission spectra for both A@N-bHCSs:P3HT:PCBM and A@T,N-bHCSs:P3HT:PCBM have less intensity as compared to the pyridine based N-bHCSs blends (i.e. P@N-bHCSs:P3HT:PCBM and P@T,N-bHCSs: P3HT:PCBM). This implies that more charge dissociation is taking place for A@N-bHCSs:P3HT:PCBM and A@T,N-bHCSs:P3HT:PCBM[53,54].

Quenching of intensity indicates that there is more efficient transfer of charge and lesser recombination taking place[40,45]. The main peak was observed at 636 nm for all the blends/ samples, (Fig 3.15 (a-b)). The observed enhancement in the intensity of the N-bHCSs doped P3HT:PCBM blends is suggested to be due to a more efficient electron transport introduced by N-doping of the bHCSs. It has been previously reported that in a pristine-P3HT-PCBM blend, the photogenerated excitons are dissociated at the interfaces, and the electrons are transported to the Al by passing between the C61 fullerenes [46]. It was found that the interface between donor and acceptor should be large to enhance a a good charge carrier generation[55]. The assimilation of the N-bHCSs in the photoactive layer provides additional pathways for the electrons through the dispersed N-bHCSs complex. This suppresses charge recombination and enhances electron transport[46], which supports the observation that the peak intensities of both P@N-bHCSs:P3HT:PCBM and P@T,N-bHCSs:P3HT:PCBM and also A@N-bHCSs:P3HT:PCBM blends were higher than that of the P3HT:PCBM blend. There was also some photo bleaching occurring in A@T,N-

bHCSs:P3HT:PCBM blends, which explains why the peak intensity led the lower values amongst the other blends.

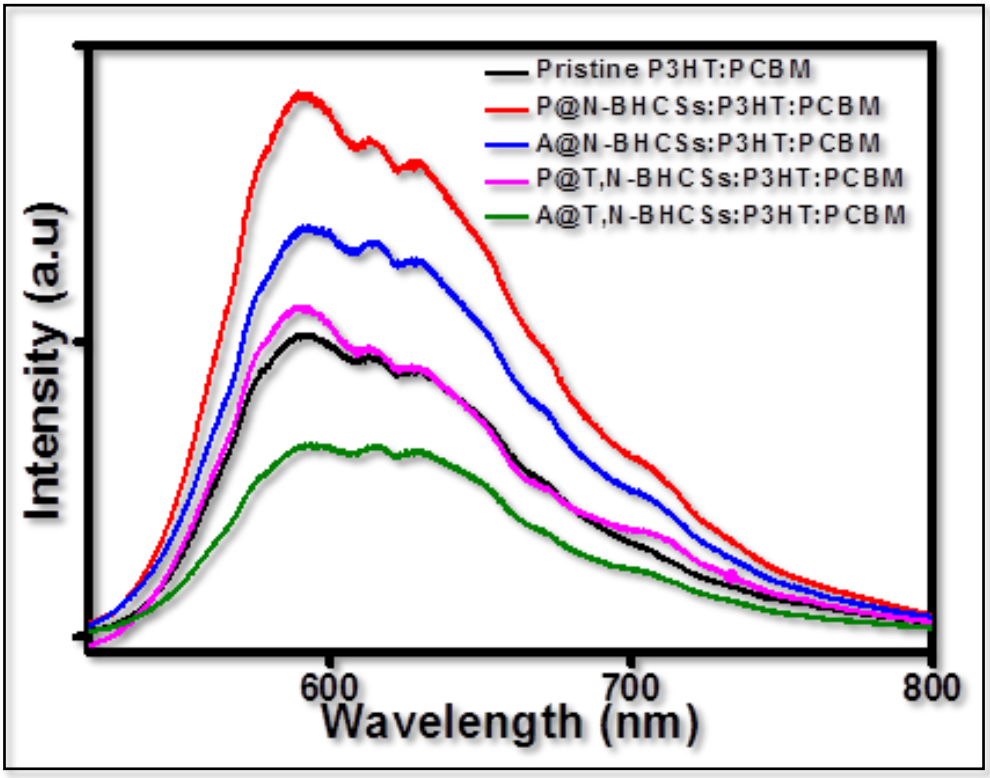

Fig. 3.15: Photoluminescence spectra of prepared pristine P3HT:PBCM and N-bHCSs doped P3HT:PBCM blends; Black = pristine P3HT:PCBM blend; Red and Blue = *in-situ* doped N-bHCSs:P3HT:PCBM blends; Pink and Green = *ex-situ* doped N-bHCSs:P3HT:PCBM blends. Note: for specificity of the materials, please see legend in the figure above.

3.3.5.3 AFM analysis

The morphology of the of pristine P3HT:PCBM and N-bHCSs:P3HT:PCBM blends was studied using AFM, (Fig. 3.16). An increased surface roughness is seen on films with N-bHCSs as compared to pristine P3HT:PCBM. These results are in line with the PL findings, which revealed that an increased roughness facilitates the charge transfer to N-bHCSs:P3HT:PCBM junction, which is attributed to the increase in PL peak intensity, hence in this case P@N-bHCSs had more charge transfer as compared to A@N-bHCSs. There was more oxygen atoms bonded to the edge defects of the A@N-bHCSs as revealed by XPS data in Table 7, which explains the reduced electron transfer activity on these materials as compared to P@N-bHCSs.

Similar studies by Mutuma and co-workers was done where it was shown that the increase in surface roughness, brings closer the interfacial interactions between the active layer, anode and the hole transport layer[40]. The calculated root mean square (R.M.S) of the pristine P3HT:PCBM film was 0.536 nm where as for P@N-bHCSs and A@N-bHCSs blends was 0.865 and 1.302 nm, respectively as shown in Table 9.

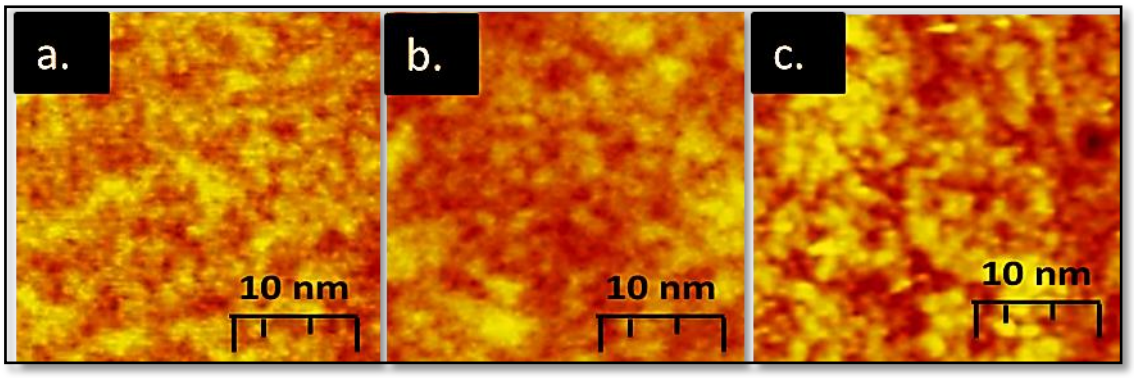

Fig.3. 16: AFM images of the prepared thin films (a) pristine P3HT:PCBM; (b) A@N-bHCSs:P3HT:PCBM; (c) P@N-bHCSs:P3HT:PCBM.

Table 9: Calculated R.M.S roughness of pristine P3HT:PCBM and N-bHCSs doped thin films

Sample	**P3HT:PCBM**	**A@N-bHCSs:P3HT:PCBM**	**P@N-bHCSs:P3HT:PCBM.**
R.M.S roughness (nm)	0.536	0.865	1.302

3.3.5.4 Current-voltage (*J-V*) characteristics of the fabricated devices

Table 10 and Fig. 3.17 show the current-voltage characteristics of the P3HT:PCBM blends doped with pristine N-bHCSs, P@N-bHCSs and A@N-bHCSs active layers under illumination at intensity of F = 6. The current densities (J_{sc}) of the devices with N-bHCSs were slightly higher than that on pristine bHCSs. This can be attributed to fact that N-bHCSs has an increased charge-transport distance as demonstrated by the PL results in Fig. 3.15 and also increased surface roughness as shown in Fig. 3.16. The results have proved that the electron density was increased by n-type doping of bHCSs, which consequently improved the optoelectronic properties of P3HT:PCBM active layer in an organic solar cell device as hypothesized. The alteration of the HOMO and LUMO energies of the active layer components was also predicted by the increase in open circuit voltage (V_{oc}) in the devices with N-bHCSs, which is also consisted with the literature findings[58,59].

The V_{oc} and J_{sc} values of both P@N-bHCSs and A@N-bHCSs were much lower than those reported in the literature by Mutuma *et.al* for pristine bHCSs, this could be attributed to the size distribution of the SiO_2 spheres (d = 105 - 200 $\pm$ 5 nm) used to make bHCSs, which was slightly higher than that in the literature (d = 90 - 300 nm)[48]. The size distribution resulted in shorting of the device. Although the values are much lower, we also took into consideration that gold (Au) was also incorporated into the broken carbon spheres (bCSs) in the literature[33], hence the comparison is not a full reflection of the materials, what is important is the enhancement of the device performance by n-doping which gives directions to future studies. Power conversion efficiency values were not mandatory for this study since the FF was very low due to large series resistance (R_s) by prediction from the shape of the curves in devices; the point was to demonstrate the improvement of the device performance by n-doping of the bHCSs. Fig.3.18, shows the semi-log I-V characteristics corresponding to the curves in Fig. 3.18, under dark current and illumination. The curves show the exact points when the V_{oc} and the J_{sc} can be found.

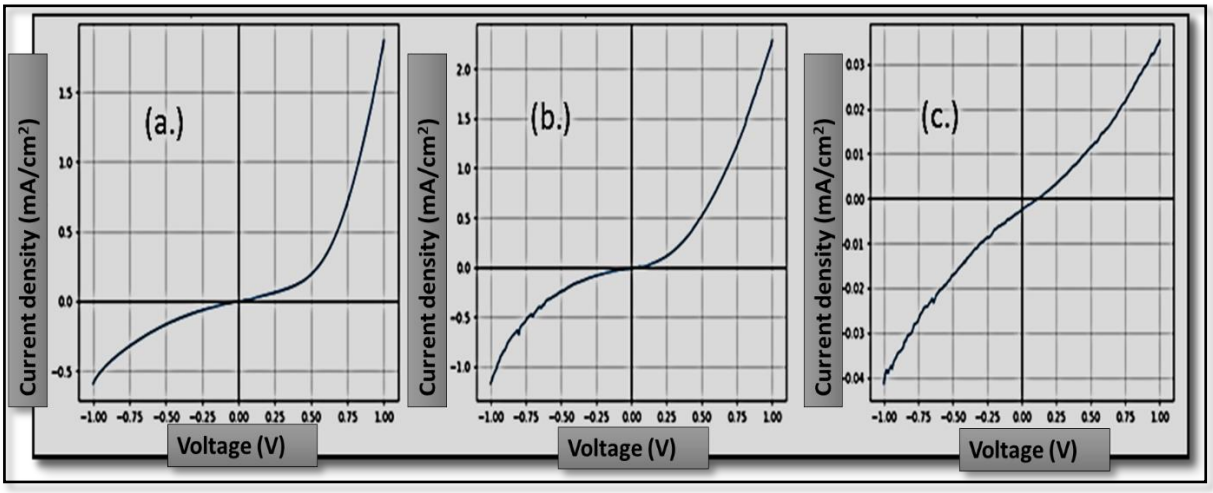

Fig. 3.17: I-V curve analysis of P3HT: PCBM blends doped withg (a) pristine N-bHCSs; (b) A@N-bHCSs; (c) P@N-bHCSs (measured at AM 1.5 / 100 mW/cm^2 illumination, curves plotted using I-V plot - solar characterisation software, version 0.5.3, 2017).

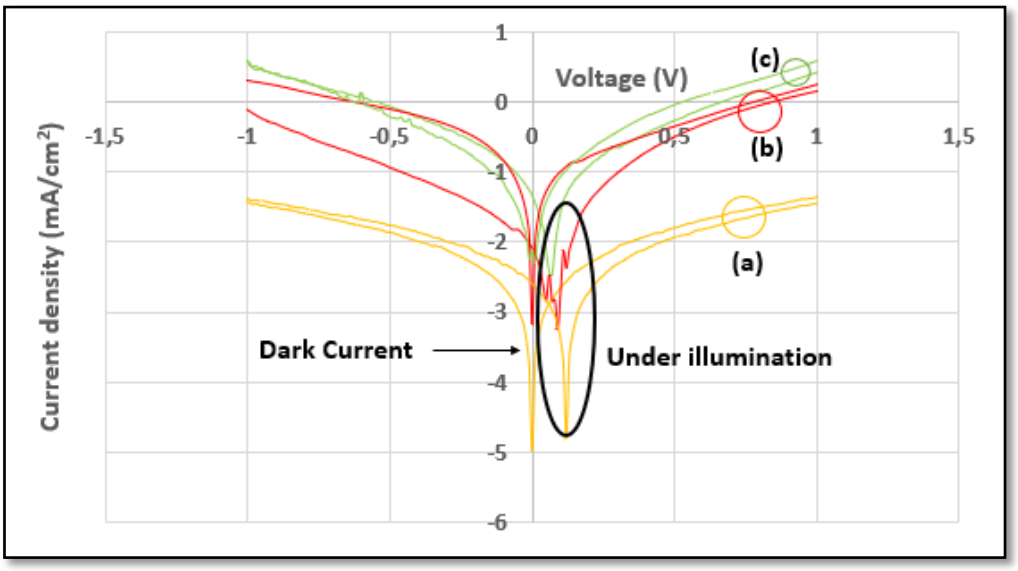

Fig. 3.18: Semi-log I-V charecteristics of the fabricated P3HT:PCBM based devices doped with (a) P@N-bHCSs; (b) A@N-bHCSs and (c) Pristine bHCSs. Measurements were done under both dark and illumination conditions as indicated in the plots.

Table 10: Device parameters of solar cells prepared by bHCSs doped P3HT: PCBM composites in ITO/PEDOT:PSS/P3HT:PCBM:bHCSs/Al under AM 1.5 / 100 mW/cm^2 illumination and cross-sectional area of 7.0×10^{-4} cm^2

P3HT:PCBM blends based device	I (µA)	V_{oc} (V)	Jsc (µA/cm^2)
Pristine bHCSs	0.001	0.09	1.43
A@N-bHCSs	0.002	0.18	2.56
P@N-bHCSs	0.15	0.20	214.29

The power conversion efficiencies (η) of the fabricated devices could be calculated using Eq. 1

$$\eta = J_{sc}V_{oc}FF/P_{in} \quad \textbf{Eq. 1}$$

where P_{in} is the incident power and has irradiance value of 100 mW/m^2 which is standard for measuring the PCE of solar cells[60].

3.5 References

1. Deshmukh, A. A., Mhlanga, S. D. & Coville, N. J. Carbon spheres. *Mater. Sci. Eng. R Reports* **70,** 1–28 (2010).

2. Chung, I., Lee, B., He, J., Chang, R. P. H. & Kanatzidis, M. G. All-solid-state dye-sensitized solar cells with high efficiency. *Nature* **485,** 486–489 (2012).

3. Gao, M.-Y. *et al.* Fullerene-like Polyoxotitanium Cage with High Solution Stability. *J. Am. Chem. Soc.* **138,** 2556–2559 (2016).

4. Mohammad Bagher, A. Comparison of Organic Solar Cells and Inorganic Solar Cells. *Int. J. Renew. Sustain. Energy* **3,** 53 (2014).

5. Tang, S., Tang, Y., Vongehr, S., Zhao, X. & Meng, X. Nanoporous carbon spheres and their application in dispersing silver nanoparticles. *Appl. Surf. Sci.* **255,** 6011–6016 (2009).

6. Cao, B. *et al.* Preparation of Nitrogen-Doped Carbon Spheres by Injecting Pyrolysis of Pyridine. *ACS Sustain. Chem. Eng.* **3,** 1786–1793 (2015).

7. Guldi, D. M., Rahman, G. M. A., Zerbetto, F. & Prato, M. Carbon Nanotubes in Electron Donor−Acceptor Nanocomposites. *Acc. Chem. Res.* **38,** 871–878 (2005).

8. K. L. Choy. Chemical vapour deposition of coatings. *Prog. Mater. Sci.* **48,** 57–170 (2003).

9. Carlsson, J.-O. & Jansson, U. Progress in chemical vapor deposition. *Prog. Solid State Chem.* **22,** 237–292 (1993).

10. Wang, Z. L. & Kang, Z. C. Graphitic structure and surface chemical activity of nanosize carbon spheres. *Carbon.* **35,** 419–426 (1997).

11. Zhang, J. *et al.* Carbon science in 2016: Status, challenges and perspectives. *Carbon N. Y.* **98,** 708–732 (2016).

12. Chen, J. Recent Progress in Advanced Materials for Lithium Ion Batteries. *Materials.* **6,** 156–183 (2013).

13. Liao, Y., Gao, L., Zhang, X. & Chen, J. Nitrogen-doped hollow carbon spheres with enhanced electrochemical capacitive properties. *Mater. Res. Bull.* **47,** 1625–1629 (2012).

14. Hulicova-Jurcakova, D. *et al.* Highly Stable Performance of Supercapacitors from

Phosphorus-Enriched Carbons. *J. Am. Chem. Soc.* **131,** 5026–5027 (2009).

15. Lu, Y.-F. Nitrogen-Doped Graphene Sheets Grown by Chemical Vapor Deposition: Synthesis and Influence of Nitrogen Impurities on Carrier Transport. *Nature*. **77**, 456-458 (2013).

16. Galeano, C. Nitrogen-Doped Hollow Carbon Spheres as a Support for Platinum-Based Electrocatalysts. *ACS Catal.* **4,** 3856–3868 (2014).

17. Zheng, Y., Jiao, Y., Jaroniec, M., Jin, Y. & Qiao, S. Z. Nanostructured Metal-Free Electrochemical Catalysts for Highly Efficient Oxygen Reduction. *Small* **8,** 3550–3566 (2012).

18. Liang, J., Jiao, Y., Jaroniec, M. & Qiao, S. Z. Sulfur and Nitrogen Dual-Doped Mesoporous Graphene Electrocatalyst for Oxygen Reduction with Synergistically Enhanced Performance. *Angew. Chemie Int. Ed.* **51,** 11496–11500 (2012).

19. Xu, B., Hou, S., Cao, G., Wu, F. & Yang, Y. Sustainable nitrogen-doped porous carbon with high surface areas prepared from gelatin for supercapacitors. *J. Mater. Chem.* **22,** 19088 (2012).

20. Jiao, Y., Zheng, Y., Jaroniec, M. & Qiao, S. Z. Origin of the Electrocatalytic Oxygen Reduction Activity of Graphene-Based Catalysts: A Roadmap to Achieve the Best Performance. *J. Am. Chem. Soc.* **136,** 4394–4403 (2014).

21. Ling, X. Can Graphene be used as a Substrate for Raman Enhancement? *Nano Lett.* **10,** 553–561 (2010).

22. Wei, D. Synthesis of N-Doped Graphene by Chemical Vapor Deposition and Its Electrical Properties. *Nature*. **200,** 17-20 (2009).

23. Jin, Z., Yao, J., Kittrell, C. & Tour, J. M. Large-Scale Growth and Characterizations of Nitrogen-Doped Monolayer Graphene Sheets. *ACS Nano* **5,** 4112–4117 (2011).

24. Dai, J., Yuan, J. & Giannozzi, P. Gas adsorption on graphene doped with B, N, Al, and S: A theoretical study. *Appl. Phys. Lett.* **95,** 232105 (2009).

25. Jeong, H. M. Nitrogen-Doped Graphene for High-Performance Ultracapacitors and the Importance of Nitrogen-Doped Sites at Basal Planes. *Nano Lett.* **11,** 2472–2477 (2011).

26. Reddy, A. L. M. Synthesis Of Nitrogen-Doped Graphene Films For Lithium Battery Application. *ACS Nano* **4,** 6337–6342 (2010).

27. Chen, H. Nitrogen Doping Effects on the Physical and Chemical Properties of Mesoporous Carbons. *J. Phys. Chem. C* **117,** 8318–8328 (2013).

28. Bogush, G. H., Tracy, M. A. & Zukoski IV, C. F. Preparation of monodisperse silica particles: Control of size and mass fraction. *J. Non. Cryst. Solids* **104,** 95–106 (1988).

29. Principles, S. C., Chen, Y. U., Chen, H. & Shi, J. Construction of Homogenous / Heterogeneous Hollow Mesoporous Silica Nanostructures by. *Acc. Chem. Res.* **47,** 125–137 (2014).

30. Stöber, W., Fink, A. & Bohn, E. Controlled growth of monodisperse silica spheres in the micron size range. *J. Colloid Interface Sci.* **26,** 62–69 (1968).

31. Yang, T. *et al.* N-doped mesoporous carbon spheres as the oxygen reduction reaction catalysts. *J. Mater. Chem. A* **2,** 18139–18146 (2014).

32. Sun, Z., Song, X., Zhang, P. & Gao, L. Template-assisted synthesis of multi-shelled carbon hollow spheres with an ultralarge pore volume as anode materials in Li-ion batteries. *RSC Adv.* **5,** 3657–3664 (2015).

33. Mutuma, B. K., Matsoso, B., Ranganathan, K., Wamwangi, D. & Coville, N. J. Generation of open-ended, worm-like and graphene-like structures from layered spherical carbon materials. *RSC Adv.* **6,** 20399–20408 (2016).

34. Li, M., Wu, Q., Wen, M. & Shi, J. A novel route for preparation of hollow carbon nanospheres without introducing template. *Nanoscale Res. Lett.* **4,** 1365–1370 (2009).

35. Yang, D.-S., Bhattacharjya, D., Inamdar, S., Park, J. & Yu, J.-S. Phosphorus-Doped Ordered Mesoporous Carbons with Different Lengths as Efficient Metal-Free Electrocatalysts for Oxygen Reduction Reaction in Alkaline Media. *J. Am. Chem. Soc.* **134,** 16127–16130 (2012).

36. Masalov, V. M., Sukhinina, N. S., Kudrenko, E.& Emelchenko, G. Mechanism of formation and nanostructure of Stöber silica particles. *Nanotechnology* **22,** 275718 (2011).

37. Ibrahim, I. M., Zikry, F. & Sharaf, M. Preparation of spherical silica nanoparticles: Stober

silica. *J. Am. Sci.* **6,** 985–989 (2010).

38. Yan, L. P3HT/Dodecylamine Functioned Carbon Microspheres Composite Films for Polymer Solar Cells. *Fullerenes, Nanotub. Carbon Nanostructures*. **23,** 549–556 (2015).

39. Wilgosz, K. Template method synthesis of mesoporous carbon spheres and its applications as supercapacitors. *Nanoscale Res. Lett.* **7,** 269 (2012).

40. Singh, V., Arora, S., Arora, M., Sharma, V. & Tandon, R. P. Optimizing P3HT/PCBM/MWCNT films for increased stability in polymer bulk heterojunction solar cells. *Phys. Lett. Sect. A Gen. At. Solid State Phys.* **378,** 3046–3054 (2014).

41. Kim, H.-S. Lead iodide perovskite sensitized all-solid-state submicron thin film mesoscopic solar cell with efficiency exceeding 9%. *Sci. Rep.* **2,** 591 (2012).

42. Liu, Y., Yang, Y. M., You, J., Li, G. & Yang, Y. Integrated Perovskite/Bulk-Heterojunction toward E ffi cient Solar Cells. *Nano Lett.* (2014).

43. Winans, R. E. & Carrado, K. A. Novel forms of carbon as potential anodes for lithium batteries. *J. Power Sources* **54,** 11–15 (1995).

44. Garner, L. E. Promoting Morphology with a Favorable Density of States Using Diiodooctane to Improve Organic Photovoltaic Device Efficiency and Charge Carrier Lifetimes. *ACS Energy Lett.* **2,** 1556–1563 (2017).

45. Bhatia, R. & Kumar, L. Functionalized carbon nanotube doping of P3HT:PCBM photovoltaic devices for enhancing short circuit current and efficiency. *J. Saudi Chem. Soc.* **21,** 366–376 (2017).

46. Kymakis, E., Kornilios, N. & Koudoumas, E. Carbon nanotube doping of P3HT : PCBM photovoltaic devices. *J. Phys. D. Appl. Phys.* **41,** 165110 (2008).

47. Bernardi, M., Giulianini, M. & Grossman, J. C. Self-assembly and its impact on interfacial charge transfer in carbon nanotube/P3HT solar cells. *ACS Nano* **4,** 6599–6606 (2010).

48. Mutuma, B. Generation of open ended , worm like and graphene like structures from layered spherical carbon materials. *RSC Adv.* **6,** 20399–20408 (2016).

49. Jones, A. C. & Hitchman, M. L. Chemical Vapour Deposition. Chemical Vapour Deposition: Precursors, Processes and Applications, *RSC Adv*. **10**, 20-25 (2008).

50. Deng, Y., Xie, Y., Zou, K. & Ji, X. Review on recent advances in nitrogen-doped carbons: preparations and applications in supercapacitors. *J. Mater. Chem. A* **4,** 1144–1173 (2015).

51. Masalov, V. M., Sukhinina, N. S., Kudrenko, E. A. & Emelchenko, G. A. Mechanism of formation and nanostructure of Stöber silica particles. *Nanotechnology* **22,** 275718 (2011).

52. Jia, R. Synthesis of highly nitrogen-doped hollow carbon nanoparticles and their excellent electrocatalytic properties in dye-sensitized solar cells. *Science*. **44,** 10829–10834 (2010).

53. Servaites, J. D., Ratner, M. A. & Marks, T. J. Organic solar cells: A new look at traditional models. *Energy Environ. Sci.* **4,** 4410–4422 (2011).

54. Zhang, X. Employing Easily Prepared Carbon Nanoparticles to Improve Performance of Inverted Organic Solar Cells. *ACS Sustain. Chem. Eng.* **4,** 2359–2365 (2016).

55. Marinova, N. Light Harvesting and Charge Recombination in CH 3 NH 3 PbI 3 Perovskite Solar Cells Studied by Hole Transport Layer Thickness Variation. *ACS Nano*. **9,** 4200–4209 (2015).

56. Shrotriya, V., Ouyang, J., Tseng, R. J., Li, G. & Yang, Y. Absorption spectra modification in poly(3-hexylthiophene):methanofullerene blend thin films. *Chem. Phys. Lett.* **411,** 138–143 (2005).

57. Chi, W. J., Li, Q. S. & Li, Z. S. Effects of molecular configuration on charge diffusion kinetics within hole-transporting materials for perovskites solar cells. *J. Phys. Chem. C* **119,** 8284–8590 (2015).

58. Schiros, T. Study of the electronic properties of Li-intercalated nitrogen doped graphite. *ACS Nano* **4,** 4025–4031 (2010).

59. Kuang, C. Highly Efficient Electron Transport Obtained by Doping PCBM with Graphdiyne in Planar-Heterojunction Perovskite Solar Cells. *Nano Lett.* **15,** 2756–2762 (2015).

60. Gustav, T.D. Organic-inorganic hybrid perovskites as light absorbing material in solar cells. *Science*. **22,** 1–30 (2013).

Chapter 4

Investigation of $CH_3NH_3PbI_3$ photovoltaic device performance and stability

4.1 Introduction

One of the promising avenues in the photovoltaic (PV) industry is the synthesis and use of organic-inorganic hybrid perovskite-based devices that have recently reached power conversion efficiency (PCEs) values of up to 20.1% which transcends the best values for dye sensitized, quantum dots, organic and amorphous silicon solar cells and other evolving PV technologies[1]. These materials exhibit very fascinating features, such as exclusive optical and exciton properties, as well as good electrical conductivity[2–4]. The inorganic-organic hybrid perovskite materials are part of the ABX_3 perovskite crystal unit cell family where B is a divalent metal cation and can be Ge^{2+}, Pb^{2+} or Sn^{2+} in a 6-fold coordination forming an octahedron $[BX_6]^{4-}$ with X a monovalent anion, typically a halide, (Fig. 4.1)[5,3]. The A cation is there to balance the negative charge, stabilizing the octahedron. It can be a small molecule such as the methyl-ammonium ion[6]. The halide anion and the divalent metal cation can be varied, and these changes are often used to tune the optoelectronic properties (i.e. optical gap)[3,7].The tolerance factor *t* (i.e. ratio of the separation of A and X to the separation of B and X, *Goldschmidt's tolerance factor*) and octahedral factor μ (ratio of the B and X ionic radii) are used determine whether a combination of A, B and X can form a stable perovskite crystal structure[8]. The ideal cubic perovskite crystal has t = 1 while t|<|1 yields octahedral distortion[9]. The iodide and bromide methylammonium trihalogenoplumbates (II) ($CH_3NH_3PbX_3$, $MAPbI_3$) candidates have showed breakthrough PCE performance values for thin film solar cells[10].

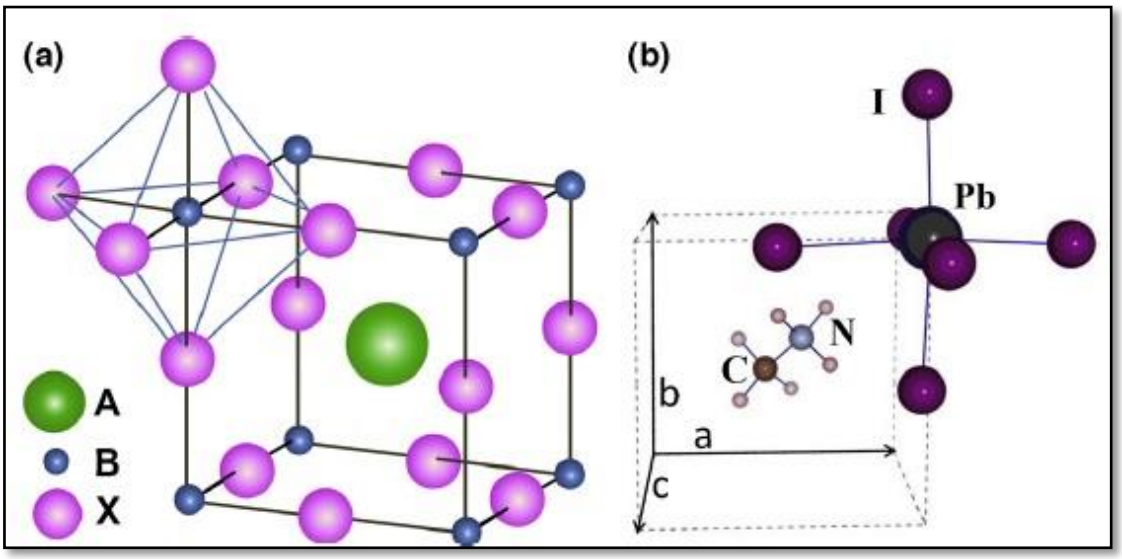

Fig. 4.1: (a) ABX_3 perovskite structure showing BX_6 octahedral with the larger A cation occupying a cubo-octahedral site (b) Unit cell of a cubic $CH_3NH_3PbI_3$ perovskite[11].

The first perovskite solar cell device was made in 2006 and was in a liquid state. In 2012 the first solid state perovskite device was made incorporating an organic hole transport material (HTM), 2,2',7,7'-tetrakis(N,N-dimethoxyphenylamine)-9,9'-spirobifluorene (spiro-MeOTAD)[12,13], (Fig. 4.2).

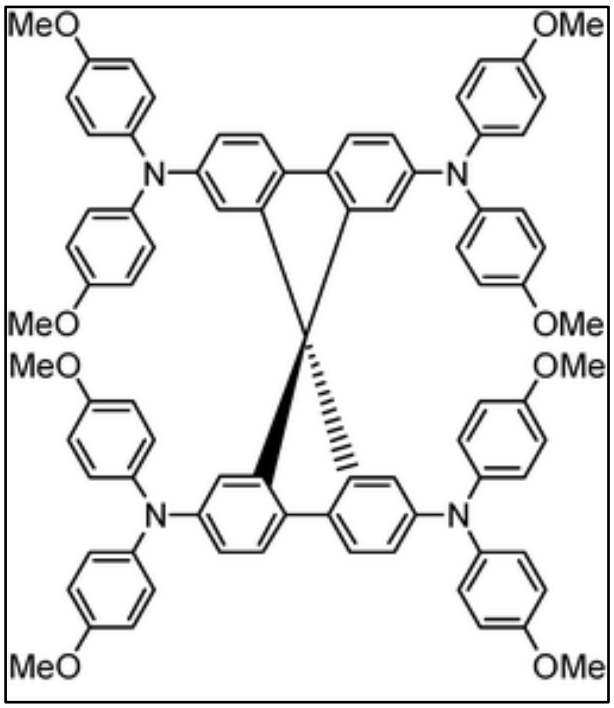

Fig. 4.2: Chemical structure of Spiro-MeOTAD[14].

Fig. 4.3, Illustrates an example of a bulk heterojunction polymer solar cells (BHJ PSCs), containing a perovskite as a photoactive layer. As indicated in the structure, ITO is a transparent conductive substrate that is commonly used in BHJ organic solar cells. It can be substituted by fluorine-doped tinoxide (FTO)[15].

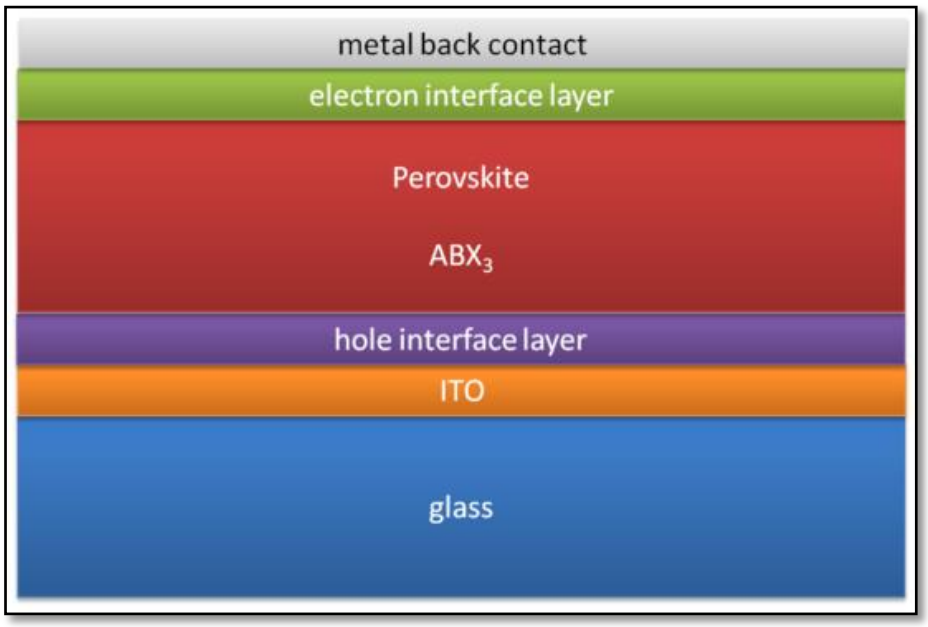

Fig. 4.3: Generic structure of the perovskite solar cell[16].

The metal oxide layer (i.e. ITO/ FTO) is usually covered by a thin layer, such as Poly(3,4-ethylenedioxythiophene)-poly(styrene sulfonate) (PEDOT:PSS), shown in Fig. 4.4, over which the photo active layer is deposited[5].

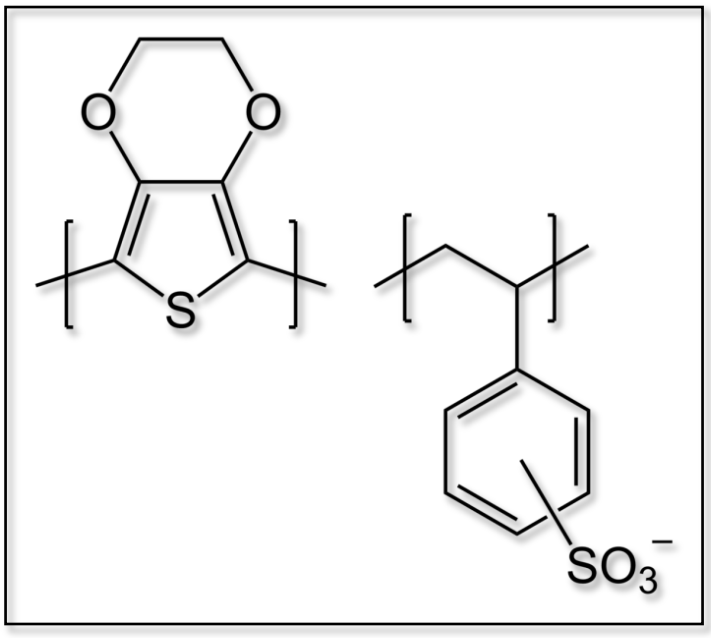

Fig. 4.4: Chemical structure of PEDOT:PSS[5].

The photoactive layer is then covered by a thin layer of an electron interface layer, such as PCBM, which is finally coated with a thin metal/ back contact such as, usually by thermal evaporation[17]. Al is regularly used because of its low work function[18,19,1,20]. However, Al also has some drawbacks such as oxidation problems when exposed to air and degradation by the acidity of PEDOT:PSS[21]. Many researches have circumvented this problem by reversing the charge collection process (i.e. collecting the holes on the top metal back contact layer and electrons at the bottom electrode) and this is done by substituting Al with metals such as Ag and Au with a high work function [1]. The bottom layer should also be an electron conducting layer such as zinc oxide (ZnO) or titanium oxides (TiO_x), eliminating the problem of the acidic effect of PEDOT: PSS on ITO of FTO[15].

The fact that perovskites relaxes the quality requirement (crystallinity) which is mandatory when dealing with silicon-based solar cells, makes it a very useful material to use in solar cell devices[22]. On the other hand, perovskites also have their drawbacks, which include their sensitivity to moisture (and possibly air) and their relatively poor stability is the largest barrier towards their commercialization [23]. The three main factors that need to be addressed in order to achieve a high stability of perovskite solar cells include air (H_2O and O_2) stability, photo stability/ UV radiation and thermal stability[24–26].

4.1.1 Stability in Air: H_2O and O_2 studies

When aqueous methylammonium lead (II) iodide is exposed to humid conditions, a hydrolysis reaction occurs in the presence of H_2O, where methylammonium lead (II) iodide first degrades into aqueous lead iodide and methylammonium iodide as presented in Fig. 4.5. Aqueous methylammonium iodide further decomposes into an aqueous methylammonium cation and hydrogen iodide. Hydrogen iodide then reacts with oxygen to form an iodide (II) ions and water or decomposes into hydrogen gas and iodide (II) ions. The consumption of hydrogen iodide steers the entire decomposition process which in turn causes decrease in the PCE.

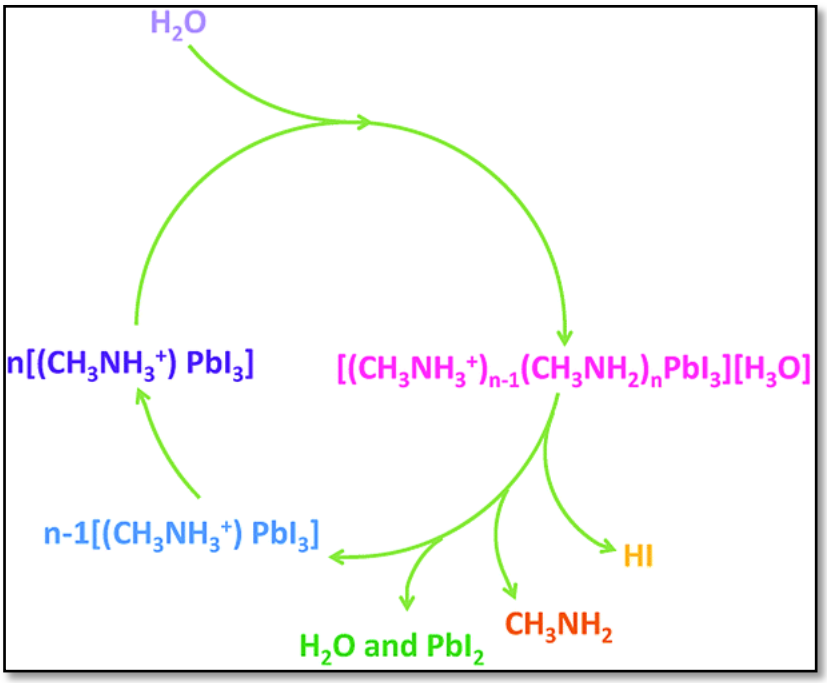

Fig. 4.5: Schematic illustration of the degradation lifecycle of $CH_3NH_3PbI_3$ crystals against moisture[27].

4.1.2 Thermal stability

Thermal degradation is another major issue faced in the use of inorganic-organic hybrid perovskite solar cells since it is difficult to avoid temperature increase during operation[25]. The crystal structure of the halide perovskite is indeed sensitive to temperature changes as there are two coexisting orthorhombic phases at room temperature which are formed from the rotation and distortions of the perovskite cage[28]. The phase related structural transitions determine the performance and the stability of the device[29]. Overall, there are two kinds of thermal degradation in a PV device; the

intrinsic thermal instability of the perovskite material itself which occurs at 85 ℃ even in inert conditions and the instability of the device layers such as the hole transport material (HTM)[30].

4.1.3 Photo stability/ UV radiation

Fig. 6 shows the mechanism of degradation enhanced by UV-light. When the device is exposed to UV light, an electron-hole pair (exciton) is formed in TiO_2 as a consequence of the inter-band transition. The hole in the valence band recombines with the electron by desorbing O_2 at the O_2 adsorption site. The photo generated electrons are then distributed differently, where the electrons generated in light absorbers are injected into the conduction band of the TiO_2 and the free electrons left in the TiO_2 recombine with the hole generated from spiro-MeOTAD.

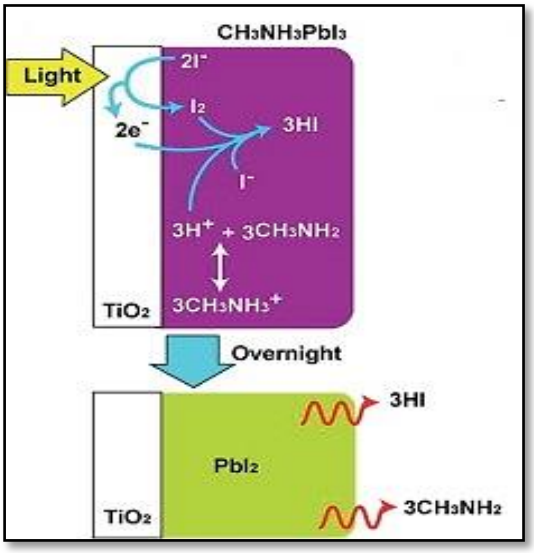

Fig. 4.6: Degradation of the perovskite crystals against UV-light[17].

The techniques to overcome these stability problems are currently under investigation worldwide. Some attempts have been done to make $CH_3NH_3PbI_3$, using an equimolar mixture of methyl ammonium iodide (CH_3NH_3I) and lead iodide (PbI_3) by applying drop-casting and annealing techniques[6]. Some recent studies have shown that the stability of the $CH_3NH_3PbBr_3$ perovskite can be improved by storage in N_2 for about two weeks, which suppresses any changes in morphology and crystallinity[31].

One of the requirements in obtaining good operating perovskite devices is by achieving a high quality perovskite film during fabrication[32]. To obtain highly crystalline films, thermal annealing is

also required, but it often leads to inhomogeneous nucleation of the perovskite films and degrades the performance of their corresponding solar cell devices. A similar study was done by others, where the effect of annealing of perovskite films at room temperature using various solvents was evaluated and the results showed high levels of crystallinity[29,33,34].

In this study we demonstrate the effect of exposing the $CH_3NH_3PbI_3$ thin film to air in duration of 24 h. The main aim was to deliberately expose the $CH_3NH_3PbI_3$ thin film to air in order to track the time it takes to degrades the crystals completely, study the morphology of these crystals and finally look how this degradation alters the photovoltaic properties of these materials.

4.2 Experimental

4.2.1 The effect of air exposure time on $CH_3NH_3PbI_3$

4.2.1.1 Preparation of CH_3NH_3I

A concentrated aqueous solution of HI (15 mL, 57 wt. % in water) was reacted with methylamine (CH_3NH_2) (15 mL, 40 wt. % in aqueous solution) at 0℃ for 2 h with constant stirring under nitrogen gas. The resulting CH_3NH_3I was then crystallized by removing the solvent by a rotary evaporator at 70℃. The resulting crystals were then washed with diethyl ether three times and dried under vacuum, overnight. This was stored in a desiccator until needed.

4.2.1.2 Cleaning and preparation of ITO-glass substrate

The ITO-glass substrate was first etched with ZnO slurry and 10M HCl. The substrate was then washed with soap water while rubbing the surfaces to remove any adhering materials and then rinsed with dH_2O. The substrate was then a sonicated in dH_2O for 15 min, rinsed with dH_2O, sonicated in acetone for 15 min, rinse with dH_2O, sonicated in EtOH for 15 min, add small portion of dH_2O and sonicate for further 5 min then take out the substrate. It was then dried under stream of N_2 air. The procedure for substrate cleaning is illustrated in chapter 3, (Fig.4.5).

4.2.1.3 Stepwise spin coating: ITO/PEDOT: PSS/$CH_3NH_3PbI_3$/PC_6BM/Al device fabrication

After cleaning the etched substrates the water soluble PEDOT:PSS was spin coated onto the substrate at 2500 rpm for 1 min. Annealing was subsequently carried out at 80 ℃ for 5 min to remove adsorbed water on the film. Thereafter a mixed solution of the halide perovskite dissolved in dichloromethane (DCM) solvent was spin coated onto the PEDOT:PSS surface for 1 min at 2500 rpm. The spin coating of the electron transport layer (PCBM) was subsequently carried out onto the

photoactive layer at 2500 rpm for 1 min. The metallization of the top electrode of the hybrid device was achieved by thermal evaporation in vacuum of Al layer. Schematic illustration of device fabrication is shown in Fig. 4.7.

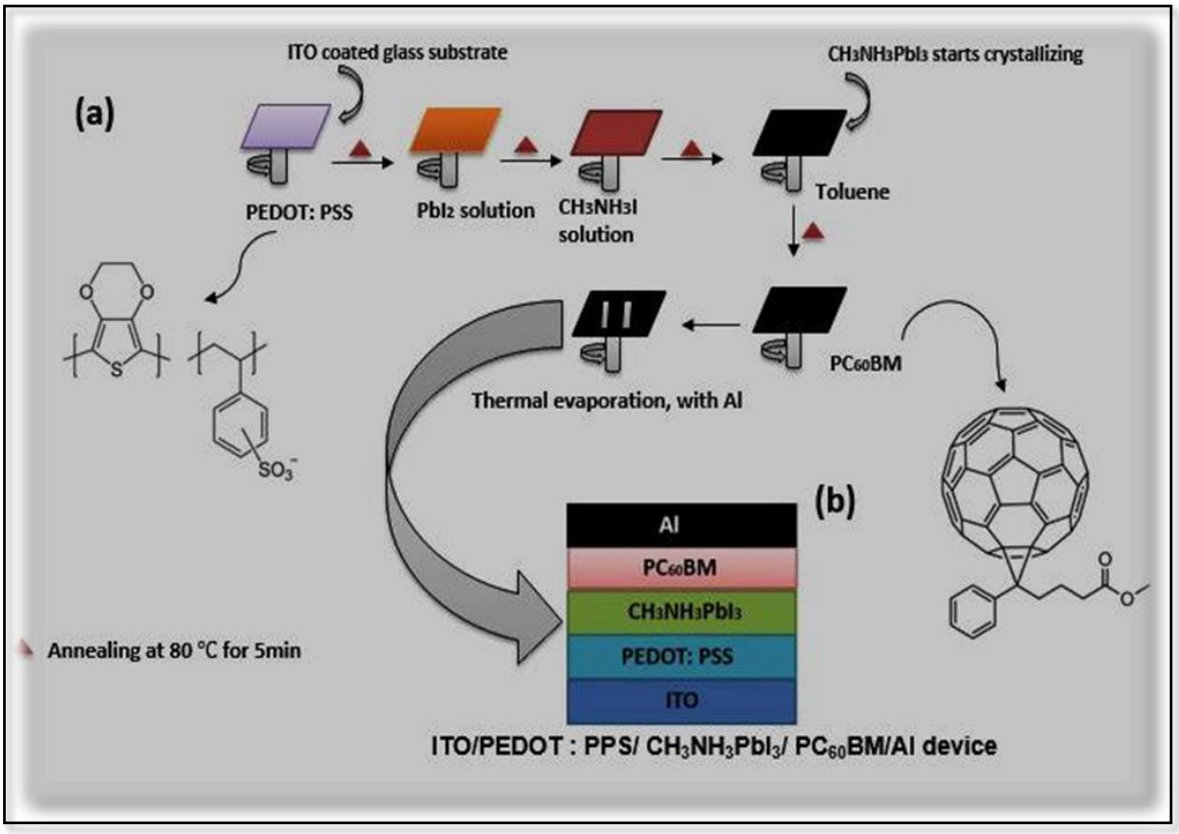

Fig. 4.7: Schematic illustration of the (a) Fabrication process of the device (b) Architectural design of the fabricated ITO/PEDOT:PSS/$CH_3NH_3PbI_3$/PCBM/Al.

4.3 Results and Discussion

4.3.1 Morphology analysis

A visual analysis of the perovskite films was done by exposing the films in air at room temperature as shown in Fig 4.8 (a). The degradation of the perovskite is indicated by the color change from dark brown to yellow after 24 h of air exposure. The yellow color is attributed to the dissociation of PbI_2 from the methyl ammonium lead iodide following the absorption of air H_2O and O_2 as schematically presented in Fig. 4.5.

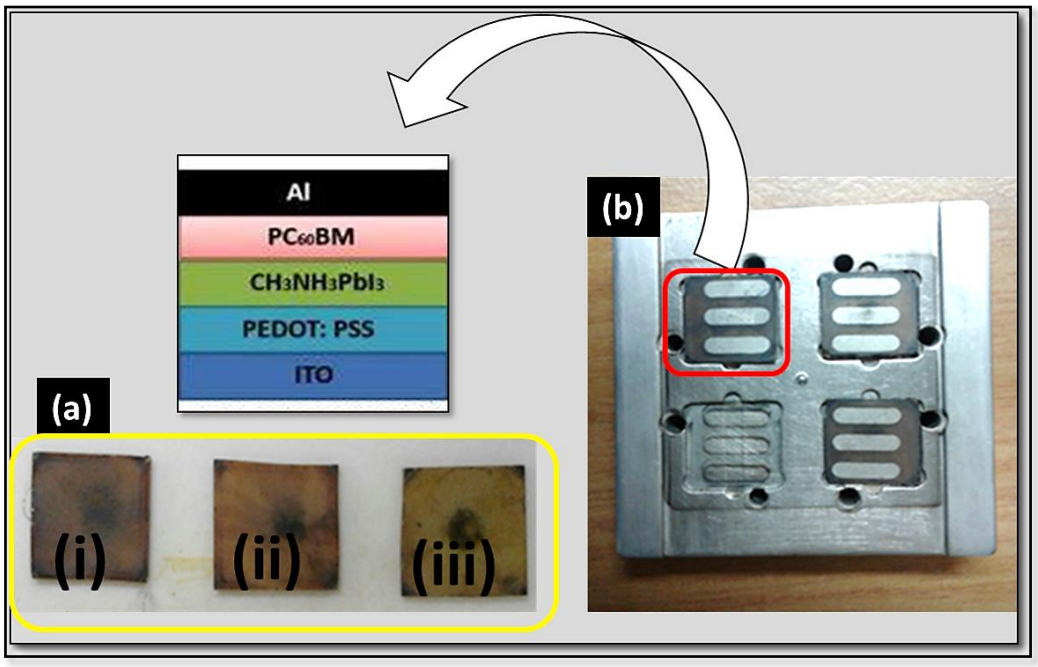

Fig. 4.8: Images of (a) Perovskite films after (i) 0 h; (ii) 12 h; (iii) 24 h of fabrication (b) Fully fabricated ITO/PEDOT: PSS/$CH_3NH_3PbI_3$/PCBM/Al device.

Fig. 4.9 (a) and (b) shows the optical microscopy image of the $CH_3NH_3PbI_3$ layer annealed taken immediately after spin coating (i.e. 0 h) and after 24 h, respectively. When a $CH_3NH_3PbI_3$ film is still fresh, a uniform layer is formed and larger crystal grain is revealed, as circled in Fig. 4.9 (a and d). After 24 h $CH_3NH_3PbI_3$ film degrades (, forming non-uniform "islands" as shown in Fig. 4.9 (a-c). Although the humidity was at minimal, the morphology of the films changes drastically after 24 h revealing the high sensitivity of $CH_3NH_3PbI_3$ to humidity.

It has been reported that the appearance of grain boundaries coincide with the presence of monohydrate ($MAPbI_3 \cdot H_2O$) Bragg reflections, hence prolonging the exposure time to humidity increases the peak intensity of monohydrate $MAPbI_3 \cdot H_2O$[13]. It is also very important to note that the optoelectronic properties of $CH_3NH_3PbI_3$ change depending on its crystallinity which determines the defect density on its crystal framework[19,35]. The grain boundaries also plays a role of crystal defects and consequently alters the material properties, hence a single uniform crystal is desired to achieve an optimal solar cell device[13]. In this work it was predicted that the boundaries (i.e. marking 1 and 2 in Fig. 4.9 (c) and arrows in Fig. 4.9(b)) between small crystal grains (i.e. line crossing marking 1 and 2 in Fig. 4.9(c)) plays a vital role in "retarding" the transport of electron as soon as they encounter these boundaries and consequently affect the optoelectronic properties of the

device. Some of the crystal growth methods to achieve uniform crystal grain have been previously reported and they include top seeded solution growth, hot-solution cooling-down growth, the inverse temperature method, and an anti-solvent vapor-assisted crystallization method[33,34,36]. All growth methods follow same key steps are which are nucleation and crystal growth[37].

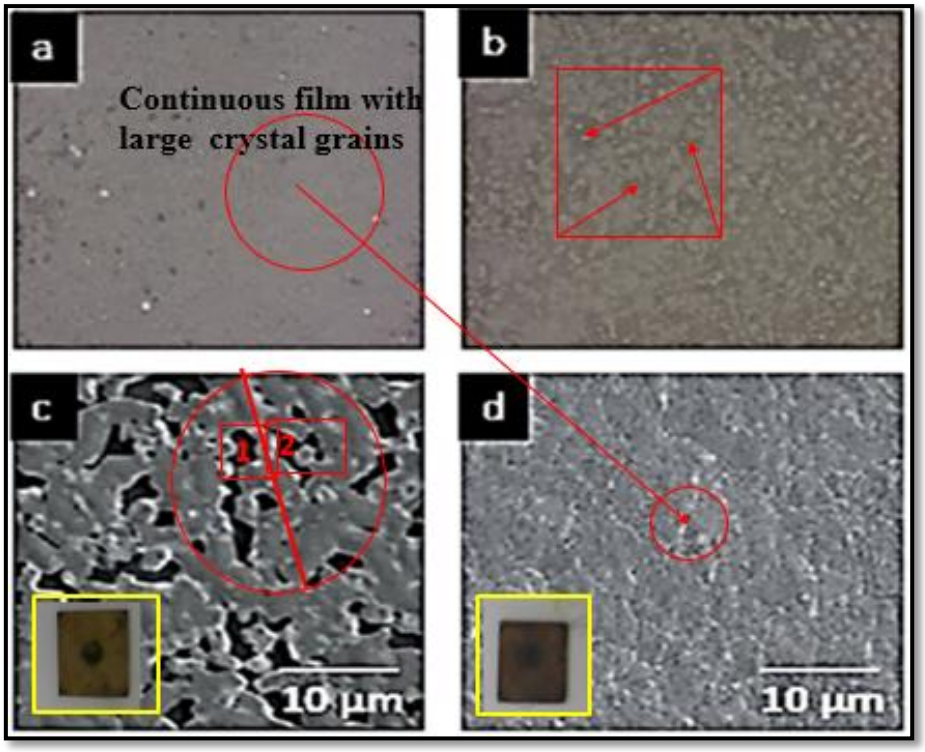

Fig.4.9: Optical micrograms taken at ×10 magnification) of the fabricated thin films after (a) 0 h and (b) 24 h and SEM images of the thin films with the corresponding images showing color change (i.e. insets) after (c) 24 h and (d) 0 h.

4.3.2 Current-voltage (I-V) characterization of the fabricated device

Fig. 10 shows *J-V* curve of the devices recorded under dark current and under illumination, measured after (a) 24 h and (b) 0 h. The I-V characteristics were measured at room temperature at a relative humidity (RH) of 55-57 %. The higher current density (J_{sc}) of 7.43 × 10^{-3} mA/cm^2 for device recorded after 0 h is attributed to the presence of pristine large uniform grains of fresh samples, Fig. 4.9 (b-c), such large grains promote charge transport by minimizing grain boundary limited electrical transport.

The mean free path of the electron is surmised to be in the same length scale as that of the grain size for larger crystals[36]. J_{sc} values are obtained by calculating the ratio of the current and the cross-sectional area (7×10^{-4} cm^2) of the semiconductor. The reduced presence of grain boundaries which act as charge carrier traps promotes the flow of charges[38].

The shunt resistance (R_{sh}) was calculated from the point in the vicinity of zero voltage (J_{sc}) and also using Eq.1, which is the slope of the curve and taking its inverse, gives R_{sh}. Series resistance (R_s) was also calculated in the vicinity of zero current (V_{oc}), taking the inverse of the slope as the R_s value. The vicinities used to calculate the R_{sh} and R_s are indicated on Fig. 4.10 (insert). For an ideal solar cell device $R_{sh} = \infty$ and it does not provide a substitute path for current to flow and $R_s = 0$ and no voltage drop occur. This is not observed in the device due to either intermixing of the active layer with the electron transport layer, which thus increases the recombination pathways.

In Table 1 it has been recorded that the R_s value for the device measured after 0 h is less than R_{sh}, 0.371 Ω cm^2 and 0.119 Ω cm^2, respectively, indicating a relative fair performance of the newly fabricated device. An increased R_s in a device analyzed after 24 h is attributed to the formation of grain boundaries on the film as indicated in Fig. 4.10 (b and c) resulting in poor charge transfer as they encounter these boundaries. R_s is greater than R_{sh} which also gives a much clear explanation of the low fill factor (FF) observed.

The low FF was mainly due to high series and low shunt resistance which can be virtually predicted by the curved shape of the obtained I-V curves, (Fig. 4.10). It is also shown in Table 1, that the R_{sh} for the device recorded at 0 h is greater than that recorded after 24 h period and this is attributed to the fact that R_{sh} is sensitive to the donor-acceptor interface area, hence the change is the nanoscale morphology of the fabricated device after 24 h had caused this drop in R_{sh} and hence the decrease in device performance.

It is also known that the power losses can be enhanced by the resistance (i.e. series and shunt) induced by the current or leakage currents around the sides of the device[39,18,40]. The series resistance also give ideas on the quality of the device and can be used as fabrication test, the higher the R_s the poor the device quality and hence poor performance[41]. This also supports the observation where the R_s value for a device recorded after 24 h was higher than that recorded at 0 h period. Fill factor (FF) is also a very sensitive parameter compared to open-circuit voltage (V_{oc}) and short-circuit current (J_{sc})[42-48].

The methods to quantify the FF losses with simplicity and without ambiguity has also been reported[49-54]. The large decrease in V_{oc} from 0 h to 24 h under illumination is attributed to decomposition of the photoactive layer[55-57], V_{oc} decreased from 0.65 V to 0.15 V as illustrated by the semi-log J-V characteristics under illumination, (Fig. 4.11). The semi-log plot also indicates an example of where the short circuit current and open circuit voltage are found, (brown circles).

$$R_{sh}/R_s = \frac{\Delta V}{\Delta Jsc} \qquad \textbf{eq. 1}$$

Fill factor values were estimated using eq. 2. Where P_{max} is the maximum power output and it was estimated where the I-V plot bends.

$$FF = \frac{Pmax}{Voc \times Isc} \qquad \textbf{eq. 2}$$

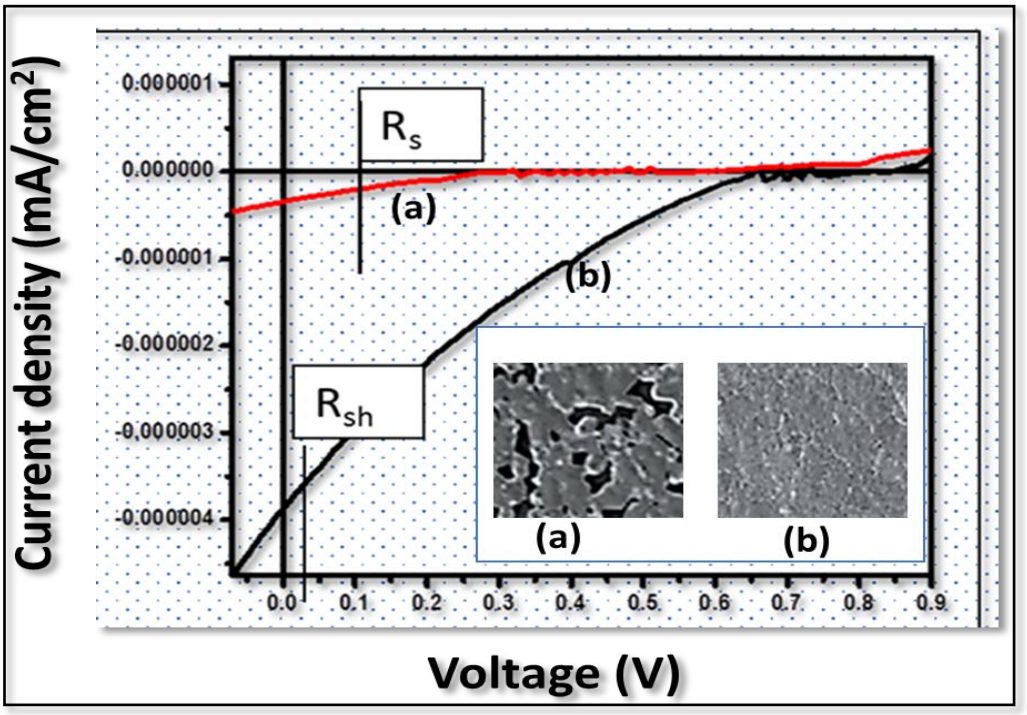

Fig. 4.10: I-V curve analysis of ITO/PEDOT:PSS/$CH_3NH_3PbI_3$/PCBM/Al device under illumination: (a) 24 h and (b) 0 h (measured at AM 1.5/ 100 mW/cm^2 illumination and area of the device was 0.07 mm^2/ 7×10^{-4} cm^2).

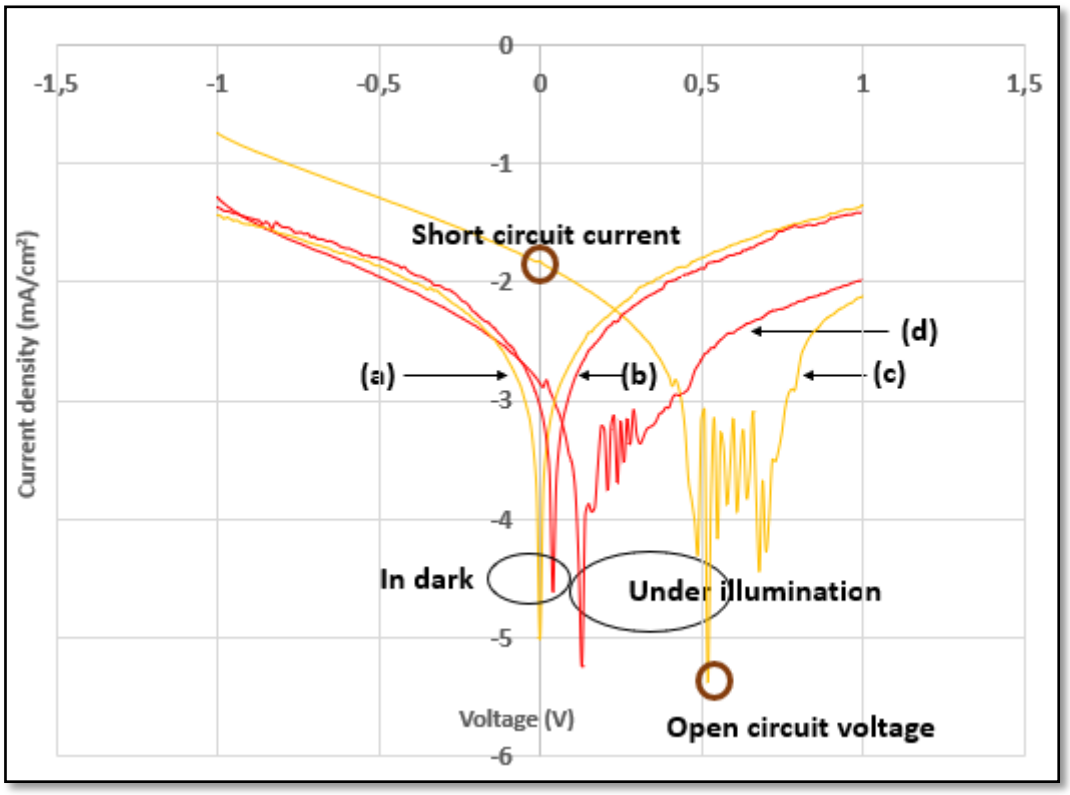

Fig. 4.11: Semi-log J-V characteristics of device measured after (a) 0 h and (b) 24 h in the dark and device measured after (c) 0 h and (d) 24 under illumination.

Table 1: Current-voltage parameters of the fabricated devices measured at AM 1.5 / 100 mW/cm^2 illumination

Time[a]	**Isc (μA)**	**Jsc (mA/cm^2)**	**V_{oc} (V)**	**R_{SH} (Ω cm^2)**	**R_s (Ω cm^2)**	**FF (%)**
0 h	5.20	7.43×10^{-3}	0.62	0.371	0.119	1.83
24 h	0.50	7.14×10^{-4}	0.15	0.036	0.296	9.34×10^{-3}

The time at which the devices were exposure to moisture or air[a]

4.4 References

1. Yan, W. High-performance hybrid perovskite solar cells with open circuit voltage dependence on hole-transporting materials. *Nano Energy* **16,** 428–437 (2015).
2. Chen, X. Multifunctional Inverse Opal-Like TiO_2 Electron Transport Layer for Efficient Hybrid Perovskite Solar Cells. *Adv. Sci.* **2,** 44-47 (2015).
3. Frost, J. M. & Walsh, A. What Is Moving in Hybrid Halide Perovskite Solar Cells? *Acc. Chem. Res.* **49,** 528–535 (2016).
4. Xia, Z., Chai, G., Wang, Y. & Zhou, H. Uniform perovskite photovoltaic thin films via ultrasonic spray assisted deposition method. *2015 IEEE 42nd Photovolt. Spec. Conf. PVSC 2015* 1–4 (2015). doi:10.1109/PVSC.2015.7355719
5. Kuang, C. Highly Efficient Electron Transport Obtained by Doping PCBM with Graphdiyne in Planar-Heterojunction Perovskite Solar Cells. *Nano Lett.* **15,** 2756–2762 (2015).
6. Mei, A. A hole-conductor–free, fully printable mesoscopic perovskite solar cell with high stability. *Science.* **345,** 295–298 (2014).
7. Ledinsk, M. Raman spectroscopy of organic-inorganic halide perovskites. *J. Phys. Chem. Lett.* **6,** 401–406 (2015).
8. Park, N. G. Perovskite solar cells: An emerging photovoltaic technology. *Mater. Today* **18,** 65–72 (2015).
9. Zhao, X. & Park, N. Stability Issues on Perovskite Solar Cells. *Nature*. 1139–1151 (2015).
10. Song, D. H., Heo, J. H., Han, H. J., You, M. S. & Im, S. H. Reproducible formation of uniform CH3NH3PbI3-xClx mixed halide perovskite film by separation of the powder formation and spin-coating process. *J. Power Sources* **310,** 130–136 (2016).
11. Mashiyama, H. Disordered Cubic Perovskite Structure of CH3NH3PbX3 (X = Cl , Br , I). *ASC Adv.* **32,** 156–158 (1998).
12. Jung, H. S. & Park, N. G. Perovskite solar cells: From materials to devices. *Small*. **11,** 10–25 (2015).
13. Mastroianni, S. Analysing the effect of crystal size and structure in highly efficient CH3NH3PbI3 perovskite solar cells by spatially resolved photo- and electroluminescence imaging. *Nanoscale.* 19653–19662 (2015).
14. Yan, W. High-performance hybrid perovskite solar cells with open circuit voltage dependence on hole-transporting materials. *Nano Energy.* **16,** 428–437 (2015).
15. Chen, X. Multifunctional Inverse Opal-Like TiO2 Electron Transport Layer for Efficient Hybrid Perovskite Solar Cells. *Advanced Science.* **2,** 14-20 (2015).
16. Frost, J. M. & Walsh, A. What Is Moving in Hybrid Halide Perovskite Solar Cells? *Accounts*

of Chemical Research. **49,** 528–535 (2016).

17. Xia, Z., Chai, G., Wang, Y. & Zhou, H. Uniform perovskite photovoltaic thin films via ultrasonic spray assisted deposition method. *2015 IEEE 42nd Photovoltaic Specialist Conference, PVSC 2015* 1–4 (2015). doi:10.1109/PVSC.2015.7355719
18. Kuang, C. Highly Efficient Electron Transport Obtained by Doping PCBM with Graphdiyne in Planar-Heterojunction Perovskite Solar Cells. *Nano Letters* **15,** 2756–2762 (2015).
19. Mei, A. A hole-conductor–free, fully printable mesoscopic perovskite solar cell with high stability. *Science.* **345,** 295–298 (2014).
20. Ledinsk, M. Raman spectroscopy of organic-inorganic halide perovskites. *Journal of Physical Chemistry Letters*. **6,** 401–406 (2015).
21. Park, N. G. Perovskite solar cells: An emerging photovoltaic technology. *Materials Today*. **18,** 65–72 (2015).
22. Zhao, X. & Park, N. Stability Issues on Perovskite Solar Cells. *Science*. **13,** 1139–1151 (2015).
23. Song, D. H., Heo, J. H., Han, H. J., You, M. S. & Im, S. H. Reproducible formation of uniform CH3NH3PbI3-xClx mixed halide perovskite film by separation of the powder formation and spin-coating process. *Journal of Power Sources.* **310,** 130–136 (2016).
24. Mashiyama, H. Disordered Cubic Perovskite Structure of CH3NH3PbX3 (X = Cl , Br , I). *ASC Adv.* **32,** 156–158 (1998).
26. Jung, H. S. & Park, N. G. Perovskite solar cells: From materials to devices. *Small*. **11,** 10–25 (2015).
27. Mastroianni, S. Analysing the effect of crystal size and structure in highly efficient CH3NH3PbI3 perovskite solar cells by spatially resolved photo- and electroluminescence imaging. *Nanoscale*. 19653–19662 (2015).
28. Marinova, N. Light Harvesting and Charge Recombination in CH 3 NH 3 PbI 3 Perovskite Solar Cells Studied by Hole Transport Layer Thickness Variation. *ACS Nano*. **9,** 4200–4209 (2015).
29. Hwang, J. O. Workfunction-tunable, N-doped reduced graphene transparent electrodes for high-performance polymer light-emitting diodes. *ACS Nano.* **6,** 159–167 (2012).
30. Editorial. Perovskite fever. *Nat. Mater.* **13,** 837 (2014).
31. Ghanavi, S. Organic-inorganic hybrid perovskites as light absorbing/hole conducting material in solar cells. *Master Thesis*, 1–37 (2013). doi:1650-8297
32. Servaites, J. D., Ratner, M. A. & Marks, T. J. Organic solar cells: A new look at traditional

models. *Energy Environ. Sci.* **4,** 4410–4422 (2011).

33. Liu, J. Two-Dimensional CH3NH3PbI3 Perovskite: Synthesis and Optoelectronic Application. *ACS Nano* **10,** 3536–3542 (2016).
34. Boucl, J. & Herlin-Boime, N. The benefits of graphene for hybrid perovskite solar cells. *Synthetic Metals*. **58**, 4-8 (2015).
35. Wan, L. F. Atomically-thin interfacial suboxide key to hydrogen storage performance enhancements of magnesium nanoparticles encapsulated in reduced graphene oxide. *Nano Lett*. **77**, 45-48 (2009).
36. Boopathi, K. M. Preparation of metal halide perovskite solar cells through a liquid droplet assisted method. *J. Mater. Chem. A* **3,** 9257–9263 (2015).
37. Singh, V., Arora, S., Arora, M., Sharma, V. & Tandon, R. P. Optimizing P3HT/PCBM/MWCNT films for increased stability in polymer bulk heterojunction solar cells. *Physics Letters, Section A: General, Atomic and Solid State Physics*. **378,** 3046–3054 (2014).
38. Kim, H.-S. Lead iodide perovskite sensitized all-solid-state submicron thin film mesoscopic solar cell with efficiency exceeding 9%. *Scientific reports* **2,** 591 (2012).
39. Bogatyrev, V. M., Borisenko, N. V. & Pokrovskii, V. A. Thermal Degradation of Polyvinylpyrrolidone on the Surface of Pyrogenic Silica. *Russian Journal of Applied Chemistry*. **74,** 839–844 (2001).
40. De Volder, M. F. L., Tawfick, S. H., Baughman, R. H. & Hart, a J. Carbon nanotubes: present and future commercial applications. *Science (New York, N.Y.)*. **339,** 535–9 (2013).
41. Liu, H., Zhang, Y., Li, R., Sun, X. & Abou-Rachid, H. Thermal and chemical durability of nitrogen-doped carbon nanotubes. *J. Nano. Res.* **14,** 1016 (2012).
42. Im, J.-H., Chung, J., Kim, S.-J. & Park, N.-G. Synthesis, structure, and photovoltaic property of a nanocrystalline 2H perovskite-type novel sensitizer (CH3CH2NH3)PbI3. *Nano. Res. Lett.* **7,** 353 (2012).
43. Hao, F. Solvent-Mediated Crystallization of CH 3 NH 3 SnI 3 Films for Heterojunction Depleted Perovskite Solar Cells. *Science.* **15,** 827- 829 (2015).
44. Ravula, S., Baker, S. N., Kamath, G. & Baker, G. A. Ionic liquid-assisted exfoliation and dispersion: stripping graphene and its two-dimensional layered inorganic counterparts of their inhibitions. *Nanoscale.* **7,** 4338–4353 (2015).
45. Tidhar, Y. Crystallization of Methyl Ammonium Lead Halide Perovskites : Implications for Photovoltaic Applications Crystallization of Methyl Ammonium Lead Halide Perovskites :

Implications for Photovoltaic Applications. *Nature*. **36,** 44-46 (2014).

46. Wang, Q. Large fill-factor bilayer iodine perovskite solar cells fabricated by a low-temperature solution-process. *Energy & Environ. Science*. **7,** 2359 (2014).
47. Zhou, Y. Room-Temperature Crystallization of Hybrid-Perovskite Thin Films via Solvent-Solvent Extraction for High-Performance Solar Cells. *J. Mater. Chem. A.* **3,** 8178–8184 (2015).
48. Jeon, N. J. Solvent engineering for high-performance inorganic-organic hybrid perovskite solar cells. *Nature materials* **13,** 1–7 (2014).
49. Brgoch, J., Lehner, A. J., Chabinyc, M. L. & Seshadri, R. Ab Initio Calculations of Band Gaps and Absolute Band Positions of Polymorphs of RbPbI3 and CsPbI3: Implications for Main-Group Halide Perovskite Photovoltaics. *J. Phy Chem C*. **18,** 27721–27727 (2014).
50. Zhang, F. Film-through large perovskite grains formation via a combination of sequential thermal and solvent treatment. *Science*. **16,** 444-449 (2016).
51. Fu, Y. Solution growth of single crystal methylammonium lead halide perovskite nanostructures for optoelectronic and photovoltaic applications. *J. Am Chem Soc.* **137,** 5810–5818 (2015).
52. Brenner, T. M., Egger, D. a., Kronik, L., Hodes, G. & Cahen, D. Hybrid organic—inorganic perovskites: low-cost semiconductors with intriguing charge-transport properties. *Nature Reviews Materials* **1,** 15007 (2016).
53. Markvart, T. & Castañer, L. *Principles of Solar Cell Operation*. *Practical Handbook of Photovoltaics* (Elsevier Ltd, 2012). doi:10.1016/B978-0-12-385934-1.00001-5
54. Schiefer, S., Zimmermann, B. & Glunz, S. W. Applicability of the Suns-V OC Method on Organic Solar Cells. *IEEE Journal of Photovoltaics* **4,** 271–277 (2014).
56. Cabestany, J. & Castañer, L. A simple solar cell series resistance measurement method. *Revue de Physique Appliquée* **18,** 565–567 (1983).
57. Gupta, D., Mukhopadhyay, S. & Narayan, K. S. Fill factor in organic solar cells. *Solar Energy Materials and Solar Cells* **94,** 1309–1313 (2010).

Chapter 5

Conclusions, recommendations and future work

5.1 Nitrogen doped hollow carbon spheres

This work provides a foundational study that reveals the effect of N-doping on bHCSs. N-bHCSs were successfully synthesized by a CVD method using polydispersed SiO_2 spheres as first demonstrated by Mutuma and co-workers[48]. Raman spectroscopy analysis confirmed the presence of the graphitized/disordered carbon in all the synthesized N-bHCSs. This observation was in agreement with the TGA results obtained, which showed a reduced thermal stability of the N-bHCSs as compared to pristine bHCSs.

The outcome of this study supported the hypothesis formulated. We successfully proved that doping P3HT:PCBM blends with N-bHCSs can to some extent enhance the electronic properties of these materials and further improve the performance of organic solar cells. This lays a foundation for new studies on these materials, especially in the area of photovoltaics.

The bonding domains on N-bHCSs and C/N ratios were also important for this study and the information was obtained using X-ray photoelectron spectroscopy (XPS) which revealed the presence of pyridinic N, pyridinic N+-O, pyrolic N and graphitic N incorporated onto the bHCSs framework.

Recommendations and future work

It is also important to take note that the blend ratio of the donor and acceptor material and solvent used for their dissolution are very important parameters in the fabrication process of the device[56]. Hence future studies should also make evaluate the optimal weight ratios and solvents for similar work. The optimal P3HT:PCBM weight ratio for this study was 1:1 and N-BHCSs doping weight ratio was 1:1:0.1.

5.2 Inorganic-organic hybrid perovskite devices

This study provided insights on the degradation rate of inorganic-organic hybrid perovskite based photovoltaic devices. A thin film solar cell device was successfully fabricated using a spin coating

method under ambient conditions. I-V characterization of the device revealed a good performance of the device while it is still fresh and after minimal air/moisture exposure. The device was further analysed after a 24 h period, where it showed a decrease in performance. Morphology studies of the devices revealed the formation of small grains or islands as the $CH_3NH_3PbI_3$ degraded under moisture exposure. This was concluded to be the major cause of reduced device performance, since it has also been reported that these grain boundaries limit the path or channels for charge carrier movement within the device.

The variations in device parameters such as the series and shunt resistance provided a clear view of the device performance and the findings were consistence with literature findings. We are confident to conclude that $CH_3NH_3PbI_3$ is very sensitive to moisture and it degrades as exposure is prolonged. It is also recommended that the fabrication should be done in a very controlled environment that takes into consideration the elimination or reduction of moisture.

Recommendations and future work

Future work should consider materials that can encapsulate the perovskite materials without hindering its absorption ability to harvest the sunlight. N-bHCSs studied in this thesis were initially seen as one of the potential materials to encapsulate the perovskite materials, but after a careful consideration on the inability of carbon to absorb light, the study was not taken further. However, we did not completely rule out the ability of N-bHCSs to be used as a potential material for encapsulation; optimization of all parameters (i.e. from fabrication to the device composition) is the first step that will be undertaken in projected future work.

.